The Detection of Amyloid-Beta Neuroplaques Using Thioflavin T and Secondary Ion Mass Spectrometry

A thesis submitted to The University of Manchester for the degree of

Masters of Philosophy in Instrumentation

in the Faculty of The School of Chemical Engineering and Analytical Science

2014

Taylor P. Kohn

Chemical Engineering and Analytical Science

Table of Content

TABLE OF CONTENT **2**

LIST OF FIGURES **5**

LIST OF TABLES **19**

LIST OF EQUATIONS **20**

1. ABSTRACT **21**

2. DECLARATION **22**

3. COPYRIGHT **22**

4. ACKNOWLEDGEMENTS **24**

5. INTRODUCTION **26**

5.1 PROJECT AIMS **26**

5.2 SIMS INTRODUCTION **28**

5.2.1 HISTORY OF SIMS 28

5.2.2 PRIMARY ION SOURCES 29

5.2.3 J105 3D CHEMICAL IMAGER 32

5.2.5 SIMS IMAGING OF THE BRAIN AND ALZHEIMER'S DISEASE 39

5.3 ALZHEIMER'S DISEASE INTRODUCTION **40**

5.3.1 STATISTICS OF ALZHEIMER'S DISEASE 40

5.3.2 CLINICAL PROGRESSION OF ALZHEIMER'S DISEASE 40

5.3.3 PATHOPHYSIOLOGY OF ALZHEIMER'S DISEASE 44

5.3.4 *IN VITRO* DETECTION OF AMYLOID PLAQUES 46

6. COMPARING SPUTTER YIELDS OF PRIMARY ION BEAMS **50**

6.1 SPUTTER YIELD INTRODUCTION 50

6.1.1 PROJECT AIMS 50

6.1.2 PREVIOUS RESEARCH 52

6.2 SPUTTER YIELD EXPERIMENTAL DESIGN 54

6.2.1 IRGANOX FILM PREPARATION 54

6.2.2 ARGININE FILM PREPARATION 55

6.2.3 ANGIOTENSIN II FILM PREPARATION 56

6.2.4 HALOPERIDOL FILM PREPARATION 58

6.2.5 UNWASHED SILICON WAFERS 58

6.2.6 MEASURING FILM THICKNESSES 59

6.2.7 SPUTTERING 61

6.2.8 DIGITAL HOLOGRAPHIC MICROSCOPE 62

6.2.9 CALCULATING VOLUME REMOVED 65

6.3 SPUTTER YIELD RESULTS 70

6.4 SPUTTER YIELD DISCUSSION 76

6.4.1 COMPARING $(H_2O)_N^+$ AND AR_N^+ SPUTTER YIELDS FOR IRGANOX 1010. 76

6.4.2 COMPARING PRIMARY ION SPUTTER YIELDS OF ARGININE. 79

7. MOUSE BRAIN TISSUE ANALYSIS 83

7.1 TISSUE STAINING AND SIMS ANALYSIS INTRODUCTION 83

7.1.1 PROJECT AIMS 83

7.1.2 PREVIOUS RESEARCH 84

7.1.3 STRUCTURE OF THE MOUSE BRAIN 87

7.2 TISSUE ANALYSIS EXPERIMENTAL DESIGN 90

7.2.1 COLLECTING MOUSE BRAIN SAMPLES 90

7.2.2 STAINING PROTOCOL DEVELOPMENT 91

7.2.3 STAINING PROTOCOL 97

7.2.4 SIMS CONDITIONS 98

7.3 TISSUE ANALYSIS RESULTS 100

7.4 TISSUE ANALYSIS CONCLUSIONS 131

8. REFERENCES 137

List of Figures

FIGURE 1: COMPARISON OF SIGNAL INTENSITY FOR 10KEV Ar_{1000}^{+} BEAM AND 10KEV $H_2O_N^{+}$ CLUSTER ION BEAM ON MULTIPLE FILMS. 32

FIGURE 2: SCHEMATIC OF THE J105 3D CHEMICAL IMAGER PRODUCED BY IONOPTIKA IN SOUTHAMPTON, UK. 33

FIGURE 3: EXAMPLE OF CHARGING. RAT WILD-TYPE BRAIN WAS RUN AT: 20KEV C_{60}^{+} PRIMARY ION BEAM, 22V BIAS, ION DOSE 2.05E12 IONS/CM^2, SPOT SIZE 7.5MM. WHEN THE BIAS WAS INCREASED TO 45V THE SAMPLE CEASED TO CHARGE. 36

FIGURE 4: THE FIVE STAGES OF CLINICAL SYMPTOMS ASSOCIATED WITH ALZHEIMER'S DISEASE. 41

FIGURE 5: T1-WEIGHTED MRI SCANS OF AN INITIALLY ASYMPTOMATIC PATIENT WITH GENETIC FAMILIAL ALZHEIMER'S DISEASE. SCANS WERE DONE OVER A 4-YEAR PERIOD AND THE FIRST SYMPTOMS OF ALZHEIMER'S DISEASE WERE RECORDED BETWEEN IMAGE 4 AND 5. THE RED AREAS INDICATE LOSS OF BRAIN VOLUME AS THE DISEASE PROGRESSES. 43

FIGURE 6: THE PROCESS BY WHICH MISFOLDED MONOMERS GROW TO FORM FIBRILS. 45

FIGURE 7: LEFT: AMYLOID PLAQUES STAINED WITH CONGO RED AND VIEWED UNDER A MICROSCOPE WITH NORMAL LIGHT. RIGHT: THE SAME SAMPLE BUT VIEWED WITH A POLARISED LIGHT, DEMONSTRATING THE "APPLE GREEN" BIREFRINGENCE. 46

FIGURE 8: STRUCTURE OF THIOFLAVIN T.[84] 47

FIGURE 9: COMPUTER MODELING OF THIOFLAVIN T'S INTERACTION WITH A PROTEIN BETA SHEET. THE FIGURE SHOWS THIOFLAVIN T NESTLED INTO THE "CHANNEL" RUNNING ALONG THE BETA SHEET AND THAT THE Π ORBITALS OF THIOFLAVIN T'S BENZOTHIAZOLE AND A BENZAMINE RING INTERACT WITH THE BOTH THE Π ORBITAL AND CH GROUPS IN THE BETA SHEET. 48

FIGURE 10: ARGININE FILMS SECONDARY ION YIELDS FOR VARIOUS Ar_N^+, C_{60}^+, AND $(H_2O)_N^+$ PRIMARY IONS. AN ION DOSE OF 5E11 IONS/CM^2 SPUTTERED THE SAMPLE AND THE SECONDARY ION YIELD WAS DETERMINE USING TOF-SIMS. SECONDARY ION YIELDS WERE MEASURED BY DR. SADIA SHERAZ. 53
FIGURE 11: MOLECULAR STRUCTURE OF IRGANOX 1010. 54
FIGURE 12: CHEMICAL STRUCTURE OF L-ARGININE. 55
FIGURE 13: SPACE FILLING MODEL OF ANGIOTENSINOGEN, THE PARENT MOLECULE OF ANGIOTENSIN II BEFORE ENZYMATIC DEGRADATION. THE BLACK ARROW INDICATES WHERE ANGIOTENSINOGEN IS CLEAVED BY RENIN TO FORM ANGIOTENSIN I. THE GREEN ARROW INDICATES WHERE ANGIOTENSIN-CONVERTING ENZYMES CLEAVE ANGIOTENSIN I INTO THE 8-AMINO-ACID PEPTIDE ANGIOTENSIN II. 56
FIGURE 14: CHEMICAL STRUCTURE OF HALOPERIDOL. 58
FIGURE 15: SCHEMATIC OF THE NANOCALC-XR THIN FILM REFLECTROMETRY 59
FIGURE 16: DHM UTILISES BOTH THE PHASE AND AMPLITUDE OF LIGHT TO CREATE A DIGITAL HOLOGRAM. 62
FIGURE 17: DHM GENERATED "PHASE VIEW" OF A CRATER. THE BLUE ARROW INDICATES AN AREA WHERE COMPUTER CALCULATED PHASE AND MEASURED PHASE ARE THE SAME. THE BLACK ARROW INDICATES AN AREA WHERE THE PHASE PREDICTED AND THE PHASE MEASURED IS DIFFERENT. 63
FIGURE 18: COMPUTER ALGORITHM CALCULATES THE DIFFERENCE IN PHASES (LEFT) TO CREATE A HOLOGRAM (RIGHT) THAT CONTAINS INFORMATION REGARDING THE HEIGHTS OF THE SAMPLE. 63
FIGURE 19: NPL IRGANOX 1010 FILM PREPARED THROUGH THERMAL EVAPORATION. THIS PHOTO WAS TAKEN AFTER SPUTTER YIELD EXPERIMENTS AS LITTLE SQUARES CAN BE SEEN ON THE FILM. PHOTO TAKEN 10 MARCH 2014. 64

FIGURE 20: COMPUTER-CALCULATED CROSS SECTION OF CRATERS. (A) CRATERS FORMED FROM C_{60}^{+} PRIMARY IONS SPUTTERING GAVE A NEARLY PERFECT CUBE SHAPE. (B) CRATERS FORMED FROM Ar_N^{+} AND $(H_2O)_N^{+}$ PRIMARY IONS SPUTTERING GAVE SIDES THAT WERE SLOPED AND ANGLED MAKING THE DETERMINATION OF THE VOLUME DIFFICULT. 65

FIGURE 21: DEMONSTRATION OF HALF-THE-SLOPE-VOLUME CALCULATIONS. (A) THE TYPICAL SLOPING SLIDES ARE SEEN IN THE CROSS SECTION OF THIS CRATER MADE THROUGH $(H_2O)_N^{+}$ PRIMARY IONS SPUTTERING. THE RED BOX AT THE CENTER OF THE CRATER IS THE AREA OF THIS COMPUTER-GENERATED CROSS SECTION WHERE THE WIDTH STRETCHES FROM HALF ONE SLOPE TO HALF THE OTHER SLOPE. (B) USING COMPUTER DRAWN SHAPES, THE ACTUAL VOLUME OF THE CROSS SECTION IS DRAWN HERE TO DEMONSTRATE THAT THE HALF-THE-SLOPE-VOLUME CALCULATION IS A VALID ESTIMATOR OF THE ACTUAL VOLUME. (C) THE DRAWN GREEN AND PURPLE SHAPES ARE MOVED TO FORM APPROXIMATELY THE SAME RED BOX THAT IS SEEN IN PANEL A. THE BLACK ARROWS SHOW THAT THE WHITE AND PURPLE TRIANGLES ARE DRAWN OUT TO THE SIDE SHOWING THAT THE AREA OVERLAPPING AND THE AREA WITHOUT COVERAGE ARE APPROXIMATELY THE SAME. RED ARROW INDICATES THE EXTRA AREA THAT IS INCLUDED AT THE BOTTOM OF THE CRATER BUT HAS NOT ACTUALLY BEEN REMOVED IN THE SPUTTERING EXPERIMENTS. THE BLUE ARROW INDICATES THE AREA THAT SPUTTERING HAS REMOVED, BUT IS NOT INCLUDED IN THE HALF-THE-SLOPE-VOLUME CALCULATIONS. 66

FIGURE 22: MEDUSA CROSS-SECTIONAL VIEW AND MEASURING THE WIDTH OF THE CRATER FROM HALF SLOPE TO HALF SLOPE. 67

FIGURE 23: HOLOGRAM WINDOW OF THE MEDUSA SOFTWARE. THE USER DRAWS THE BLUE BOXES AND THE COMPUTER PROGRAM GIVES THE AVERAGE HEIGHT OR DEPTH OF THOSE AREAS. SINCE THE SURFACE OF THE FILM IS NOT UNIFORMLY FLAT (BUT -4 NM,

-4 NM, -6 NM, AND -2 NM), THE SURFACE HAD TO BE AVERAGED (-4 NM) AND THEN SUBTRACTED FROM THE CALCULATED DEPTH (-35 NM) TO GIVE THE ACTUAL DEPTH (-31 NM). IT SHOULD ALSO BE NOTED THAT BOX 3, WHICH IS THE ESTIMATED DEPTH, SEEMS OFF CENTER, BUT THIS IS FROM HALF THE SLOPE TO HALF THE SLOPE. BOXES 1 AND 2 ARE DRAWN BASED OFF OF CROSS-SECTIONAL VIEWS AND THEN BOX 3 IS DRAWN TO BE THAT EXACT LENGTH AND WIDTH OF THOSE TWO BOXES. BOX 8 IS NOT ACTUALLY 0 NM, BUT IS A PROGRAMING ERROR WHERE THE LAST BOX DRAWN IS ALWAYS 0 NM. 68

FIGURE 24: GRAPHICAL REPRESENTATION COMPARING 2007 NPL STUDY WITH OUR DATA, SHOWING THAT THE TWO FOLLOW A SIMILAR TREND. 70

FIGURE 25: SPUTTER YIELDS FOR IRGANOX FILMS. IRGANOX 1010 WAS THE MOST EXTENSIVELY TESTED FILM. THE DATA DEMONSTRATES THAT SPUTTER YIELDS INCREASE AS THE KINETIC ENERGY OF THE BEAMS INCREASE. WHEN KINETIC ENERGIES ARE CONSTANT, C_{60}^+ PRIMARY IONS SPUTTER SIMILARLY TO $(H_2O)_N^+$ CLUSTER IONS, BUT BOTH SPUTTER GREATER THAN 20 KEV AR_N^+ CLUSTER IONS. C_{60}^+ PRIMARY ION AND $(H_2O)_N^+$ CLUSTER ION EXPERIMENTS WERE REPEATED IN AT LEAST TRIPLICATE. AR_N^+ CLUSTER IONS EXPERIMENTS WERE ONLY PERFORMED ONCE. 71

FIGURE 26: SPUTTER YIELDS FOR ARGININE FILMS. ARGININE RESULTS SHOW A GREATER VARIABILITY WITHIN CLUSTER ION TYPES THAN APPEARED IN IRGANOX 1010 STUDIES. WHILE 20 KEV $(H_2O)_{500}^+$ AND 20 KEV $(H_2O)_{2000}^+$ SPUTTER SIMILARLY, THERE IS A LARGE DROP IN $(H_2O)_{4000}^+$ CLUSTER ION SPUTTER YIELDS. SIMILARLY, 20 KEV AR_{500}^+ CLUSTER ION HAS A GREATER SPUTTER YIELD THAN 20 KEV AR_{2000}^+, INDICATING THAT THE LARGER POLYATOMIC PRIMARY IONS SPUTTER LESS THAN SMALLER POLYATOMIC IONS. 20 KEV C_{60}^+ PRIMARY IONS HAD THE GREATEST SPUTTER YIELDS. 20 KEV C_{60}^+, 20 KEV $(H_2O)_{500}^+$, AND 20 KEV $(H_2O)_{2000}^+$ CLUSTER IONS WERE TESTED IN AT LEAST

DUPLICATE, WHILE 20 KEV AR_{500}^{+}, 20 KEV AR_{2000}^{+}, AND $(H_2O)_{4000}^{+}$ CLUSTER IONS WERE TESTED ONCE. 72

FIGURE 27: SPUTTER YIELD RESULTS FOR HALOPERIDOL FILMS. ALL HALOPERIDOL SPUTTER YIELD EXPERIMENTS WERE RUN ONCE EXCEPT FOR 20 KEV C_{60}^{+} PRIMARY ION EXPERIMENTS, WHICH WERE RUN IN DUPLICATE. SIMILAR TO THE SPUTTERING OF ARGININE, 20 KEV C_{60}^{+} PRIMARY IONS HAD THE GREATEST SPUTTERING EFFECTS AND 20 KEV AR_{500}^{+} CLUSTER IONS HAVE A GREATER SPUTTER YIELD THAN 20 KEV AR_{2000}^{+} CLUSTER IONS. VARIATION WITHIN $(H_2O)_N^{+}$ CLUSTER IONS IS NOT SEEN AS $(H_2O)_{4000}^{+}$, $(H_2O)_{2000}^{+}$, AND $(H_2O)_{500}^{+}$ PRIMARY IONS ALL SPUTTER BETWEEN 80 AND 90 NM^3/ION. 73

FIGURE 28: SPUTTER YIELD RESULTS FOR ANGIOTENSIN II. ALL ANGIOTENSIN II EXPERIMENTS WERE RUN ONCE. OVERALL SPUTTER YIELDS ARE MUCH LESS THAN IRGANOX 1010, ARGININE, OR HALOPERIDOL. 20 KEV AR_{2000}^{+} PRIMARY IONS SPUTTER MUCH LESS THAN 20 KEV C_{60}^{+} OR 20 KEV $(H_2O)_{500}^{+}$ CLUSTER IONS. 20 KEV C_{60}^{+} OR 20 KEV $(H_2O)_{500}^{+}$ CLUSTER IONS HAD SIMILAR SPUTTER YIELDS. 74

FIGURE 29: SPUTTER YIELD RESULTS FROM SILICON SPUTTERING. ALL SILICON SPUTTERING EXPERIMENTS WERE PERFORMED ONCE. AR_N^{+} CLUSTER IONS WERE NOT TESTED SINCE PREVIOUS EXPERIMENTS PERFORMED IN THE LAB SHOWED NO VISIBLE SPUTTERING. ONCE AGAIN, SPUTTER YIELDS ARE GREATER WHEN THE KINETIC ENERGY IS GREATER. 20 KEV C_{60}^{+} PRIMARY IONS ALSO ONCE AGAIN HAD THE GREATEST SPUTTER YIELDS 75

FIGURE 30: LOG-LOG PLOT DEMONSTRATING THE UNIVERSAL SPUTTERING YIELD PLOT WHERE Y/N IS THE SPUTTER YIELD PER NUMBERS OF ATOMS IN THE PRIMARY CLUSTER AND E/AN IS ENERGY PER NUMBER OF ATOMS. 76

FIGURE 31: UNIVERSAL SPUTTER YIELD PLOTS FOR ARGON AND WATER CLUSTER ION BEAMS. (A) SEAH 2013 DATA PLOTTING ARGON SPUTTERING ON IRGANOX 1010 WITH LINEAR REGRESSION FITTING.[103] (B) OUR DATA PLOTTING WATER PRIMARY IONS SPUTTERING ON IRGANOX 1010 FOR 10 KEV $(H_2O)_{500}^+$, 10 KEV $(H_2O)_{2000}^+$, 20 KEV $(H_2O)_{500}^+$, 20 KEV $(H_2O)_{2000}^+$, AND 20 KEV $(H_2O)_{4000}^+$. IN ORDER TO COMPARE SEAH'S ARGON RESULTS (A) WITH OUR WATER RESULTS (B), THE UNITS MUST BE SLIGHTLY DIFFERENT. SEAH'S DATA MEASURES ENERGY PER NUMBER OF ATOMS IN THE CLUSTER, I.E. AR_{4000}^+ WOULD HAVE 2000 ATOMS IN EACH CLUSTER AND SO THE ENERGY OF EACH CLUSTER WOULD BE DIVIDED BY 2000. IN ORDER TO ACCURATELY COMPARE OUR DATA FOR WATER, WHICH CONSISTS OF BOTH HYDROGEN AND OXYGEN ATOMS, I CHOSE TO GRAPH ENERGY PER WATER MOLECULE IN EACH CLUSTER, I.E. $(H_2O)_{4000}^+$ WILL HAVE 4000 WATER MOLECULES AND SO THE ENERGY OF EACH CLUSTER WILL BE DIVIDED BY 4000. THIS INSURES THAT OUR COMPARISON IS PER *ION UNIT*. THIS COMPARISON IS NOT TO DETERMINE A UNIVERSAL EQUATION FOR THE WATER CLUSTER ION BEAM, BUT RATHER TO DEMONSTRATE THAT OUR WATER DATA ALSO APPEARS TO FOLLOW A SIMILAR UNIVERSAL SPUTTER YIELD TREND. WHILE (A) AND (B) ARE GRAPHED PER *ION UNIT*, THEY CANNOT BE GRAPHED ON THE SAME AXES, THUS FOR (C), OUR WATER SPUTTERING DATA AND OUR ARGON SPUTTERING DATA ARE GRAPHED USING THE UNIT ENERGY PER *NUCLEON* (I.E. THE COMBINATION OF NEUTRONS AND PROTONS WITHIN THE ATOM OR MOLECULE – ARGON HAS 40 NUCLEONS AND WATER HAS 18 NUCLEONS). (C) SHOWS THAT THE WATER CLUSTER ION BEAM HAS A GREATER ENERGY PER NUCLEON THAN ARGON.....78

FIGURE 32: LOG-LOG PLOT OF THE C_{60}^+, AR_N^+, AND $(H_2O)_N^+$ CLUSTER IONS ON AN ARGININE FILM. THREE EXPERIMENTS ARE POINTED TO AND THE SPUTTER YIELDS OF THESE THREE EXPERIMENTS ARE DISCUSSED ABOVE IN TABLE 7. 80

FIGURE 33: COMPARISON OF SECONDARY ION YIELDS WITH PREDICTED SPUTTER YIELDS FOR 20 KEV C_{60}^{+}, 20 KEV $(H_2O)_{500}^{+}$, 20 KEV $(H_2O)_{2000}^{+}$, AND 20 KEV $(H_2O)_{4000}^{+}$. EACH SECONDARY YIELD EXPERIMENT RECEIVED 5E11 ION DOSE, AND SECONDARY ION YIELD IS MEASURED FOR THE INITIAL LAYER. PREDICTED SPUTTER YIELDS WERE CALCULATED BY MULTIPLYING THE APPLIED ION DOSE BY THE SPUTTERING RATES CALCULATED ABOVE IN FIGURE 26. THE GRAPHS ILLUSTRATE THAT SECONDARY ION YIELD RATES OF 20 KEV $(H_2O)_{4000}^{+}$ ARE 10 TO 14 TIMES GREATER THAN THE SECONDARY ION YIELD RATES OF 20 KEV C_{60}^{+}. SECONDARY ION YIELDS WERE MEASURED BY DR. SADIA SHERAZ. 81

FIGURE 34: JOHANSSON GROUP IMAGE FROM PUBLISHED ARTICLE DEMONSTRATING THE CO-LOCALISATION OF TOF-SIMS-IDENTIFIED CHOLESTEROL, M/Z 369 (WHITE ARROW, A) AND P-FTAA STAINED AMYLOID-BETA AGGREGATES (BLUE SPOT, B). 86

FIGURE 35: ANATOMICAL IMAGE OF A SAGITTAL CUT MOUSE BRAIN. 87

FIGURE 36: ANATOMY OF THE BRAIN IDENTIFYING THE ISOCORTEX AND HIPPOCAMPUS FOR A) FLUORESCENT MICROSCOPY AND B) TOF-SIMS IMAGES. 88

FIGURE 37: 3XTG-AD MOUSE MODEL BRAIN TISSUE STAINED WITH THIOFLAVIN S DEPICTING INCREASED FLUORESCENT DUE TO AMYLOID-BETA AGGREGATES FOUND IN THE PYRAMIDAL NEURONS OF THE HIPPOCAMPUS. 89

FIGURE 38: ELECTRON MICROSCOPE IMAGE OF AN AMYLOID-BETA PLAQUE DEMONSTRATING THE STRINGY AGGREGATES FORMING CLUMPING TOGETHER TO FORM A MESH-LIKE STRUCTURE. 89

FIGURE 39: MASS SPECTRUM OF THIOFLAVIN T FILM. EXPERIMENT WAS CONDUCTED WITH THE C_{60}^{+} PRIMARY ION BEAM, A 4.5 MM SPOT SIZE, 11 PA, 500 SHOTS, A TILE 290 MM X 290 MM, 64 PIXELS/SQUARE, AND A 12% DUTY CYCLE FOR A TOTAL ION DOSE OF 2.18E12. 92

FIGURE 40: TOTAL ION IMAGES FOR PRE (A) AND POST (B) 0.02% THIOFLAVIN T STAINING OF A TRIPLE TRANSGENIC MOUSE BRAIN, HIPPOCAMPUS REGION. A) ANALYSED WITH THE C_{60}^+ PRIMARY ION BEAM, A SPOT SIZE OF 7.8 MM, A CURRENT OF 10 PA, 250 MM X 250 MM TILE SIZE, 32 X 32 PIXELS, ION DWELL WAS 200 SHOTS, A 50% DUTY CYCLE, FOR A TOTAL ION DOSE OF 2.05E12. B) ANALYSED WITH THE C_{60}^+ PRIMARY ION BEAM, A SPOT SIZE OF 7.8 MM, A CURRENT OF 4 PA, 250 MM X 250 MM TILE SIZE, 32 X 32 PIXELS, ION DWELL WAS 200 SHOTS, A 75% DUTY CYCLE, FOR A TOTAL ION DOSE OF 1.23E12. 93

FIGURE 41: PRE AND POST STAINS OF WILD TYPE MOUSE BRAIN, HIPPOCAMPUS REGION, LOOKING AT CHOLESTEROL DISTRIBUTION (369 M/Z). TISSUE WAS STAINED AS DESCRIBED IN THE NEXT SECTION, 7.2.2. BOTH TISSUE WERE IMAGES WITH THE C_{60}^+ PRIMARY ION GUN WITH A 7.7 MM SPOT SIZE, 22 PA, 250 MM X 250 MM TILES, 200 SHOTS, 32 X 32 PIXELS, 24% DUTY CYCLE, 16 X 10 TILES FOR AN ION DOSE OF 2.16E12. 94

FIGURE 42: FLUORESCENT MICROSCOPIC IMAGES OF STAINED WILD-TYPE MOUSE BRAIN, HIPPOCAMPUS REGION. BOTH TISSUES WERE DEHYDRATED IN 70% ETHANOL AND 80% ETHANOL EACH FOR 1 MINUTE BEFORE BEING STAINED IN 0.002% THIOFLAVIN DISSOLVED IN 80% ETHANOL FOR 8 MINUTES. A) THIS SAMPLE WAS WASHED IN 80% ETHANOL AND 70% ETHANOL FOR 1 MINUTE EACH BEFORE BEING RINSED TWICE IN DEIONISED WATER EACH FOR A MINUTE. B) THIS SAMPLE WAS WASHED TWICE IN 50% ETHANOL FOR 1 MINUTE EACH BEFORE BEING RINSED TWICE IN DEIONISED WATER EACH FOR A MINUTE. 96

FIGURE 43: TOTAL ION COUNT FOR WILD-TYPE MOUSE BRAIN ANAYLSIS - HIPPOCAMPUS AND ISOCORTEX REGIONS SHOWN. PRE-STAIN ANALYSIS WAS DONE WITH THE FOLLOWING PARAMETERS: C_{60}^+ PRIMARY ION BEAM, SPOT SIZE 7.8 MM, CURRENT 10 PA, TILE SIZE 250 MM X 250 MM, PIXELS 32 X 32, ION DWELL 200 SHOTS, DUTY CYCLE

50%, total ion dose 2.03E12 ions/cm^2. A stage bias of 45 Volts was added to the sample. Analysis was done with Image Analyzer. 101

Figure 44: The same sample as Figure 43, but image depicts the yields for the secondary ions with a mass-to-charge ratio of 125 m/z. This fragment is from the phosphate head of phosphonosphingolipids. These phosphate heads are present throughout the hippocampus and isocortex regions, but very few are found in the white matter. 102

Figure 45: The same sample as Figures 43 & 44, but image depicts the yields for the secondary ions with a mass-to-charge ratio of 184 m/z. This fragment is a larger ion from the phosphate head of phosphonosphingolipids. Again these phosphate heads are present throughout the hippocampus and isocortex regions and have a similar concentration as the 125 m/z fragments. 103

Figure 46: The same sample as Figures 43-45, but this image depicts the yields for the secondary ions with a mass-to-charge ratio of 369 m/z. This secondary ion is a fragment of chloestrol. Cholesterol is seen in high frequency in the white matter regions surrounding the hippocampus. Very little cholesterol is found in the hippocampus or isocortex. 104

Figure 47: The same sample as Figures 43-46, but this image depicts the yields for the secondary ions with a mass-to-charge ratio of 385 m/z. This secondary ion is a larger fragment of cholestrol. This fragment is seen with less intensity in the white matter than was seen with the secondary ion 369 m/z, however there does appear to be a greater frequency of this cholesterol fragment in the hippocampus and isocortex..... 105

Figure 48: The same sample as Figures 43-47, but this image depicts the yields for the secondary ions with a mass-to-charge ratio of 267 m/z. The secondary

ION WITH A MASS-TO-CHARGE RATIO OF 267 M/Z IS THE CHARACTERISTIC FRAGMENT FOR THE THIOFLAVIN T MOLECULE AS DETERMINED IN EARLIER EXPERIMENTS. AREAS OF HIGH INTENSITY ARE NOT SEEN, BUT RATHER DIFFUSED BACKGROUND. 106

FIGURE 49: THE SAME SAMPLE AS FIGURES 43-48, BUT THIS IMAGE DEPICTS THE YIELDS FOR THE SECONDARY IONS WITH A MASS-TO-CHARGE RATIO OF 283 M/Z. THIS SECONDARY ION IS THE SECOND MOST FREQUENT FRAGMENT FOR THE THIOFLAVIN T MOLECULE AS DETERMINED IN EARLIER EXPERIMENTS. 107

FIGURE 50: SAME TISSUE AS FIGURES 43-49, BUT THE TISSUE HAS BEEN STAINED ACCORDING TO THE STAIN PROTOCOL DESCRIBED IN SECTION 7.2.3. TOTAL ION COUNT FOR WILD-TYPE MOUSE BRAIN ANAYLSIS - HIPPOCAMPUS AND ISOCORTEX SHOWN. POST-STAIN ANALYSIS WAS DONE WITH THE FOLLOWING PARAMETERS: C_{60}^{+} PRIMARY ION BEAM, SPOT SIZE 7.8 MM, CURRENT 19 PA, TILE SIZE 250 MM X 250 MM, PIXELS 32 X 32, ION DWELL 200 SHOTS, DUTY CYCLE 23%, TOTAL ION DOSE 2.02E12 IONS/CM^2. A STAGE BIAS OF 40 VOLTS WAS ADDED TO THE SAMPLE. 110

FIGURE 51: SAME TISSUE SAMPLE AS FIGURES 43-50, BUT THIS IMAGE DEPICTS THE YIELDS FOR THE SECONDARY IONS WITH A MASS-TO-CHARGE RATIO OF 267 M/Z - THE CHARACTERISTIC FRAGMENT OF THIOFLAVIN T. THIS TISSUE HAS BEEN ANALYSED POST-STAIN BUT THERE ARE NO AREAS OF HIGH INTENISTY, WHICH IS CONSISTENT WITH THE EXPECTATION THAT NO AMYLOID AGGREGATES WOULD BE PRESENT IN THE WILD-TYPE MICE. THIS IMAGE WAS PROVIDED TO ILLUSTRATE THAT THE STAIN IS NOT RESPONSIBLE FOR PRODUCTION OF AREAS OF HIGH INTENSITY SECONDARY IONS THAT ARE SEEN WHEN AMYLOID-BETA AGGREGATES ARE PRESENT..... 111

FIGURE 52: SAME TISSUE SAMPLE AS FIGURES 43-51, BUT THIS IMAGE DEPICTS THE YIELDS FOR THE SECONDARY IONS WITH A MASS-TO-CHARGE RATIO OF 283 M/Z – THE SECOND MOST ABUNDANT ION FROM THIOFLAVIN T. LIKE THE IMAGE ABOVE, ONLY A

BACKGROUND FROM THE STAIN IS SEEN AND NO AREAS OF HIGH INTENSITY ARE FOUND. 112

FIGURE 53: FLUORESCENT MICROSCOPY IMAGE OF THE HIPPOCAMPAL REGION OF THE TISSUE USED IN FIGURES 43-52. TISSUE WAS IMAGED AS DESCRIBED ABOVE IN SECTION 7.2.3. NO AREAS OF FLUORESCENT INTENSITY (LIKE ARE SEEN IN FIGURE 37) ARE SEEN IN THIS IMAGE. THIS LACK OF FLUORESCENT INTENSITY/AMYLOID PLAQUES IS TO BE EXPECTED SINCE THIS IS A WILD-TYPE TISSUE SAMPLE. 113

FIGURE 54: TOTAL ION COUNT FOR 3XTG-AD MOUSE MODEL BRAIN ANAYLSIS - HIPPOCAMPUS AND ISOCORTEX SHOWN. PRE-STAIN ANALYSIS WAS DONE WITH THE FOLLOWING PARAMETERS: C_{60}^{+} PRIMARY ION BEAM, SPOT SIZE 4.5 MM, CURRENT 12 PA, TILE SIZE 290 MM X 290 MM, PIXELS 64 X 64, ION DWELL 500 SHOTS, DUTY CYCLE 12%, TOTAL ION DOSE 2.19E12 IONS/CM^2. A STAGE BIAS OF 40 VOLTS WAS ADDED TO THE SAMPLE. 115

FIGURE 55: THE SAME SAMPLE AS FIGURE 54, BUT IMAGE DEPICTS THE YIELDS FOR THE SECONDARY IONS WITH A MASS-TO-CHARGE RATIO OF 125 M/Z - A FRAGMENT FROM THE PHOSPHATE HEAD OF A PHOSPHONOSPHINGOLIPID. ONCE AGAIN, THESE PHOSPHATE HEADS ARE PRESENT THROUGHOUT THE HIPPOCAMPUS AND ISOCORTEX REGIONS, BUT VERY FEW ARE FOUND IN THE WHITE MATTER. 116

FIGURE 56: THE SAME SAMPLE AS FIGURES 54 & 55, BUT IMAGE DEPICTS THE YIELDS FOR THE SECONDARY IONS WITH A MASS-TO-CHARGE RATIO OF 184 M/Z. THIS FRAGMENT IS A LARGER ION FROM THE PHOSPHATE HEAD OF A PHOSPHONOSPHINGOLIPID. 117

FIGURE 57: THE SAME SAMPLE AS FIGURES 54-56, BUT THIS IMAGE DEPICTS THE YIELDS FOR THE SECONDARY IONS WITH A MASS-TO-CHARGE RATIO OF 369 M/Z - A FRAGMENT OF CHOLESTEROL. AS IN THE WILD-TYPE TISSUE, THE CHOLESTEROL IS SEEN IN HIGH FREQUENCY IN THE WHITE MATTER REGIONS SURROUNDING THE HIPPOCAMPUS. THE

3xTg-AD tissue does however have less cholesterol in the hippocampus or isocortex than the wild-type tissue. 118
Figure 58: The same sample as Figures 54-57, but this image depicts the yields for the secondary ions with a mass-to-charge ratio of 385 m/z. This secondary ion is a larger fragment of cholesterol, but a less frequent secondary ion when compared to the cholesterol ion with a charge-to mass ratio of 369 m/z. 119
Figure 59: Same tissue sample as Figures 54-58, but this image depicts the yieids for the secondary ions with a mass-to-charge ratio of 267 m/z - the characteristic fragment of Thioflavin T. This a control showing that no areas of high intenisty can be seen prior to staining. 120
Figure 60: Same tissue as Figures 54-59, but the tissue has been stained according to the protocol described in section 7.2.3. Total Ion Count image of 3xTg-AD mouse model brain anaylsis - hippocampus and isocortex shown. Post-stain analysis was done with the following parameters: C_{60}^{+} primary ion beam, spot size 4.5 mm, current 11 pA, tile size 290 mm x 290 mm, pixels 64 x 64, ion dwell 500 shots, duty cycle 13%, total ion dose 2.18E12 ions/cm^2. A stage bias of 40 Volts was added to the sample. As was seen in the wild-type tissue, the ethanol washes dissolved most of the lipids resulting in less pronounced white matter. 123
Figure 61: Same tissue sample as Figures 54-60, but this image depicts the yields for the secondary ions with a mass-to-charge ratio of 267 m/z - the characteristic fragment of Thioflavin T. The small dots of greater intensity are believed to be areas where Thioflavin T has bound to amyloid-beta aggregates and the increased concentration of Thioflavin T produced an increased secondary ion yield in those locations. The

aggregates range in size from 50 mm to 20 mm in diameter. Fluroescent imaging was used to confirm that these were aggregates (shown in Figure 30).....124
Figure 62: Same tissue sample as Figures 54-61, but this image depicts the yieids for the secondary ions with a mass-to-charge ratio of 283 m/z – the second most abundant ion from Thioflavin T. As in Figure 61, aggregates are seen in the isocortex but with less intenisty. This lesser intensity is due to the fact that this particular ion is a less abundant fragment of Thioflavin T. The co-localisation of these secondary ions provides further evidence that these areas of intensity correlate to Thioflavin T ions bound to amyloid-beta aggregates.....125
Figure 63: Fluorescent microscopy image of the tissue sample from Figures 54-62 – hippocampus and isocortex regions. Tissue was imaged as described in section 7.2.3. Several areas of fluorescent intensity are seen in this image corresponding the location of amyloid plaques. Image is a composite of several images stitched together to form a single larger image of the tissue.....126
Figure 64: Overlay of Thioflavin T characteristic fragment 267 m/z mass spectrum image and fluorescent microscopy image. Distension is strongly evident between the two images, thus overlays were very difficult to attempt. Brunelle describes this same problem in his 2013 H&E paper where SIMS images and microscopic images could not be overlaid due to variability in the tissue structure.....127
Figure 65: Adjusted overlay of Thioflavin T characteristic fragment 267 m/z mass spectrum image and fluorescent microscopy image. Images were stretched to align the likely areas of fluorescent intensity with

secondary ion intensity. Even this process failed to align the intensity areas at the top right. 128
Figure 66: Comparison of pre- and post- stained images demonstrating the consistent alignment even after washings under atmospheric pressure. A tile from the same location was blown up on the right, demonstrating the structure and form of the tissue to be consistent. 132
Figure 67: Comparison of pre-stained ToF-SIMS TIC Spectrum for aggregate and control tiles. Image on the top right is the TIC image of the pre-stained tissue. The location of the amyloid plaques is overlaid onto the image to illustrate that the aggregate tile does indeed have aggregates present. 133
Figure 68: Comparison of post-stained ToF-SIMS TIC Spectrum for an aggregate tile and a control tile. Image on the top right is the TIC image of the post-stained tissue. While there are no new ions present, the aggregate tile has greater counts for 267 m/z and 283 m/z ions. 134
Figure 69: A pre-stained cholesterol image compared with a post-stained Thioflavin T image, illustrating that cholesterol deposits were not found around the plaques for 15 month old mice. 135

List of Tables

TABLE 1: A LIST OF COMMON SIMS POSITIVE ION FRAGMENTS FOUND IN BRAIN SAMPLES 35

TABLE 2: COMPARING THE MOLECULAR MASSES OF THE SAMPLES. 50

TABLE 3: SPUTTER YIELDS FOR VARIOUS C_{60}^{+} PRIMARY ION BEAM KINETIC ENERGIES ON IRGANOX 1010 FILMS. THE RESULTS FOR THE 2007 NPL STUDY WERE FOUND WITHIN A TABLE IN SHARD ET AL. 2008 PAPER, BUT THE RESULTS FOR THE 2010 VAMAS STUDY WERE ESTIMATED FROM A GRAPH FOUND WITHIN THAT PAPER.' 52

TABLE 4: TABLE OF THE REFLECTIVITY INDEXES FOR THE FILMS USED IN THESE EXPERIMENTS. SILICON WAFERS WERE NOT MEASURED FOR THICKNESS SINCE THERE WAS NO FILM ON THE SURFACE. TECHNICALLY SILICON HAS A REFLECTIVITY INDEX OF 3.420. 60

TABLE 5: MEASUREMENTS OF FILM THICKNESSES FROM NANOCALC DEMONSTRATING THE UNIFORMITY OF FILMS USED IN THIS EXPERIMENT. Σ IS THE STANDARD DEVIATION OF THE MEASUREMENTS. 60

TABLE 6: COMPARISON OUR STUDIES WITH PREVIOUS STUDIES FOR 10 KEV C_{60}^{+}, 20KEV C_{60}^{+}, AND 40 KEV C_{60}^{+} SPUTTERING ON IRGANOX 1010 FILMS. 70

TABLE 7: CALCULATING THE NM^3/ION NUCLEON FOR 20 KEV C_{60}^{+}, 20 KEV $(H_2O)_{500}^{+}$, AND 20 KEV $(H_2O)_{4000}^{+}$ 79

List of Equations

EQUATION 1: TOTAL ION COUNT IS DETERMINED BY CURRENT (*I*) MEASURED IN (*PICOAMPS*), TIME (*T*), MEASURED IS (*S*), AND DIVIDED BY THE CHARGE OF AN ELECTRON (*E*), MEASURED IN ($A \cdot S$). 61

EQUATION 2: TOTAL ION COUNT IS A UNITLESS TALLY OF PRIMARY IONS. THE CHARGE OF AN ELECTRON HAS UNITS OF AMPS AND SECONDS. THESE ARE NEGATED WHEN MULTIPLIED BY CURRENT (*PA* CONVERTED INTO *A*) AND TIME (*S*)..... 61

EQUATION 3: CALCULATING THE ACTUAL DEPTH OF THE CRATER BY SUBTRACTING THE AVERAGE SURFACE HEIGHT FROM THE AVERAGE CRATER DEPTH. 69

EQUATION 4: CALCULATION OF THE ESTIMATED VOLUME OF THE CRATER..... 69

1. Abstract

The University of Manchester

Author: Taylor Kohn

Degree: M.Phil. in Instrumentation

Thesis Title: The Detection of Amyloid-Beta Neuroplaques Using Thioflavin T and Secondary Ion Mass Spectrometry

Date: 14 September, 2014

Secondary ion mass spectrometry excels at determining the spatial distribution of lipids in tissue, and thus has been used as a tool to elucidate the pathophysiologic mechanisms/etiology of Alzheimer's disease. However, secondary ion mass spectrometry struggles to detect larger macromolecules such as the characteristic protein plaques associated with Alzheimer's disease. This project was undertaken to determine a protocol that would identify Alzheimer's amyloid plaques using secondary ion mass spectrometry and then compare the plaque location to the lipid distribution within the diseased brain tissue. To accomplish this, samples were stained using Thioflavin T, a fluorescent molecule whose size is within the instrument's range of detection and that specifically binds to amyloid plaques. The samples were then analysed with secondary ion mass spectrometry to detect the characteristic fragment of Thioflavin T. This method proved successful and allowed for the comparison of amyloid plaque locations with the spatial distribution of various lipid species.

2. Declaration

I hereby declare that no portion of the work referred to in the thesis has been submitted in support of an application for another degree or qualification of this or any other university or other institute of learning.

3. Copyright

4. Acknowledgements

I would like to thanks the University of Manchester and the US-UK Fulbright Commission for the opportunity to come to the UK and to study at the University. I would also like to thank Professor John Vickerman for first agreeing to sponsor my scholarship application, for providing the opportunity to research in the lab, and for all the guidance and support over the past year. I would like to thank Dr. Nicholas Lockyer for co-sponsoring my master's thesis and for providing guidance as I learned about SIMS and integrated myself into the lab. I would like to give a special thanks to Dr. Sadia Sheraz, as she has been a very patient mentor despite my many mistakes. Learning how to use the J105 has been one of the most complex things I have ever done and I would never have been able to even scratch the surface of understanding without Sadia's help. I would also like to give a special thanks to Irma Berrueta Razo for all of her help learning to run and operating the J105 and for helping me to formulate my thesis. Also a huge thanks to Irma for helping me to procure the tissue samples. I would like to thank Giles for being a friend when I just arrived in Manchester and for taking me under his wing and introducing me to the basics of SIMS. Finally, a large thank you to the rest of the lab for all the camaraderie, support, and help over the past year.

I would like to thank Dr. Hervé Boutin for providing the tissue samples used in this thesis.

I would like to thank for my parents for raising me to be inquisitive and to have a love for learning. I would lastly like to thank my fiancée Jaden for all of her

support throughout this entire year; with your support and encouragement this year would not have been possible.

5. Introduction

5.1 Project Aims

The aim of this project is to identify amyloid-beta plaques in rat brains that have been transgenically modified to develop Alzheimer's disease. Since the peptide amyloid beta is too large to be detected by secondary ion mass spectrometry (SIMS) and since Alzheimer's diseased brains are studied with in this lab, this project sought a way by which to identify these neuroplaques.

Thioflavin Tis a small molecule that is known to bind to amyloid plaques. Further, Thioflavin T is small enough that it is within the range of detection by SIMS. Thus this project looks at the viability of using Thioflavin T stain to determine the location of the amyloid plaques, a task that is essential in the study of Alzheimer's disease. Hopefully this technique will allow future researchers to be able to relate the vast amount of information that can be obtained through SIMS to the location of the amyloid plaques.

Another portion of this study was to compare the sputter yields of the C_{60}^+, Ar_n^+, and $(H_2O)_n^+$ primary ion beams to determine which beam would be best for the tissue imaging of the Alzheimer's diseased mice brains. The sputter yield measures the amount of material removed by each primary ion; while most of the materials sputtered are neutral molecules, less 1% are ions, known as secondary ions, but these secondary ions are able to be analysed by mass spectrometry. While it is traditionally held that sputter yields and secondary ion yields are proportional, these

experiments explored whether the new $(H_2O)_n^+$ primary ion beam is able to produce a greater number of secondary ions without requiring a proportional sputter yield.

5.2 SIMS Introduction

5.2.1 History of SIMS

The origins of secondary ion mass spectrometry (SIMS) stretches back to when J.J. Thomason, a Mancunian by birth, observed the effect of positive ions upon a metal plate during his discharge tube experiments in the early 1900's.[1] This early observation, along with his mass-to-charge ratio discovery, laid the foundation for the field of mass spectrometry and specifically for SIMS. Nearly half a century later in 1949 at the University of Vienna, Herzog and Viehböck built a prototype SIMS instrument that was designed for analytical use. Their instrument consisted of two electrical fields; the first acted on the anode ray used to produce the beam for sputtering and the second was used to push the positive ions sputtered by the beam towards the detector. Their instrument was under high vacuum, thus enabling them to avoid losing ions due to gas scattering.[2] Later, in 1967, using a similar instrument, Herzog would partner with Helmut Liebl in Massachusetts at the American company GCA where they analysed moon rocks provided by NASA.[3]

In the late 1960s, Alfred Benninghoven developed the first instrument to perform static SIMS.[4] All previous instruments and methods had used dynamic SIMS where very high energetic primary particles with high fluence were used to bombard a sample. Such bombardment removed hundreds of monolayers each second and thus such technique could only be used for bulk characterisation of solids, yet this increased damage was necessary due to the limited sensitivity of detectors of the time. Benninghoven's technique for static SIMS instead reduced the primary ion current by several orders of magnitude thus allowing the removal of less

than 1% the very top monolayer. In order to then detect the now much-diminished secondary ion flux, Benninghoven switched from the prevalently used amplifier to a counter tube, which counted single ions allowing for increased sensitivity by a six orders of magnitude.[5] Benninghoven's instrument now allowed scientists to perform surface analysis and static SIMS became one of the most powerful and important instruments in the field of surface analysis. The next large breakthrough in SIMS instrumentation came in 1979 when Benninghoven and others replaced the quadrupole mass analyser with a time-of-flight (ToF) mass analyser. This allowed for a theoretically unlimited mass range, a solution to the limited mass range that the quadrupole offered. An additional major advantage is that because it is a parallel rather than a scanning instrument, the ToF analyser also permitted the collection of all the ions emitted. Thus was born the ToF-SIMS.[4]

5.2.2 Primary Ion Sources

Today time-of-flight mass analysers are still mainly used, but many advances have been made in regard to the primary ion source. Early techniques used inert gas ions, Ar^+ and Xe^+, which generate high yields of elemental ions and worked very well with inorganic materials.[4] Scientists, however, were becoming increasingly interested in organic materials. In the late 1980s, Briggs and Hearn began using liquid metal atomic primary ions. They created a Ga^+ primary beam, which allowed for an increased focus, thus opening up the possibilities of high spatial resolution mapping.[6] While this allowed for the detection of larger molecules such as lipids, it however failed to provide adequate ion yields to realise molecular imaging at the

smallest probe size. Ions from the sample material are formed as the primary ions bombard the sample, transferring kinetic energy from the primary ion to the atoms of the target. This sets off a cascade of collisions as the atoms impacted by the primary ion then collide with many more atoms. Some of the collisions return to the surface and force atoms or molecules to be ejected. Of all these atoms or molecules being ejected, known as the sputter yield, >99% are neutral and <1% are charged.[4] The amount of charged ions produced is related to two factors: the ionisation propensity of the sample molecules and the primary ion that causes the sputtering. Around this time, studies had found that in order to increase the ejection of secondary ion yield for larger molecules, it was necessary to get the cooperative action of multiple atoms all moving upwards at the same time.[7] Thus, in order to increase the number of atoms moving up, scientists decided to increase the size of primary ions sputtering the sample. So in 2001, Ionoptika Ltd and the Vickerman group in Manchester developed a liquid metal cluster ion beam. This ion beam used gold clusters for a primary ion with Au_3^+ being the most effective ion.[8] Soon after, IONTOF, another mass spectrometer company, came out with bismuth ion cluster beam. The effectiveness of these liquid metal cluster ion beams was readily apparent, as the secondary ion yield had in some case increased one thousand times and larger masses came into detection range.[4]

While such increases began to allow for biological tissue imaging, the quest for even better ion beams had not ceased. In 2003, the Vickerman group began using polyatomic ion beams with C_{60}^+ ions. The key to this advancement was in the increased number of atoms within the primary ion. When a C_{60}^+ ions impact with

the surface, two factors come into play: first the impact causes C_{60}^+ primary ions bonds to break apart reducing the kinetic energy that is transferred to the sample, and second the kinetic energy is now partitioned over 60 Carbon atoms, thus kinetic energy transferred to the sample is spread out over the impart zone. This however means that only a very small amount of the kinetic energy is directed at the surface of the tissue sample resulting in less damage. The result was a greater sputtering with less penetration than with gold or bismuth ions.[9] While the buckminsterfullerene ions once again increased the range of molecular detection and provided increased secondary ion yields, the SIMS community was still not satisfied. They began to wonder if they increased the size of the primary ion cluster even more, would they be able to once again increase the sputtering while decreasing the penetration? In 2001, the Matsuo group published a paper describing the use of argon ion clusters.[10] Later the Vickerman group in Manchester showed that indeed the argon ion clusters beam did have a gentler means of ejecting secondary ions with reduced damage, but there was not a uniform increase in secondary ion yields.[11] While the Ar_n^+ cluster beam was useful, the desire for even greater secondary ion yields still remained. In 2013, along with Ionoptika, the Vickerman group engineered their Ar_n^+ cluster ion gun so that it could also produce water ion clusters. Early studies comparing $(H_2O)_n^+$ ions to Ar_n^+ ions found an increase in signal of ten to fifty times (Figure 1, next page). It still remained unknown if this increase in signal was due simply to a general increase in sputtering (that is, total material removed) or if the water ions were actually more adept at ionising molecular fragments and thus increasing the secondary ion yield.

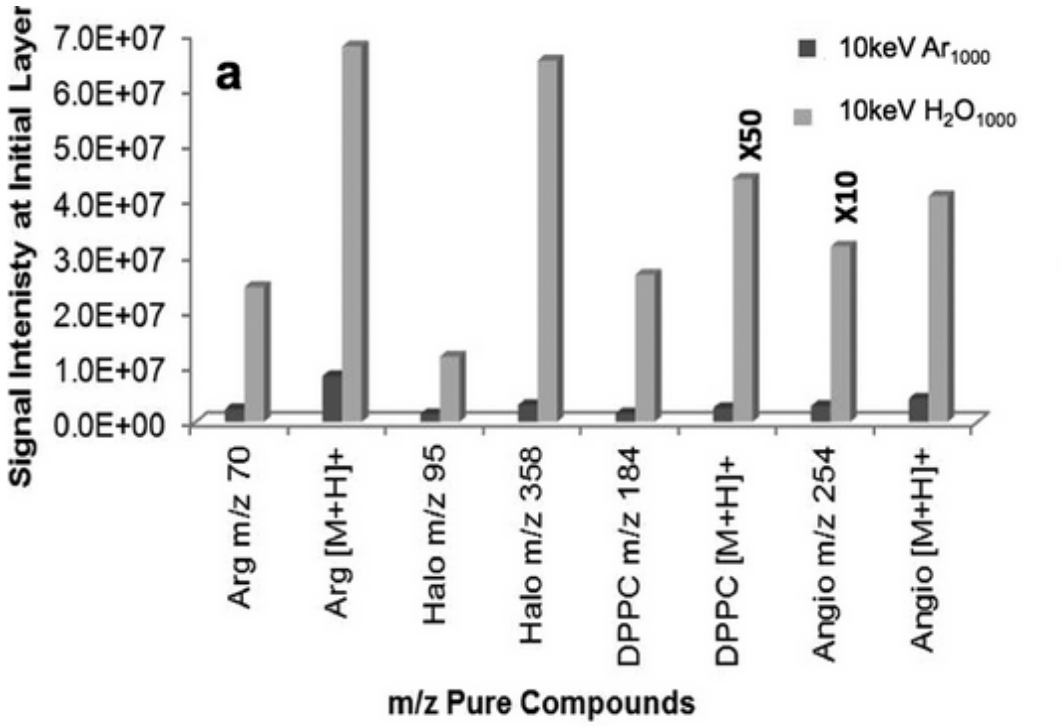

Figure 1: Comparison of signal intensity for 10KeV Ar_{1000}^{+} beam and 10KeV $H_2O_n^{+}$ cluster ion beam on multiple films.[12]

5.2.3 J105 3D Chemical Imager

In recent years, another new technology has become available in terms of mass spectrometry instrumentation. The J105 3D Chemical Imager (Figure 2, next page) emerged from discussions between Ionoptika Ltd., Professor John Vickerman, and Dr. Nick Winograd of Penn State University. This is the instrument that was used to perform all the SIMS experiments in this dissertation. The J105 utilises three new advances: a direct current (dc) ion beam, a temporal and spatial linear buncher, and a tandem MS/MS capability.[13] Prior to this, most ToF-SIMS instruments utilised a pulsed primary ion beam, which permitted time between

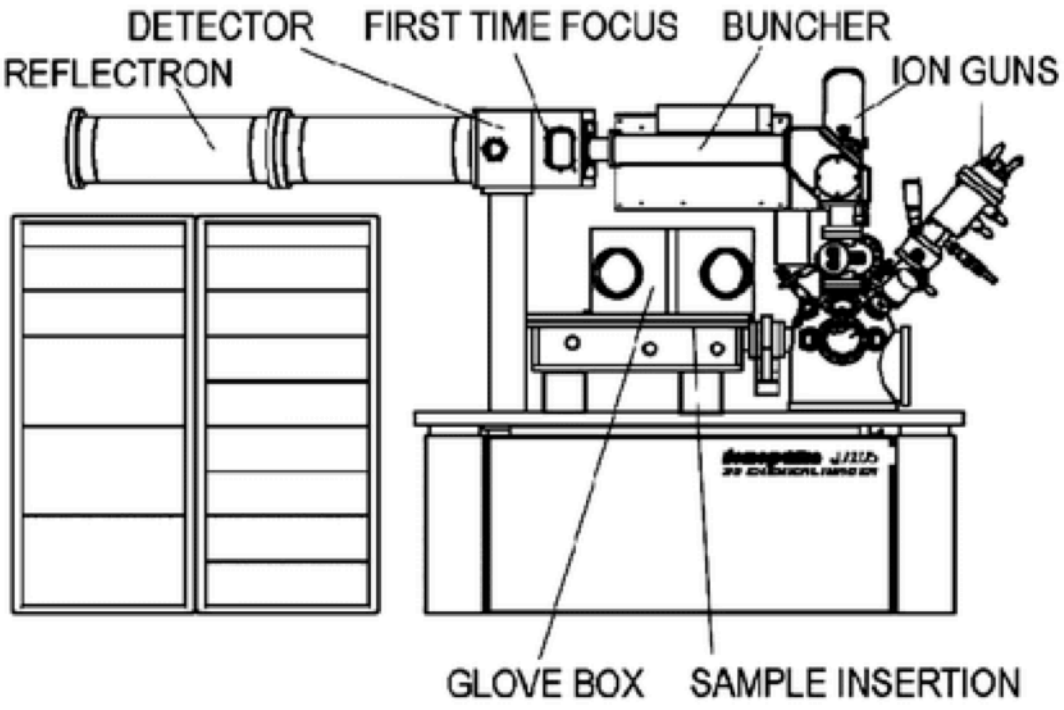

Figure 2: Schematic of the J105 3D Chemical Imager produced by Ionoptika in Southampton, UK.[14]

pulses for secondary ions to be sent from the sample to the time-of-flight mass analyser detector, thus giving time for the analyser to handle the load. Instead, the DC primary ion beam of the J105 is constantly creating secondary ions allowing for an increase in mass resolution as well as spatial resolution.[15] To manage the constant creation of secondary ions, a linear buncher has been added to the time-of-flight analyser. The buncher is first filled with secondary ions that have been sent up from the sample, and then the buncher applies an acceleration field, 7 keV at the entrance of the buncher and 1 keV at the end, forcing the secondary ions to fire through the buncher towards the ToF analyser.[14] This acceleration creates a time and spatial focus as the secondary ions exit the linear buncher and enter into the ToF analyser. Since the secondary ions are all traveling at different speeds as they leave

the buncher, a special harmonic field ToF reflectron is needed. This allows the secondary ions to be analysed based on only their mass to charge, and not their energy. Finally, two filters are applied so that MS/MS can be performed, thus allowing for an even greater identification of compounds. The J105 3D imager, in combination with its DC polyatomic cluster ion beams, allows for efficient imaging of tissue and even makes 3D imaging a possibility – a task that would take other ToF-SIMS instruments much too long.[16]

5.2.4 SIMS use in Biological Samples

In the early 1970's, SIMS was first used to characterise renal tissue and red blood cells.[17] Today as ion beams have progressed and allowed for an increase in high spatial resolution mapping, imaging of biological tissues has become quite common. For tissue imaging, the primary ion beams most often used are either a liquid metal ion source, such as Au_{1-3}^{+} or Bi_{1-7}^{+}, or a polyatomic ion beam, such as C_{60}^{+} or SF_5^{+}.[18] One benefit of using a liquid metal ion source is that they provide sub-500 nm spot size. The spot size describes how focused the beam is when it impacts the sample. The spot size is also used to determine the optimum size of each pixel: if a spot size is 500 nm, then each resulting pixel for that image can be made as small as 500 nm. Another benefit to a cluster ion from liquid metal ion source is that it creates a large amount of secondary ions. This increase in secondary ions, however, comes at the cost of increased chemical damage done to the sample.[4] This is where polyatomic ion beams excel; as they impact the sample, the energy is partitioned between the atoms of the primary ion and thus less damage is done to the

sample.[19] Today polyatomic ion beams are able to provide as focused a spot size as the liquid metal ion sources, as C_{60}^+ primary ion beams have been able to achieve spot sizes of 150 nm but Ar_n^+ cluster beams have yet to go below a spot size of 2 μm.[20]

Beyond renal tissue and erythrocytes, ToF-SIMS has been utilised to image the human spinal cord, mouse bone marrow, rat cardiac tissue, xylem transport tissue in maple trees, osteoarthritic human cartilage, mouse duodenum, and human cancer cells - just to name a few.[21-27] Using this technique allows for label-free analysis and identification of small molecules and fragments of larger macromolecules. These images provide an insight into the spatial localisation of molecules where antibodies and staining dyes are not required. Over the years, many have contributed to the ever-growing library of fragments, making identification of the mass spectrum even easier. Table 1 is a list of common positive fragments found in the most brain samples derived from a 2011 paper by Nicholas Winograd.[28]

Molecule	Label	Mass	Formula	Species	Reference
Cholesterol	CH	369.3	$C_{27}H_{45}$	$[M+H-H_2O]^+$	29, 30, 31
--	CH	385.3	$C_{27}H_{46}O$	$[M-H]^+$	29, 30
Phosphonosphingolipid	(2-AeP)	126	$C_2H_9NPO_3$	Fragment	32
--	(2-AeP)	184	$C_5H_{15}NPO_4$	Fragment	33
5-hydroxypentanoic acid	CH	115.0	$C_5H_7O_3$	$[M-2H]^+$	34

Table 1: A list of common SIMS positive ion fragments found in brain samples.[28]

While many molecules have been characterised in the literature, one challenge in SIMS imaging is that most biological molecules have yet to be chronicled.[35] If an investigator is interested in localising a particular molecule not previously addressed in the literature, a film of solely that molecules

must be made to determine that molecule's distinctive fragmentation pattern. These films are often made by dissolving the molecule of interest in ethanol, water, or chloroform and then adding the solution to a conductive substrate such as a silicon or indium tin oxide. The samples are dried by either spin coating or freeze drying, creating a uniform film.[36] The films are then analysed with SIMS resulting in a unique fragmentation pattern often with one ion being the most dominant. Upon analysing the sample tissue, the molecule of interest can then be located by finding that molecule's distinctive ion fragment.[37]

Another challenge in SIMS tissue imaging is sample charging which causes a loss of signal – often presenting as a dark spot on an image (Figure 3).

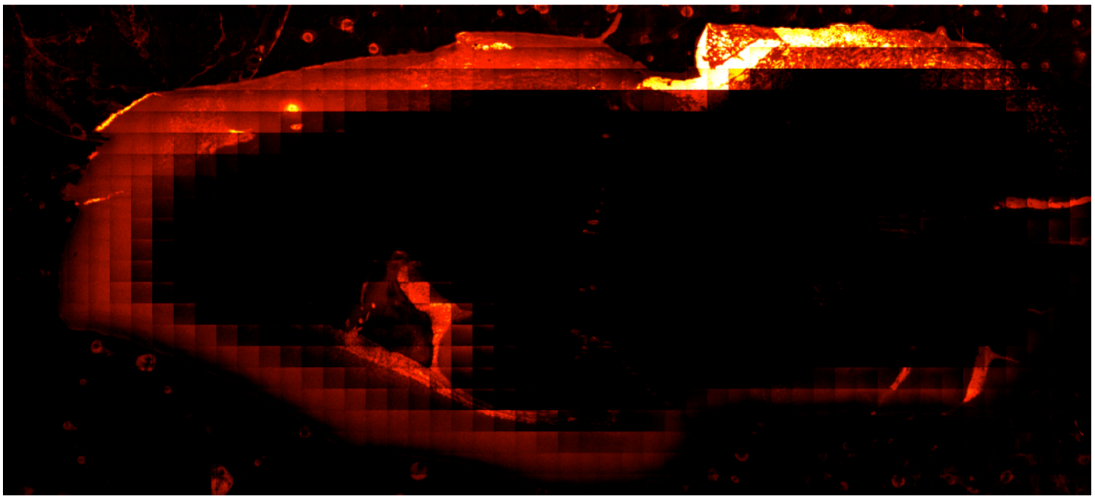

Figure 3: Example of charging. Rat wild-type brain was run at: 20KeV C_{60}^{+} primary ion beam, 22V Bias, Ion Dose 2.05E12 ions/cm^2, Spot Size 7.5µm. When the bias was increased to 45V the sample ceased to charge.

The bombardment of charged primary ions combined with the ejection of secondary ions and electrons forms a flux. This flux of the incoming and outgoing charged particles can cause the sample to be positive or negative depending which charge is lost the most.[38] This net charge can cause the primary ions to be deflected away from the region of interest or hinder the ejection of secondary ions, resulting in a loss of signal.[39] Charging is often worse with thicker tissue samples, thus it is important to use as thin a sample as possible. To counter balance charging, the J105 uses a stage bias can be added to the sample. The stage bias simply adds a voltage to the stage that helps to compensate for the flux of the incoming and outgoing charged particles on the tissue's surface. While adding a stage bias can help to minimise charging, increasing the stage bias too much will reduce the flux of charged particles too much leading to a loss of signal – thus the right balance needs to be found for each tissue type.

Another issue to consider during SIMS imaging is tissue damage. While primary ion bombardment causes the ejection of secondary ions, this bombardment can also do extensive chemical damage to the sample. The primary ions can implant into the sample, surrounding surface molecules can be fragmented and distorted, and the mixing of atoms can all occur. Thus upon each primary ion bombardment, a crater of damage is left; the size of this crater depends both on the composition of the sample and on the primary ion beam. This crater is defined as the damage cross-section, σ, and this is an area whose molecular spatial orientation is no longer unaffected. It becomes important that no primary ion hits again in a previously damaged area or else the information gathered would not reflect the molecular structure of the original tissue but rather would be recording damaged tissue (the

essence of the static SIMS approach).[4] In 1981, Benninghoven estimated that the damage cross-section for an Ar^+ primary ion beam on peptide film was 10^{-14} cm^2.[40] Thus, it has been calculated that for static conditions to apply the ion dose ought not to exceed 10^{13} ions/cm^2.[41] More recently, it has been shown that polyatomic primary ions, C_{60}^+ and SF_5^+, only have a damage cross-section of 10^{-15} cm^2, thus making it possible to surpass the static limit with these primary ions beams.[42,43] The beauty of the new polyatomic cluster ion beams is that it is possible bombard more than 1% of the surface since the chemical damage caused by the polyatomic cluster ion beam is minimal. Thus it is possible to analyse one sample multiple times without having to worry about re-analysing damaged tissue.

Finally, sample preparation must be considered when working with tissue samples. The most common type of sample preparation and the procedure used in the experiments described in this thesis is cryo-sectioning. Cryo-sectioning is performed by immediately freezing the tissue sample after animal sacrifice. The desired sample is removed from the animal and then flash frozen in liquid nitrogen. The tissue requires such rapid freezing in order to preserve the *ante mortem* condition of the tissue.[4] In order to obtain workable samples, the frozen tissue has to be sliced using a cryostat to create 8μm - 20μm thick sections. These super thin sections are then carefully placed onto a conductive wafer such as silicon or indium tin oxide. The newly sectioned samples can be stored in an -80°C freezer for up to several months or can be allowed to thaw and used immediately.[44] In these experiments, the tissues were placed back into the -80°C for several weeks and then desiccated at room temperature under vacuum for one hour before being placed into

the TOF-SIMS.[45] This use of desiccation helps to reduce the chemical dispersion of lipids and decomposition in the tissue.

5.2.5 SIMS Imaging of the Brain and Alzheimer's Disease

The brain is an excellent tissue for ToF-SIMS analysis due to the abundance of lipid species found in the white and grey matter and of metabolites that cannot be analysed through blood analysis. SIMS has been used to image the lipids surrounding "song control nuclei" of zebra finch brains, abnormal distribution of boron-containing amino acids in rat gliomas, qualification of aluminum in the human brain, and lipid distribution in Alzheimer's disease patients.[46-49] The focus on the study of neurodegenerative diseases, such as Alzheimer's disease, has increased over the reason years as these diseases have become increasingly diagnosed. SIMS, with its unique ability to determine the spatial localisation of lipids and metabolites, seems like an ideal instrument for the study of Alzheimer's disease since several studies have suggested an abnormal lipid metabolism or interaction may be present in diseased patients.[50-52] While lipid abundance studies are essential, they fail when lipid distribution is not correlated with the location of the amyloid plaques associated with Alzheimer's disease. Therefore in this thesis, the focus will be upon determining a method by which the amyloid plaques can be located.

5.3 Alzheimer's Disease Introduction

5.3.1 Statistics of Alzheimer's Disease

Alzheimer's disease is a neurological disease that causes a progressive decline of cognitive ability, ultimately resulting in the death of the patient. Alzheimer's disease currently has no cure and the diagnosis is difficult as postmortem histological stains of the brain are the only definitive diagnosis.[53] In 2013, there were estimated to be 5 million patients in the United States and 800,000 in the UK who were suffering from dementia thought to be Alzheimer's disease.[54,55] Worldwide, in 2013, there were estimated to be 44.4 million cases of Alzheimer's disease with this number expected to increase to 75.6 million by 2030 and 135.5 million by 2050.[56] Currently, one in every nine Americans over the age of 65 is diagnosed with dementia thought to be associated with Alzheimer's disease.[54] Recent studies have reported that nearly 500,000 patients in the United States and 60,000 patients in the UK die each year due to Alzheimer's disease.[54,55] In 2011, three-quarters of Americans knew someone who had the disease or had passed away from Alzheimer's disease. As a result, this disease is now the second most-feared disease in America and 22% of Americans state that they are most afraid of getting Alzheimer's disease.[57]

5.3.2 Clinical Progression of Alzheimer's Disease

As a neurodegenerative disease, Alzheimer's ultimately leads to death as the neurons in the brain eventually decay, but for many, death is a release from a long and debilitating disease. Alzheimer's disease has six clinically defined stages: first a

clinically symptom-free period, followed by five stages with varying, worsening degrees of cognitive impairment (Figure 4).[58] Physicians often measure cognitive ability with a mini-mental state examination, a thirty-question survey that helps to diagnose dementia.

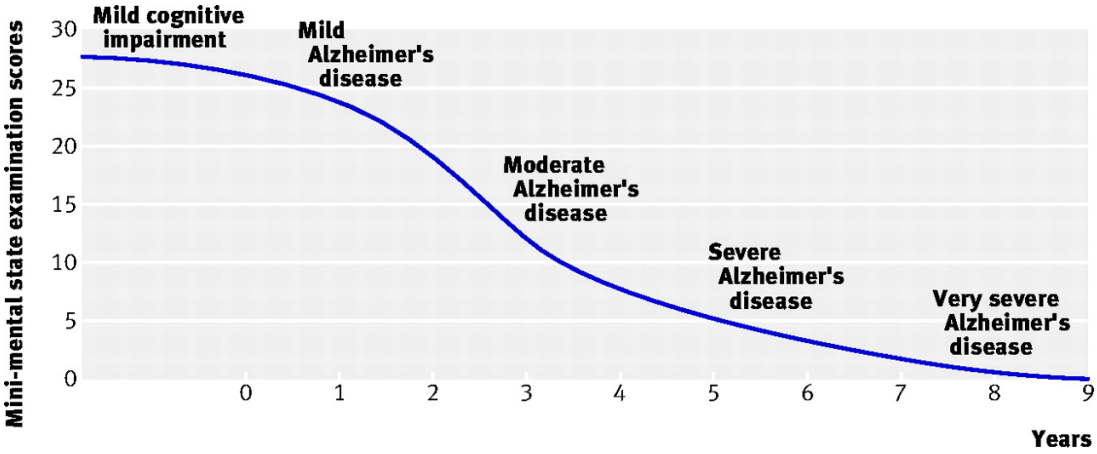

Figure 4: The five stages of clinical symptoms associated with Alzheimer's disease. [59]

The first of stage of Alzheimer's disease is when the patient experiences no impairment and function is normal. While memory and cognitive ability at this time are unimpaired, the underlying pathophysiological disease processes have begun in the brain.[60] The pre-symptomatic stage can often last 20 to 30 years as neuroproteins aggregate to form neuroplaques and tangles in the hippocampus.[61] It is only once these neuroplaques and tangles reach a certain threshold that clinical symptoms appear. This manifestation of symptoms brings on the second stage of Alzheimer's disease, known as mild cognitive impairment. At this stage, the patient might experience some lapses in memory – occasionally forgetting common words or the location of frequently used items. However, these lapses are not regular enough that the patient, their family and friends, or a physician would notice.[59]

The third stage is classified as mild Alzheimer's disease. In this stage the neuroaggregates begin to appear not only in the hippocampus but also now in the frontal lobe and temporal lobe of the brain. The temporal lobe is responsible for speaking and understanding speech while the frontal lobe of the brain is responsible for thinking and planning.[62] Thus, at this stage of the disease, the patient noticeably struggles to come up with names or the right words, forgets material that they have just read, and has difficulty with planning and organising.[63] Despite the decrease in cognitive ability, medical professionals performing a mental state examination still might not be able to diagnose dementia. It is only in the fourth stage, moderate Alzheimer's disease, when the symptoms become obvious. Patients begin to forget recent events, lose their ability to remember what day it is, and become increasingly moody and withdrawn. During this period of the disease, the proteins that support the walls of the neurons are aggregating and neurons are decreasingly receiving nourishment and removing waste.[64]

During the fifth stage, cognitive ability radically declines as patients begin to forget their personal history, experience major personality and behavioral changes, and need increasing help with activities of daily living (ADLs), including eating, dressing, and handling toiletries. The patient is able to distinguish between familiar and unfamiliar faces, but is mostly unable to remember why someone's face is familiar.[63] At this period, the neuroprotein aggregation is widespread throughout the cortex and the brain begins to shrink due to neuronal death (Figure 5, next page). In the sixth and final stage, very severe Alzheimer's disease, the patient becomes unable to have conversations, care for themselves, or even remember their own name. The brain has atrophied significantly due to neuronal death, and muscle

movement and swallowing become increasingly difficult. Patients will often die to an infection - since the immune system is very weak – or due to malnutrition – as the patient is no longer able to swallow.[65]

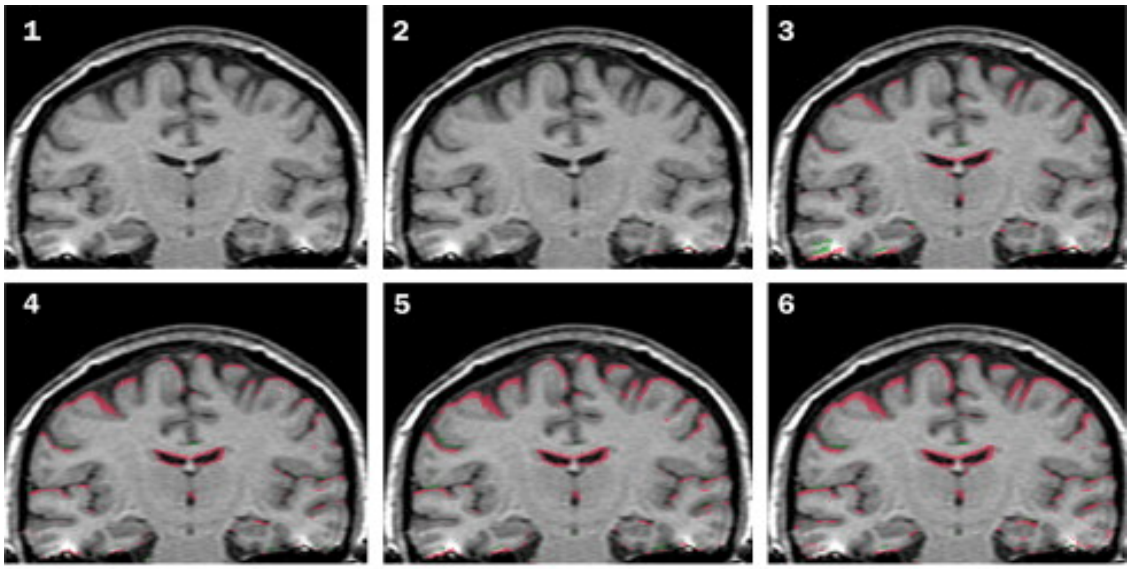

Figure 5: T1-weighted MRI scans of an initially asymptomatic patient with genetic familial Alzheimer's disease. Scans were done over a 4-year period and the first symptoms of Alzheimer's disease were recorded between image 4 and 5. The red areas indicate loss of brain volume as the disease progresses. [66]

On average the time from first symptom to death is 8.5 years, but some patients may live as long as 20 years after presentation of their first symptoms.[67] This disease slowly debilitates the mind and the patient gradually forgets all about themselves and their loved ones. Perhaps Pat Roberson best captures the true rawness of this disease: "I hate Alzheimer's. It is one of the most awful things because, here is a loved one, this is the woman or man that you have loved for 20, 30, 40 years, and suddenly, that person is gone. They're gone. They are gone".[68]

5.3.3 Pathophysiology of Alzheimer's Disease

Alois Alzheimer first described the neurotangles and neuroplaques present in this disease in 1907.[69] While the causes of this disease are unknown, several theories have been proposed.[63] This dissertation will focus mainly on the most widely accepted theory, the Amyloid Cascade Hypothesis. This hypothesis postulates that aggregates of the neuroprotein amyloid-beta are the toxic species that cause the pathology of Alzheimer's disease.[70] The theory further posits that the formation of the plaques is due to an imbalance between production and clearance of amyloid-beta. As this imbalance increases, more and more free amyloid- beta exists which eventually leads to the formation of neurotangles and neuroplaques.

In 1985, scientists determined that the peptide amyloid-beta formed the core of the neuroplaques.[71] Amyloid-beta is a 37- to 49-amino acid peptide, but it is believed that amyloid-beta is most toxic when it is 40 to 42 amino acids in length.[72] Amyloid-beta is a fragment of a larger protein, cleverly named amyloid precursor protein, which is an integral membrane peptide partially responsible for synaptic formation and neuroplasticity.[73,74] Two enzymes, β-secretase and γ-secretase, cleave the amyloid precursor protein to form amyloid-beta, a soluble 4 kDa peptide.[59]

The soluble amyloid-beta undergoes a conformational change to a form that is rich in beta-pleated sheets. It is in this state that the 42-amino-acid amyloid-beta acts as a prion and causes the same conformational change to occur in other amyloid-beta peptides.[72] These beta sheet peptides then begin to stack upon each other first, forming dimers, then oligomers, followed by protofibrils, and finally the

mature fibrils or plaques that are seen in posthumous autopsies (Figure 6).

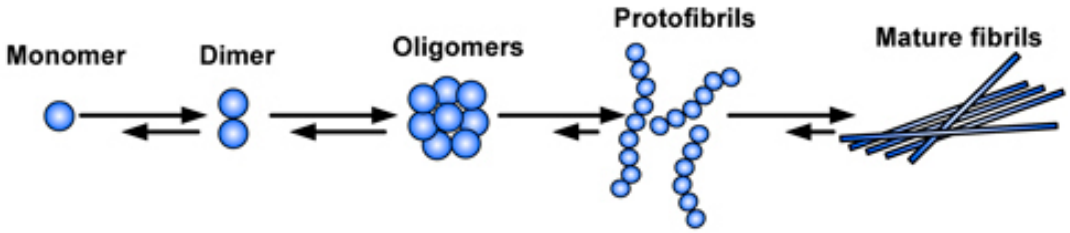

Figure 6: The process by which misfolded monomers grow to form fibrils.[75]

The oligomers range in size from three peptides to twelve or fifteen peptides before being classified as protofibrils.[59] The mature fibrils can grow to be quite large, averaging about 50 μm, but can be as large as 200 μm in humans and transgenic mice.[76] For a long time, it was assumed that the mature fibrils or neuroplaques were the toxic species, but recent research has suggested that the oligomer is the harmful form. In this new theory, the brain attacked by the harmful oligomer forms the mature fibrils as a means of protecting itself. The mature plaques have been shown to be stable and thus the formation of plaques could be an evolutionary protective mechanism.[77] This theory has become quite popular in neurodegerative disease research in the last 5 years. While much of the underlying research has been promising, not enough time has passed for drugs to come to market based on this new theory.

In both diseased and healthy cells, clearance of the prion peptide is modulated by a host of enzymes or low-density lipoprotein receptor-related protein; thus, many postulate that the issue is not in the clearance of amyloid-beta because there are too many different systems that would need to fail in order to produce disease.[78,79] Instead, it may be an excess of production of amyloid-beta, such that the clearance is not able to keep up; this hypothesis is supported by many cases of

familial Alzheimer's disease. Familial Alzheimer's disease, unlike sporadic Alzheimer's disease, has a specific gene mutation that is genetically inherited and the symptoms present much earlier. One example of this is where the amyloid precursor protein has a duplication causing an overexpression of amyloid-beta.[80] These patients will have excess production of amyloid-beta since the overexpression of amyloid-beat exceeds the rate of clearance resulting in an accumulation of the peptide within the cell.

5.3.4 *In Vitro* Detection of Amyloid Plaques

For researchers and pathologists, it is necessary to use dyes in order to detect the plaques, which otherwise are unable to be seen by the naked eye. Alois Alzheimer first used Congo Red, an azo dye, to identify the strange deposits back in 1907.[69] Congo Red is still used today by pathologists performing autopsies since Congo Red bound to amyloid plaques gives off an apple-green birefringence (Figure 7) when viewed with a polarised light source, making identification rather simple.[81]

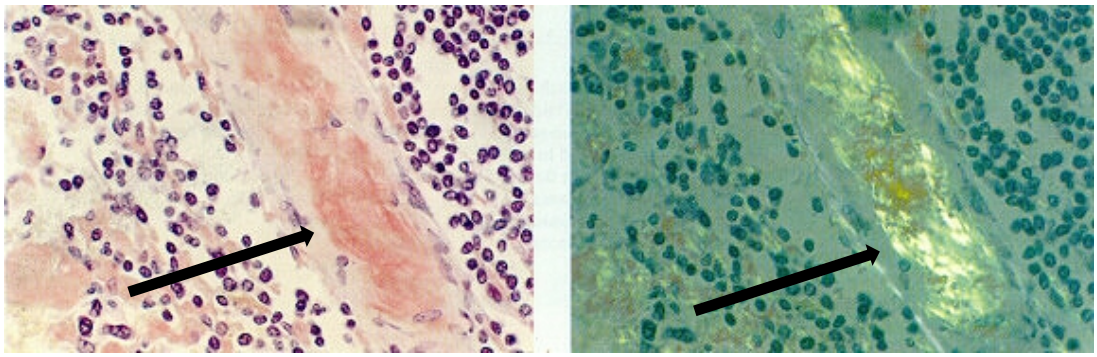

Figure 7: Left: Amyloid plaques stained with Congo Red and viewed under a microscope with normal light. Right: The same sample but viewed with a polarised light, demonstrating the "apple green" birefringence.[82]

Congo Red also has been shown to bind to amyloid-beta oligomers and protofibrils in addition to larger neuroplaques, an important characteristic with the increased focus on amyloid oligomers.[83] The use of Congo Red, however, for *in vitro* studies has recently decreased since the dye also binds to collagen, a structural protein found in abundance throughout the body.

Another amyloid dye that is commonly used is Thioflavin T, a bright yellow-green benzothiazole dye that has a molecular mass of 318.86 Daltons and a monoisotopic mass of 318.0957 (Figure 8).[84]

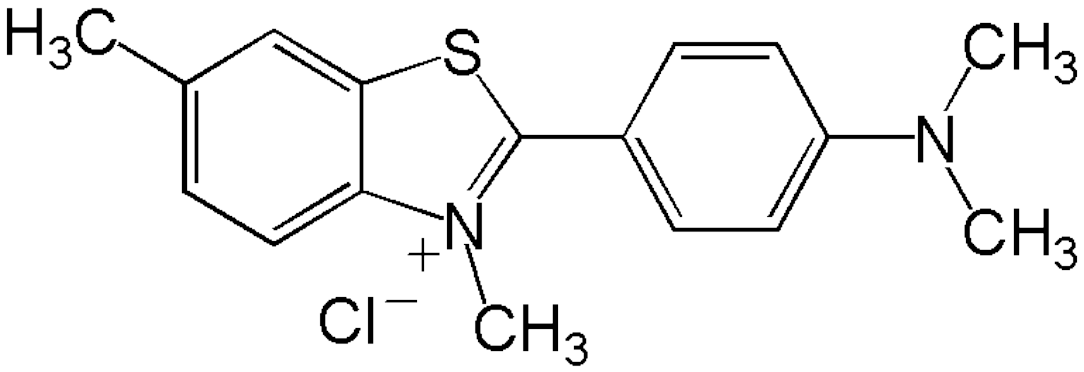

Figure 8: Structure of Thioflavin T.[84]

While Congo Red has a poor functional specificity, the fluorescent small molecule Thioflavin T excels in this area. While Thioflavin T does bind to the protein elastin and other beta-sheet rich proteins, the background tends to be diminished since elastin and other beta-rich proteins are sparse in brain samples. Upon binding to amyloid plaques and oligomers, Thioflavin T increases in fluorescent intensity and undergoes a red shift of its emission spectrum.[85] Free Thioflavin T has an excitation and emission of 350 nm and 440 nm, respectively, while bound Thioflavin T has a red-shifted excitation and emission of 440 nm and 490 nm, respectively.[86,87] Thus, the amyloid aggregates can be easily identified in an analysis using these longer

wavelengths. It is believed that Thioflavin T binds to amyloid beta by fitting into a "channel" that runs the length of the beta sheet (Figure 9, front view).

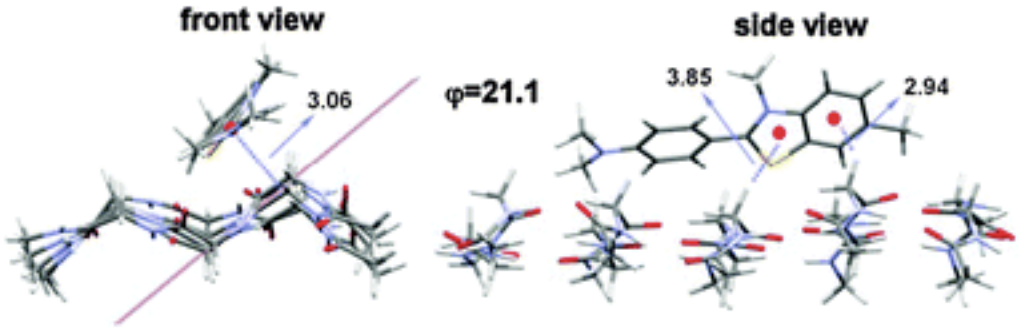

Figure 9: Computer modeling of Thioflavin T's interaction with a protein beta sheet. The figure shows Thioflavin T nestled into the "channel" running along the beta sheet and that the π orbitals of Thioflavin T's benzothiazole and a benzamine ring interact with the both the π orbital and CH groups in the beta sheet.[88]

It is hypothesised that steric interactions occur between the dye and the protein, which might explain the increase in fluorescence of Thioflavin T.[89] More recent research has suggested that the π – π and CH– π interactions between the beta sheet and fluorescent dye stabilise the Thioflavin T molecule, thus causing the increase in fluorescent intensity (Figure 9, side view). While there is believed to only be one binding site per amyloid-beta unit, it is debated whether a single Thioflavin T binds or whether the Thioflavin T binds as a dimer.[90] While this stoichiometry plays an important role in amyloid aggregation assays, it is less important in tissue staining since aggregates can be composed of thousands if not millions of monomers. Therefore, for these many reasons, Thioflavin T is the industry standard for small molecule amyloid aggregate staining.

Thioflavin S, another benzothiazole dye, is derived from Thioflavin T. To create Thioflavin S, Thioflavin T is methylated and sulfonated, resulting in a mixture of compounds with varying molecular weights and structures.[87] Unlike the brilliant

yellow-green of Thioflavin T, Thioflavin S has a muddy yellow colouration. Further Thioflavin S does not give off an increased fluorescence nor does it have a shifted absorbance spectrum. Thioflavin S is used often in aggregation studies where only purified amyloid proteins are present. Thioflavin S and Thioflavin T, however, are generally used interchangeably and give similar results since both bind to aggregates using the same mechanism.

The other industry-standard method of detecting amyloid-beta plaques is by using antibodies. This method is the most specific technique; the antibody binds to the amyloid-beta and a secondary fluorescent antibody then binds to the primary antibody. There is some concern that some of these antibodies bind to the monomer in addition to the oligomers and plaques thus giving false-positives for aggregates.[91] Since the molecular weight of these antibodies is roughly 150 kilodaltons, they are outside the scope of SIMS detection and were thus not used in this project.

6. Comparing Sputter Yields of Primary Ion Beams

6.1 Sputter Yield Introduction

6.1.1 Project Aims

The study of sputter yields for primary ion beams is essential to determine which ion beam is most adept for specific tissue studies. These experiments were performed during the first few months of my time in Manchester and thus served as a first introduction to ToF-SIMS. This data would then guide my project as I selected the primary ion beams to be used later in the rat brain analysis. These studies compared the sputter rates of three primary ion beams (C_{60}^+, Ar_n^+, and $(H_2O)_n^+$) on four thin films (Irganox 1010, L-arginine, synthetic angiotensin II and haloperidol) and an unwashed silicon wafer. These five samples were used to determine sputter yields for a variety of molecular types because of the unique properties of each and the variation in their molecular weights (Table 1); Irganox 1010 is an antioxidant, arginine is a amino acid, angiotensin II is a small peptide, the silicon wafer is an inorganic material which also formed the substrate for the thin films, and haloperidol is a small pharmaceutical molecule.

Compound	Silicon	Arginine	Haloperidol	Angiotensin II	Irganox 1010
Molecular Weight	28.08 g/mol	174.2 g/mol	375.9 g/mol	1031.2 g/mol	1177.6 g/mol

Table 2: Comparing the molecular masses of the samples.

After the films had been deposited on the silicon wafer, the thicknesses of the films were measured with a NanoCalc thin film reflectrometry system. The films were then placed inside the J105, taking note of the position of the film, and sputtered for a determined amount of time. Several craters were sputtered in each film, so care was taken to ensure that the craters did not overlap. After sputtering, the crater dimensions were measured using a digital holographic microscope, DHM, to estimate the size of each crater. Finally, the sputter yields were calculated by dividing the volume removed by the number of ions that bombarded the sample. These results were then compared with values for C_{60}^{+} primary ion sputter yields reported in the literature to validate our methods.

One of the most important parameters in the sputter yield experiments was the depth of the films. The films needed to be sufficiently thick for two reasons. First, it was important that the sputtering would not go completely through the film and into the silicon wafer. If this occurred, there would be no way to determine the sputter yield since the calculation required a consistent rate of sputtering and silicon sputters much more slowly than the films. Second, thicker films allowed for the sputtering of deeper craters, which minimised measurement variability; DHM measurements of a crater 30 to 40 nm deep were more precise than those of a crater that was 3 or 4 nm deep. Therefore for both of these reasons, the films needed to be as thick as possible. Initially, the protocols for creating the films yielded rather thin films, but by increasing the concentration of the solutions or by adding more of the solution to the wafers, we were able to make sufficiently thick films.

6.1.2 Previous Research

The measurement of sputter yields has been an important aspect of SIMS research over the years. Recently there has been a considerable incentive to find primary ion beams that provide an increased secondary ion yield while limiting the material sputtered (i.e. total damage done to the sample). Two recent studies have been performed to determine molecular sputter yields using Irganox 1010 films and C_{60}^+ primary ions.[92,93] The first of these studies was performed at the National Physical Laboratory (NPL) in Teddington, UK in 2007. This study used a single layer film of Irganox 1010; results for this study can be found in Table 3.

Kinetic Energies in keV	Results in nm^3/ion	
C_{60}^+ Energy	2007 NPL Study[92]	2010 VAMAS Study[93]
10	82 ± 8	~80 ± 10
20	163 ± 16	~ 160 ± 20
30	254 ± 25	~ 225 ± 10
40	Not Studied	~ 350 ± 200

Table 3: Sputter Yields for various C_{60}^+ primary ion beam kinetic energies on Irganox 1010 films. The results for the 2007 NPL study were found within a table in Shard et al. 2008 paper,[94] but the results for the 2010 VAMAS study were estimated from a graph found within that paper.[92,93]

The second of these studies was a VAMAS (Versailles Project on Advanced Materials and Standards) interlaboratory study performed in 2010. A total of 20 laboratories took part in this depth profiling study, including the Surface Analysis Research Centre in Manchester. This study used a multiple layer film that alternated between Irganox 1010 and Irganox 3114. The Irganox 1010 layers were

approximately 100nm thick, while the interrupting Irganox 3114 layers were only 3nm thick. Since the sputtering rates of Irganox 3114 and Irganox 1010 with C_{60}^+ primary ions only differ on average by 14.1% and since the Irganox 3114 layers were so thin compared to the Irganox 1010 layers, this data was also used for comparison.[94] Table 3 displays the results from this study as well. These previous results provided a benchmark by which we could compare our initial C_{60}^+ results and thus validate our method.

As discussed in the chapter 5.2.2, previous 10 keV $(H_2O)_{1000}^+$ cluster ion experiments have been done in this lab showing an increased yield of secondary ions when compared to the secondary ion yields of 10 keV Ar_{1000}^+ (Figure 1, page 32). Other unpublished data from the Vickerman group compares the secondary ion yield for $(H_2O)_n^+$ cluster ion and C_{60}^+ primary ions (Figure 10). This graph illustrates a seven-fold increase in secondary ions from 20 keV $(H_2O)_{5000}^+$ sputtering relative to the secondary ion yield of 20 keV C_{60}^+ primary ions. Part of this chapter is to determine if this increase of secondary ion yields is due to an increase in sputter yields or if the water is more adept at creating secondary ions.

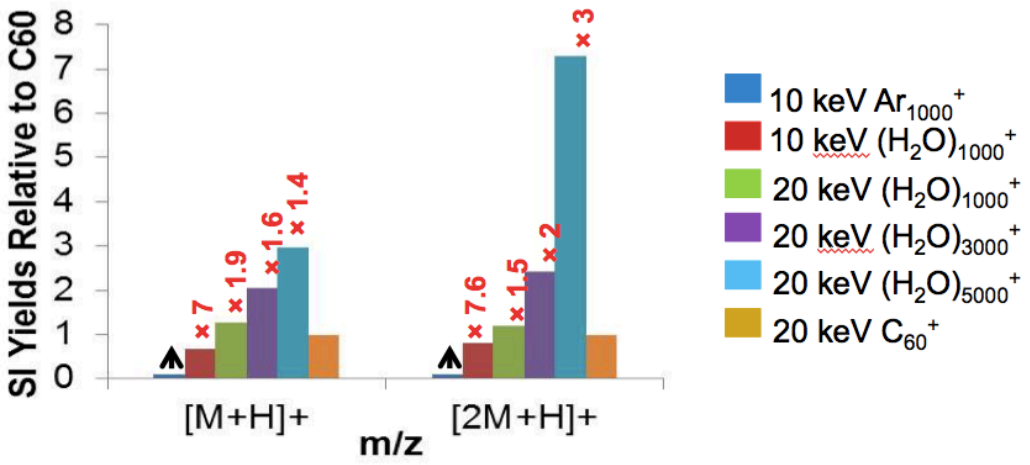

Figure 10: Arginine films secondary ion yields for various Ar_n^+, C_{60}^+, and $(H_2O)_n^+$ primary ions. An ion dose of 5E11 ions/cm^2 sputtered the sample and the secondary ion yield was determine using ToF-SIMS. Secondary ion yields were measured by Dr. Sadia Sheraz.

6.2 Sputter Yield Experimental Design

6.2.1 Irganox Film Preparation

Irganox 1010 (chemical structure depicted in Figure 11) is the molecule most commonly used in sputter yield experiments because, when dissolved and evaporated, it forms a molecular solid with excellent integrity and superb reproducibility.

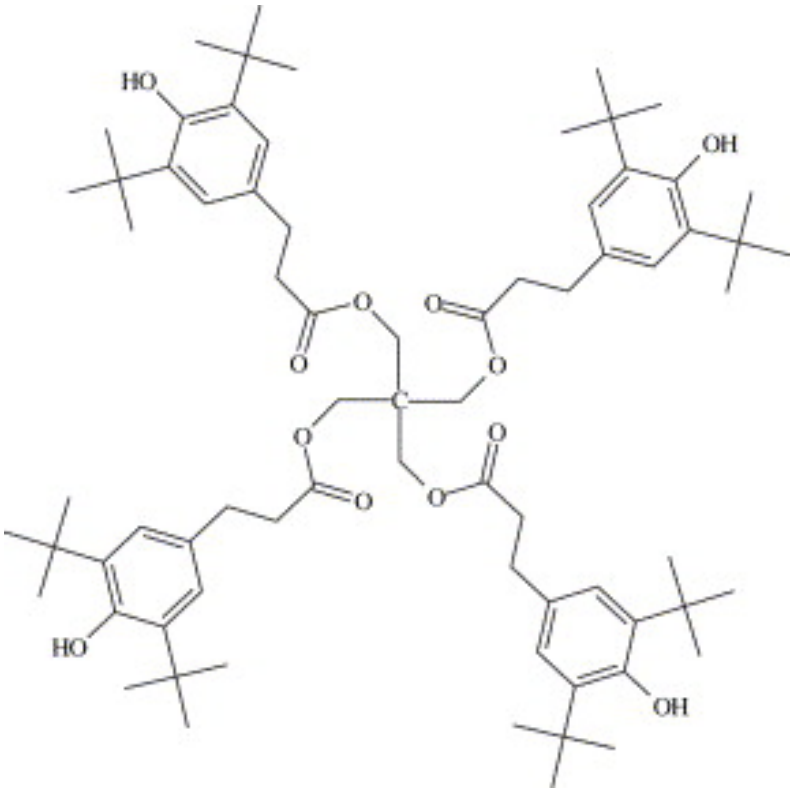

Figure 11: Molecular Structure of Irganox 1010.[95]

To create the Irganox 1010 films, new silicon wafers (Agar Scientific) was washed three times by placing the wafers into a pure chloroform solution (Fisher Scientific) and sonicated for five minutes for each wash. After the three washes, the silicon wafers were allowed to sit until dry. During the washes, 0.012 g of Irganox (Ciba

Specialty Chemicals) was weighed and dissolved in 500 µL of chloroform, creating a 20 mM Irganox 1010 solution. These solutions were then made into films using a spin caster (Laurell Technologies Corporation). The spin caster uses a vacuum to hold the silicon wafer and spins the wafer utilising centrifugal force to create uniform films. The spin caster was set to 1700 RPM and 10 µL was dispensed by pipette before the axial rotation began – known as static dispensing. Once dispensed, the spin caster was turned on, causing the Irganox 1010 solution to spread out uniformly and form a flat film on the surface of the silicon wafer. To obtain a thicker film, 10 µL was dispensed fourteen additional times while the spin caster was revolving at 1700 RPM – known as dynamic dispensing.

6.2.2 Arginine Film Preparation

L-Arginine is one of the larger amino acids, with a molecular weight of 174.2 g/mol, but arginine also makes a stable and reproducible film (Figure 12).

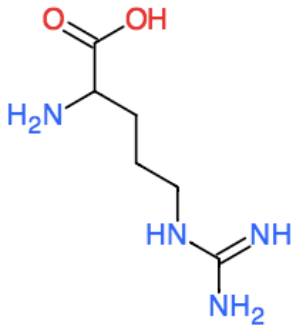

Figure 12: Chemical structure of L-arginine.[96]

This amino acid is commonly used for films in the Manchester laboratory and is found abundantly in the body and in tissue samples. To make arginine films, the silicon wafers were washed and sonicated for five minutes each in four different

solutions: first in hexane (Fisher Scientific), then water (Sigma-Aldrich), then methanol (Sigma-Aldrich), and once again in water. A 287 mM arginine solution was created by dissolving 50 mg of L-Arginine (Fluka BioChemika) in 1 mL of water. A 7 μL aliquot was pipetted onto the washed silicon wafer in static mode followed by an additional 7 μL aliquot being added in dynamic mode with the spin caster set to 6700 RMP. This produced uniform, thick, and reproducible films.

6.2.3 Angiotensin II Film Preparation

Angiotensin II is one of the larger molecules that can be detected with ToF-SIMS, but is a very small peptide with only 8 amino acids: Asp-Arg-Val-Tyr-Ile-His-Pro-Phe (Figure 13).

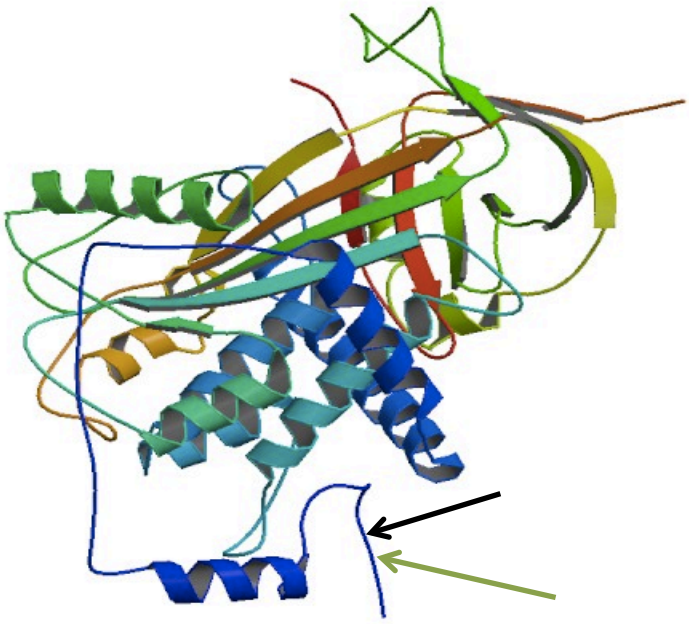

Figure 13: Space filling model of angiotensinogen, the parent molecule of angiotensin II before enzymatic degradation. The black arrow indicates where angiotensinogen is cleaved by renin to form angiotensin I. The green arrow indicates where angiotensin-converting enzymes cleave angiotensin I into the 8-amino-acid peptide angiotensin II.[97]

Angiotensin II plays an important part in mammalian homeostasis as it controls blood pressure and blood volume. Angiotensin II concentration is regulated by renin, which is released in the kidney when blood pressure or volume is too low. Renin stimulates a release of angiotensinogen from the liver and also cleaves this precursor protein into angiotensin I in the blood stream. Angiotensin I travels to lung alveoli where angiotensin-converting enzymes cleave angiotensin I into angiotensin II. Angiotensin II then travels to the adrenal gland where it stimulates aldosterone production. In turn, aldosterone causes increased water reabsorption in the kidney's nephrons, which increases blood volume and pressure.[98] While angiotensin II will not be found in abundance in the brain, we were interested to see if sputter yields differed amongst type of molecular films.

The angiotensin II films were the hardest to make consistently and often the film would be non-uniform. The angiotensin II solution was prepared by dissolving 0.3 mg of [Asn1,Val5] Angiotensin II (Cambridge Bioscience) in 250 μL of ethanol (Fisher Scientific). The silicon wafers were washed and sonicated for five minutes first with water and then twice with ethanol. 20 μL of the angiotensin II solution was then added to the silicon wafers in static mode, followed by another 20 μL added in dynamic mode with the spin caster set to 990 RPM. While most of the early films were homogenous, after many repetitions, several were produced that were fairly uniform and were usable for these experiments.

6.2.4 Haloperidol Film Preparation

Haloperidol (Figure 14) is a small pharmaceutical drug that is used to treat schizophrenia and other psychological issues.[99] The molecular mass of haloperidol

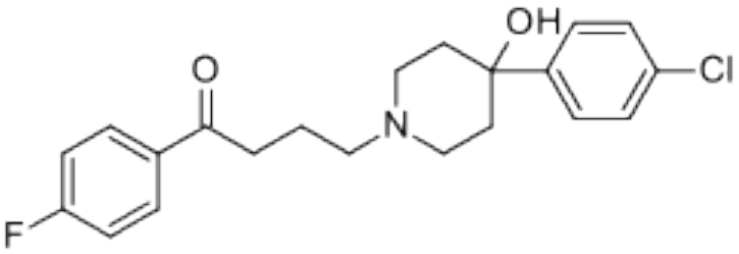

Figure 14: Chemical structure of haloperidol.[100]

is 375.9 g/mol, thus providing a mid-sized molecule for sputter yield analysis. Haloperidol forms a deep blue film that is very uniform and easily reproduced. Silicon wafers were washed and sonicated for five minutes first with methanol and then twice with chloroform. A 0.08mM haloperidol solution was made by dissolving 8 mg of haloperidol (Sigma-Aldrich) in 250 μL of a 10:1 chloroform to methanol solution. Two aliquots of 7 μL were then dynamically added to the washed silicon wafers with the spin caster set to 2700 RPM.

6.2.5 Unwashed Silicon Wafers

Our final experiments used plain unwashed silicon wafers, which provided a hard inorganic that would indicate how "hard" the polyatomic primary ions were. Previous experiments in the lab had shown that C_{60}^+ primary ions were able etch a crater in the silicon, while Ar_n^+ primary ions could sputter silicon for hours and barely leave a mark. Therefore, we were interested to see if $(H_2O)_n^+$ cluster ions

would create a crater in the silicon wafers or if they would leave them unscathed like their gas counterpart Ar_n^+ cluster ions. For many of the films, sputtering would last for a few minutes to an hour, but the sputtering of silicon lasted for several hours each time. Since previous experiments in the lab had shown extremely low rates of sputtering from Ar_n^+ primary ions, they were omitted in these experiments. While unwashed, careful care was taken to ensure that the silicon wafers to be used were clean and freshly removed from the protective coverings.

6.2.6 Measuring Film Thicknesses

In order to determine the uniformity and consistency of each film, we used the NanoCalc-XR thin film reflectrometry system from Ocean Optics (Figure 15). This instrument utilises the reflective index of the molecular film to determine the film thickness. First a blank, washed silicon wafer would be placed under the

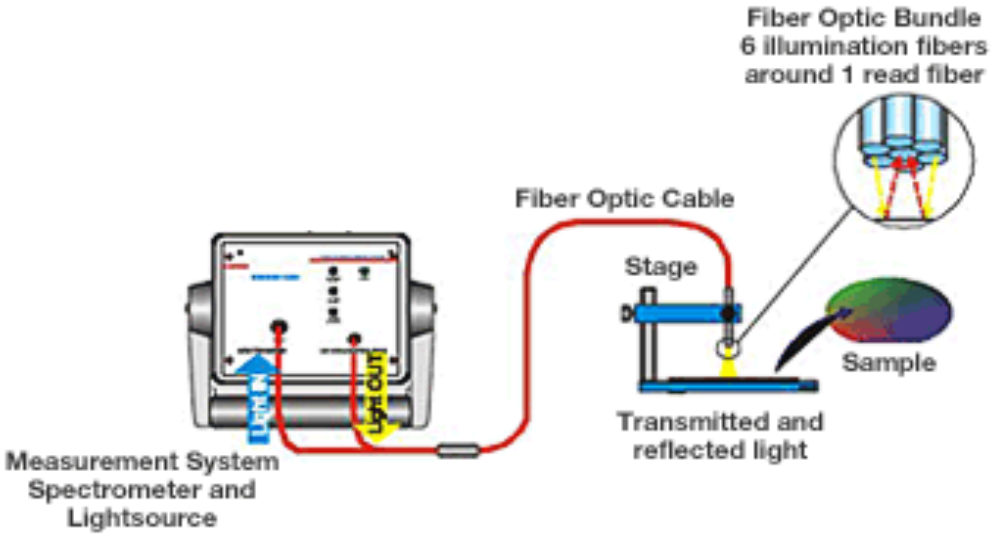

Figure 15: Schematic of The NanoCalc-XR thin film reflectrometry.[101]

fiber optic bundle with six illuminating fibers and one read fiber, which would determine the reference height of the silicon. Next the film, which had been spin-cast onto a silicon wafer similar to the reference sample, would be placed under the fiber optic bundle – being careful not to move the probe's arm and thus alter the reference height. The illuminating fibers shine down onto the film and the light from the probe passes through the film and is reflected back to the read fiber, but not all the light is reflected back to the fiber bundle as the molecules in the film disperse some of this light. Since the user tells the NanoCalc the reflectrometry index for the film, the Nanocalc then estimate the thickness of the film by measuring the intensity of the reflected light. Reflectivity indexes for the films are provided in Table 4.

Compound	Silicon	Arginine	Haloperidol	Angiotensin II	Irganox
Reflectivity Index	--	1.664	1.594	1.660	1.483

Table 4: Table of the reflectivity indexes for the films used in these experiments. Silicon wafers were not measured for thickness since there was no film on the surface. Technically Silicon has a reflectivity index of 3.420.

In order to measure the uniformity of the samples, each film was measured eight times at various points on the film. If a film had high levels of variation, it would not be used; only the most uniform of samples were used. The measurements in Table 5 are an example of the uniformity of several of the films that were used in these experiments along with the standard deviation, σ, of the measurements.

Film	Measurements in nm								
	1	2	3	4	5	6	7	8	σ
Irganox	148.4	149.2	148.7	145.0	151.0	147.1	147.1	151.0	2.04
Arginine	163.5	165.6	165.2	165.1	163.3	164.4	164.6	164.1	0.82
Haloperidol	90.8	91.0	91.9	91.6	90.9	91.0	92.1	93.0	0.78
Ang II	211.8	212.5	211.6	206.0	215.2	219.2	219.5	209.1	4.68

Table 5: Measurements of film thicknesses from NanoCalc demonstrating the uniformity of films used in this experiment. σ is the standard deviation of the measurements.

6.2.7 Sputtering

Sputtering experiments were carried out under high vacuum conditions in the J105 3D Chemical Imager (Ionoptika, Ltd.). The polyatomic ions used in these experiments were: 10 keV C_{60}^{+}, 20 keV C_{60}^{+}, 40 keV C_{60}^{+}, 20 keV Ar_{500}^{+}, 20 keV Ar_{2000}^{+}, 10 keV $(H_2O)_{500}^{+}$, 10 keV $(H_2O)_{2000}^{+}$, 20 keV $(H_2O)_{500}^{+}$, 20 keV $(H_2O)_{2000}^{+}$, and 20 keV $(H_2O)_{4000}^{+}$. The ion current for each beam would be measured on the stage before and after each sputtering experiment. Each sputtering experiment was set to raster an area of 250 nm by 250 nm. The beams rastered the films in direct sputtering for a specific amount of time. With the time and current known, the total sputtering ion count can be calculated (Equation 1):

$$Ite^{-1} = Total\ Ion\ Count$$

Equation 1: Total ion count is determined by current (*I*) measured in (*picoAmps*), time (*t*), measured is (*s*), and divided by the charge of an electron (*e*), measured in ($A \cdot s$).

Total Ion Count is a tally of all the primary ions that leave the ion gun and impact the surface of the film. This is why total ion count is unitless (Equation 2):

$$pA\left(\frac{A}{1E12\ pA}\right) \times \left(\frac{1}{A \cdot s}\right) \times s = Total\ Ion\ Count$$

Equation 2: Total Ion Count is a unitless tally of primary ions. The charge of an electron has units of Amps and seconds. These are negated when multiplied by current (*pA* converted into *A*) and time (*s*).

Initial experiments were cautious since we did not know how long to sputter each film. After learning approximate sputter rates, we were able to hone our experiments to obtain optimal depth of craters. Sputtering for silicon ranged from 45 minutes to three hours, while sputtering for Irganox lasted between 2 minutes and 10 minutes. Thus there was quite a range in how long sputtering would last.

6.2.8 Digital Holographic Microscope

In order to determine sputter yields, the total volume removed is divided by the total ion count. The ion count was calculated during the sputtering, but the total volume removed had to be determined by digital holographic microscope, DHM (Lyntec). Unlike a typical optical microscope, the DHM does not record the image; instead, it records the wavelength of light that is captured by the objective. An algorithm then reconstructs these wavelengths and a "hologram" is created. Whereas traditional microscopes use a lens to reconstruct the image, the DHM replaces this with an equation. The benefit to this type of acquisition is that both the amplitude and the phase are acquired, while normal light microscopes only utilise the amplitude of light (Figure 16).

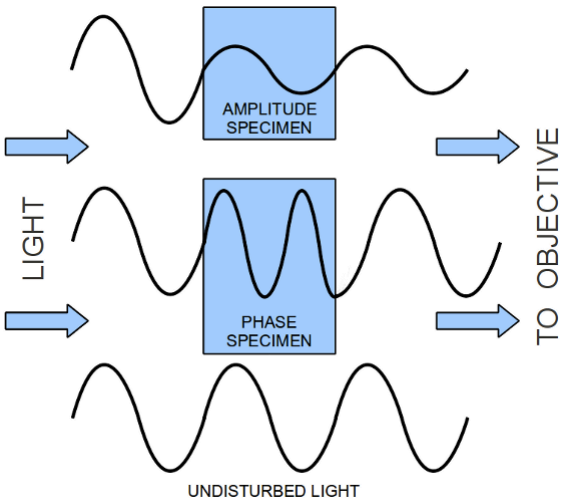

Figure 16: DHM utilises both the phase and amplitude of light to create a digital hologram.[102]

For the source of light, the DHM uses a 300 to 400 nm laser that reflects off the sample. Similar to the NanoCalc, the laser will be directed at the sample and, with the reflective index of the sample having been entered by the user, the computer calculates what ought to be reflected off of the sample. The computer generates a

predicted phase and compares this with the actual phase of the reflected light. These are then combined in the "Phase View" in the computer program "Koala" and "Medusa" that accompanies the DHM (Figure 17).

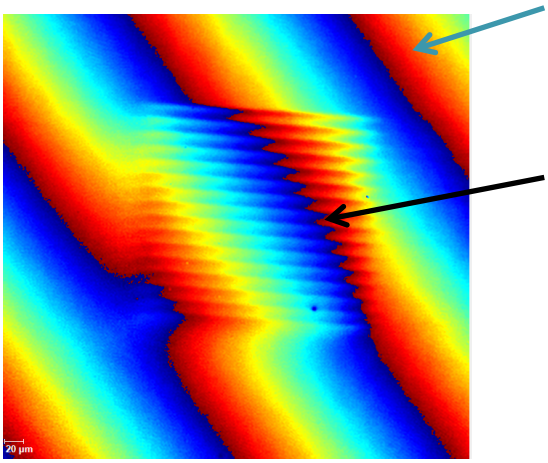

Figure 17: DHM generated "Phase View" of a crater. The blue arrow indicates an area where computer calculated phase and measured phase are the same. The black arrow indicates an area where the phase predicted and the phase measured is different.

Where the phase predicted and the phase measured are different, an interference has occurred. This can be either an area where the film has a crater or extra material on top of the film (Figure 17, Black Arrow). The computer algorithm uses these differences in phase to construct a hologram (Figure 18).

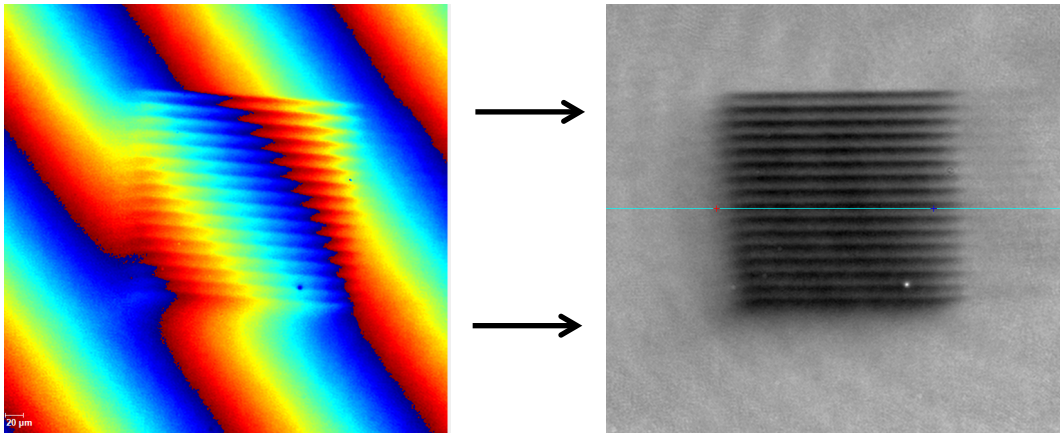

Figure 18: Computer algorithm calculates the difference in phases (left) to create a hologram (right) that contains information regarding the heights of the sample.

This newly created hologram no longer depicts changes in phase, but actually calculates variations in height. Thus, the depth of the craters can be determined.

The DHM has several limitations that had to be addressed before accurate data could be obtained. First, an estimation of the depth for the film had to be supplied to the computer program. The estimation had to be within 300 to 400 nm since phases repeat and the algorithm needed to know within which phase to calculate. To solve this problem, the thickness of the films was determined by the NanoCalc as previously described. Another limitation was that if the sample was not perfectly in focus, then there would be artificial heights and depths. Thus great care had to be taken to ensure that each sample was in focus. Finally, each sample had to be perfectly flat. If the film was not perfectly flat, then the DHM would measure this as a slope and the proper depths of the craters would be inaccurate. While many of our samples appeared to be uniformly flat, to ensure absolute flatness, we ordered four Irganox 1010 films from NPL (Figure 19). These films were made through thermal evaporation, as opposed to spin casting, giving an even more uniform surface. NPL tested the thickness of each of the films finding them to be 47.65 nm, 47.31 nm, 47.12 nm, and 47.50 nm thick. While initially the limitations of the DHM were problematic, once these solutions were implemented, the data were consistent and repeatable.

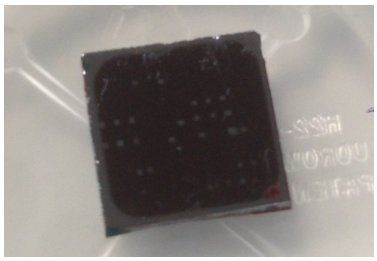

Figure 19: NPL Irganox 1010 film prepared through thermal evaporation. This photo was taken after sputter yield experiments as little squares can be seen on the film. Photo taken 10 March 2014.

6.2.9 Calculating Volume Removed

Since the holograph contained the data for the variations in heights, this could be used to calculate the volume of the crater. The craters formed by C_{60}^{+} primary ions were nearly perfect cuboid (Figure 20A) and so determining the volume was only a matter of measuring the length, width, and depth. The craters formed by Ar_n^{+} and $(H_2O)_n^{+}$ cluster ion beams, however, are hardly cuboidal (Figure 20B) and simply measuring the length, width, and depth would give a volume that was too large. A consistent protocol needed to be developed that would accurately describe the volumes, and to ensure that all the volumes were calculated by the same method.

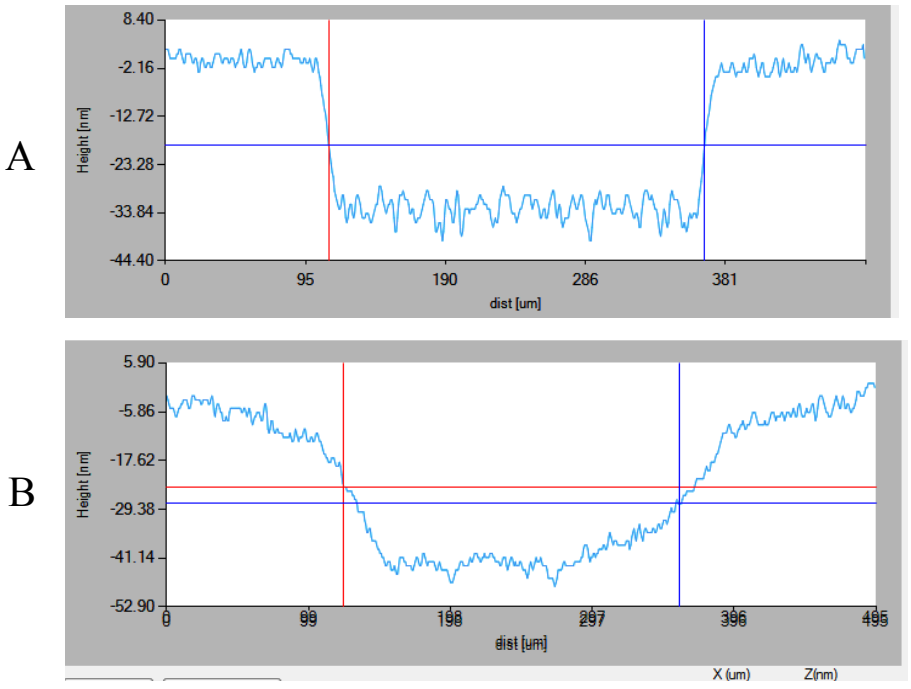

Figure 20: Computer-calculated cross section of craters. (A) Craters formed from C_{60}^{+} primary ions sputtering gave a nearly perfect cube shape. (B) Craters formed from Ar_n^{+} and $(H_2O)_n^{+}$ primary ions sputtering gave sides that were sloped and angled making the determination of the volume difficult.

The solution was to measure the length and width not to the edge of each crater, but to measure the length and width at half the slope of the sides. While the

sides were sloped, they were for the most part uniformly sloped. The assumption of this method was that the extra volume included at the bottom of the crater (Figure 21, red arrow) would be nearly equal to the volume not counted at the top of the crater (Figure 21, blue arrow). This would give an estimation of the volume that neither was too generous nor too small (Figure 21).

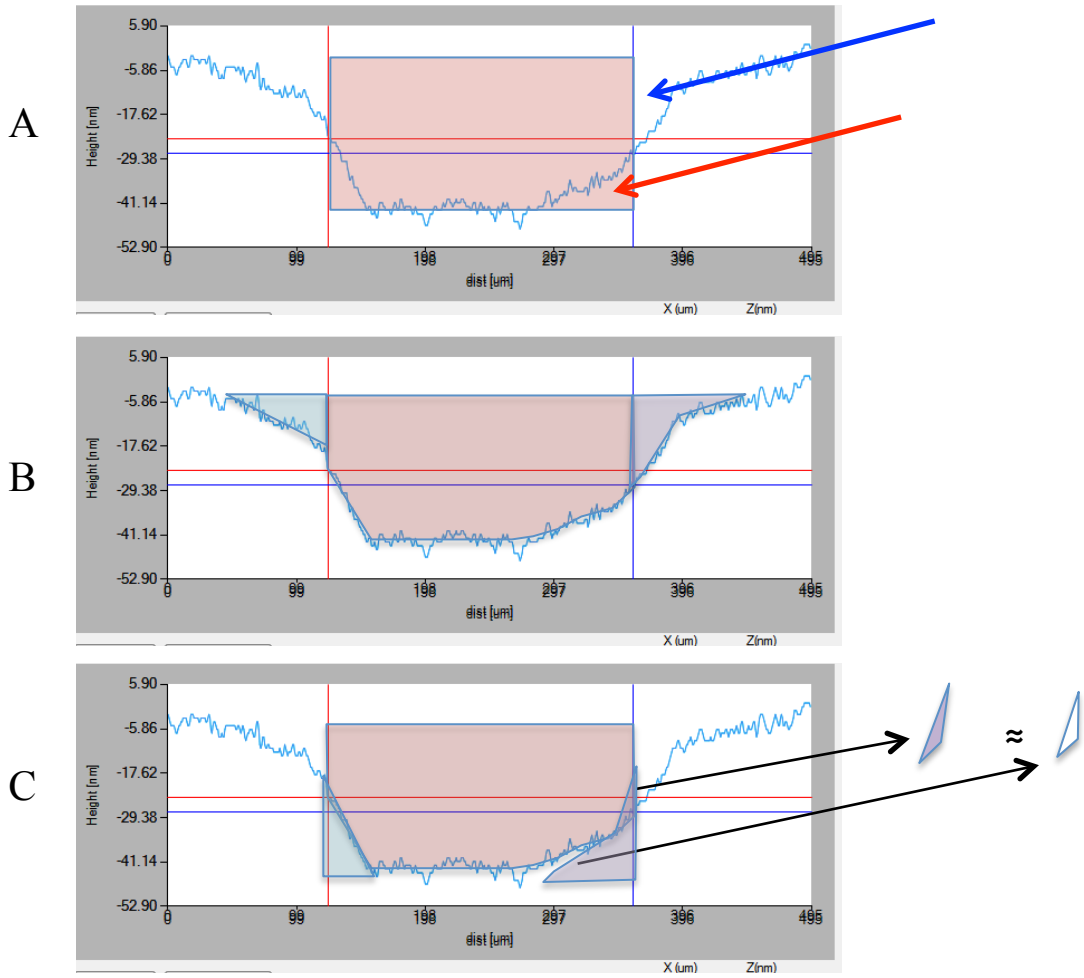

Figure 21: Demonstration of half-the-slope-volume calculations. (A) The typical sloping slides are seen in the cross section of this crater made through $(H_2O)_n^+$ primary ions sputtering. The red box at the center of the crater is the area of this computer-generated cross section where the width stretches from half one slope to half the other slope. (B) Using computer drawn shapes, the actual volume of the cross section is drawn here to demonstrate that the half-the-slope-volume calculation is a valid estimator of the actual volume. (C) The drawn green and purple shapes are moved to form approximately the same red box that is seen in panel A. The black arrows show that the white and purple triangles are drawn out to the side showing that the area overlapping and the area without coverage are approximately the same. Red arrow indicates the extra area that is included at the bottom of the crater but has not actually been removed in the sputtering experiments. The blue arrow indicates the area that sputtering has removed, but is not included in the half-the-slope-volume calculations.

While these estimations are very close to the actual volume, it must be stressed that these are estimations. Definite volumes would be preferred, but this was not possible with the instrumentation that was available. Others in the group tried to use atomic force microscopy (AFM) to estimate the volume of the craters, but the AFM was only able to determine the volume of a small part of the crater and thus was unhelpful. The goal of these experiments was not, however, to determine the definite volume of the craters, but rather to compare the sputter yields of different primary ions. As long as we used the same protocol to estimate volume on all of the craters, this method would allow for an accurate comparison.

To determine the length and width of the crater, the red and blue vertical lines seen in Figure 22 had to be moved to half way down the slope of the side. Medusa would then calculate the width of the cross-sectional view (Figure 22 green circle). The same would be done to determine the length. These lengths and widths would be transferred to the hologram and marked (Figure 23, next page - blue box 1 & 2) so that the depth would only be measured in desired area.

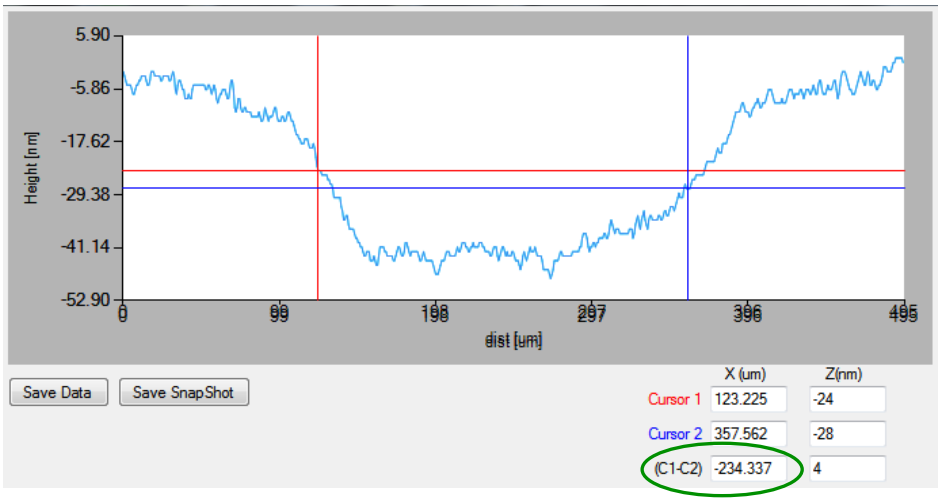

Figure 22: Medusa cross-sectional view and measuring the width of the crater from half slope to half slope.

The Medusa software then determines the height or depth of the film where the user drew the blue squares in the hologram window seen in Figure 23. While ideally the surface of the film would be uniformly zero, this rarely occurred (Figure 23, red circles). Even with the Irganox samples from NPL, the surfaces still had slight variations. To solve this, the computer-calculated average height of the surface was determined and subtracted from the computer-calculated average depth of the crater (Figure 23, green circle) to produce the actual depth of the crater (Equation 3, next page).

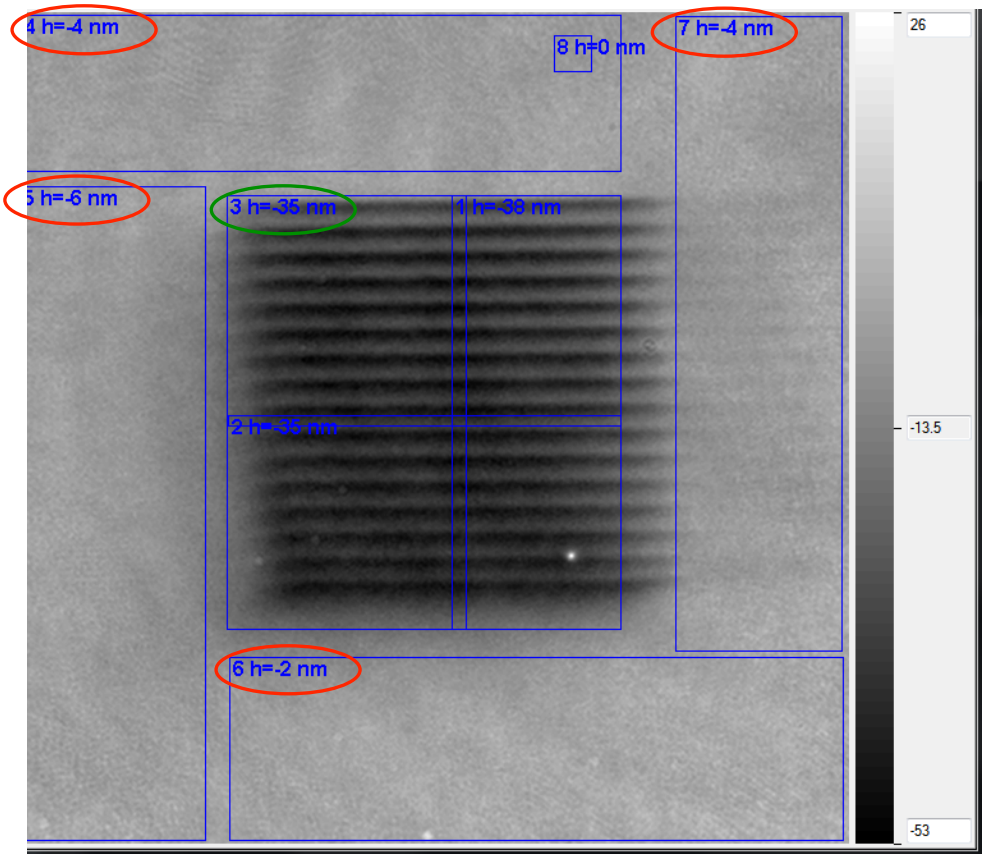

Figure 23: Hologram window of the Medusa software. The user draws the blue boxes and the computer program gives the average height or depth of those areas. Since the surface of the film is not uniformly flat (but -4 nm, -4 nm, -6 nm, and -2 nm), the surface had to be averaged (-4 nm) and then subtracted from the calculated depth (-35 nm) to give the actual depth (-31 nm). It should also be noted that box 3, which is the estimated depth, seems off center, but this is from half the slope to half the slope. Boxes 1 and 2 are drawn based off of cross-sectional views and then box 3 is drawn to be that exact length and width of those two boxes. Box 8 is not actually 0 nm, but is a programing error where the last box drawn is always 0 nm.

$$\text{Average Crater Depth} = -35 \text{ nm}$$

$$\text{Average Surface Height} = (-4 + -4 + -6 + -2)/4 = -4 \text{ nm}$$

$$\text{Actual Crater Depth} = (-35 \text{ nm} - -4 \text{ nm}) = -31 \text{ nm}$$

Equation 3: Calculating the actual depth of the crater by subtracting the average surface height from the average crater depth.

Finally, the measured width, height, and calculated depth would be multiplied to give the total estimated volume of crater (Equation 4).

$$(Width)(Length)(Depth) = Volume$$

$$Width = 234 \text{ nm}$$
$$Length = 257 \text{ nm}$$
$$Depth = -31 \text{ nm}$$
$$Estimated\ Volume = 1.86E6 \text{ nm}^3$$

Equation 4: Calculation of the estimated volume of the crater.

6.3 Sputter Yield Results

The calculated volumes were divided by the total ion counts to determine sputter yields. To confirm the effectiveness of our procedure, we compared our results with the previously found results for 10 keV C_{60}^+, 20 keV C_{60}^+, and 40 keV C_{60}^+ sputtering on Irganox 1010 (Table 6 & Figure 24):

Kinetic Energies in keV	Results in nm^3/ion		
C_{60}^+ Energy	2007 NPL Study[92]	2010 VAMAS Study[93]	Our Study
10	82 ± 8	~80 ± 10	62.0 ± 18
20	163 ± 16	~ 160 ± 20	152.6 ± 41
30	254 ± 25	~ 225 ± 10	Not Studied
40	Not Studied	~ 350 ± 200	397.2 ± 106

Table 6: Comparison our studies with previous studies for 10 keV C_{60}^+, 20keV C_{60}^+, and 40 keV C_{60}^+ sputtering on Irganox 1010 films.

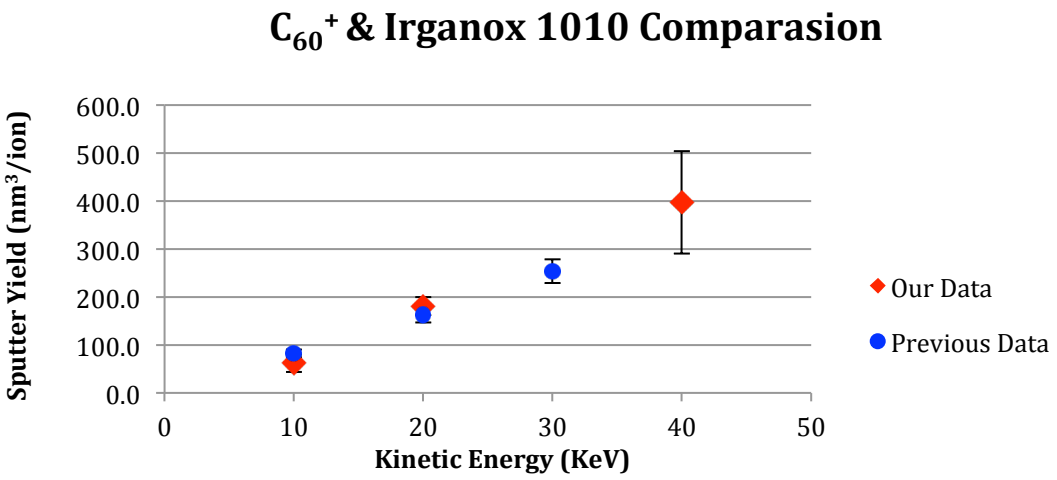

Figure 24: Graphical representation comparing 2007 NPL Study[92] with our data, showing that the two follow a similar trend.

Our results correlate very closely with previous data, demonstrating that our method of measuring crater volume is a viable protocol. The following pages are graphical representation of our results (Figure 25-Figure 29):

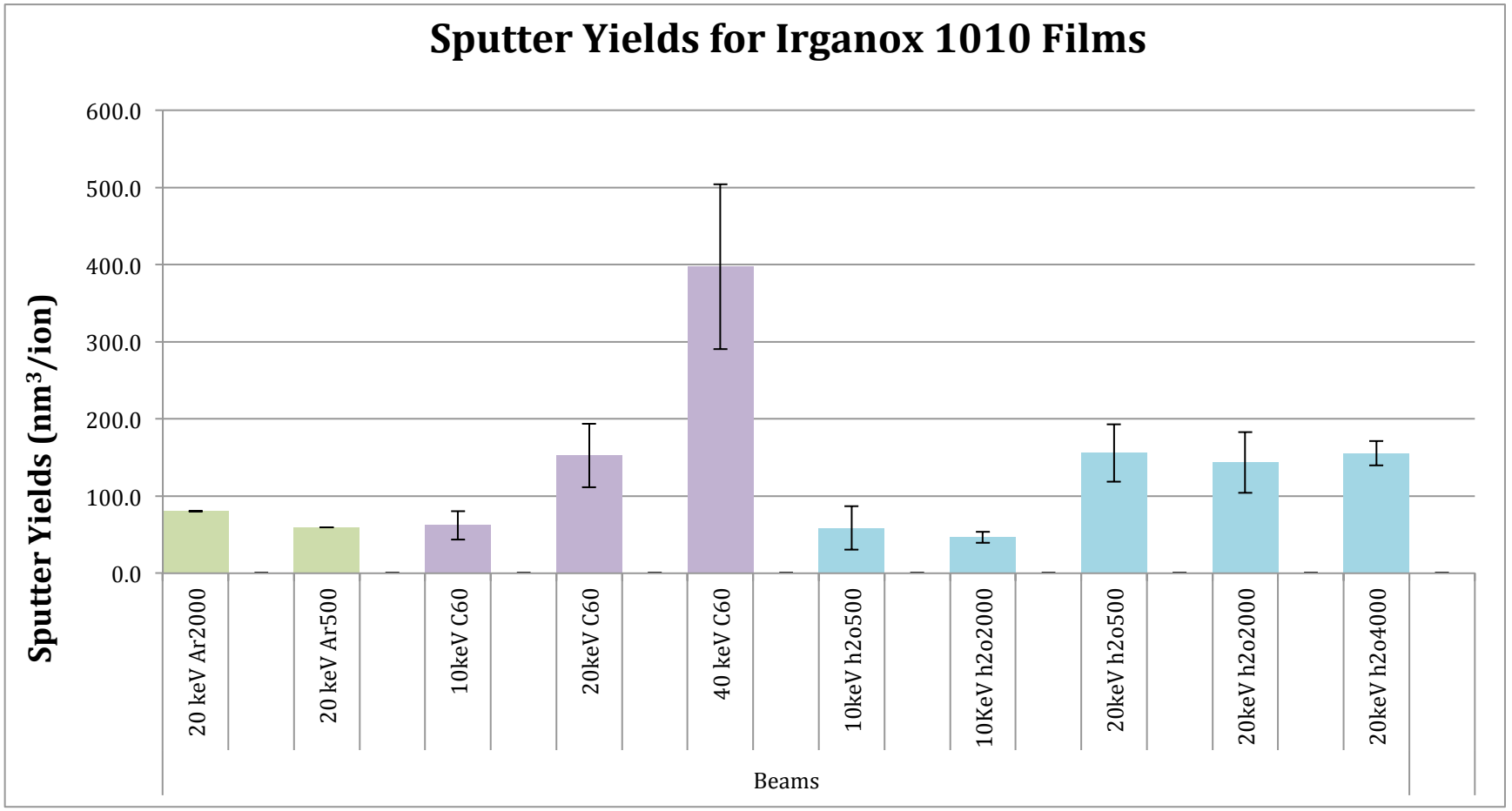

Figure 25: Sputter yields for Irganox films. Irganox 1010 was the most extensively tested film. The data demonstrates that sputter yields increase as the kinetic energy of the beams increase. When kinetic energies are constant, C_{60}^+ primary ions sputter similarly to $(H_2O)_n^+$ cluster ions, but both sputter greater than 20 keV Ar_n^+ cluster ions. C_{60}^+ primary ion and $(H_2O)_n^+$ cluster ion experiments were repeated in at least triplicate. Ar_n^+ cluster ions experiments were only performed once.

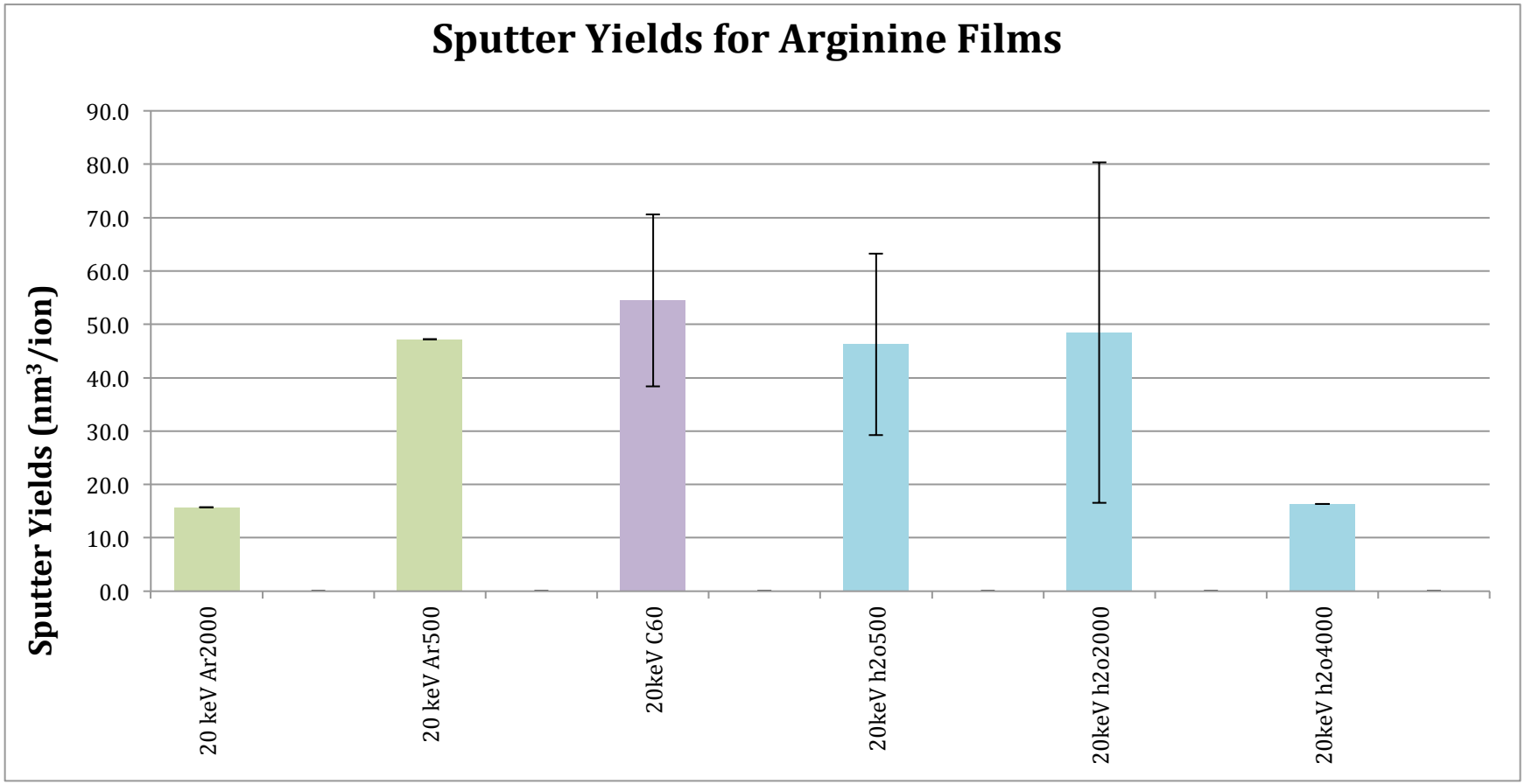

Figure 26: Sputter yields for arginine films. Arginine results show a greater variability within cluster ion types than appeared in Irganox 1010 studies. While 20 keV $(H_2O)_{500}^+$ and 20 keV $(H_2O)_{2000}^+$ sputter similarly, there is a large drop in $(H_2O)_{4000}^+$ cluster ion sputter yields. Similarly, 20 keV Ar_{500}^+ cluster ion has a greater sputter yield than 20 keV Ar_{2000}^+, indicating that the larger polyatomic primary ions sputter less than smaller polyatomic ions. 20 keV C_{60}^+ primary ions had the greatest sputter yields. 20 keV C_{60}^+, 20 keV $(H_2O)_{500}^+$, and 20 keV $(H_2O)_{2000}^+$ cluster ions were tested in at least duplicate, while 20 keV Ar_{500}^+, 20 keV Ar_{2000}^+, and $(H_2O)_{4000}^+$ cluster ions were tested once.

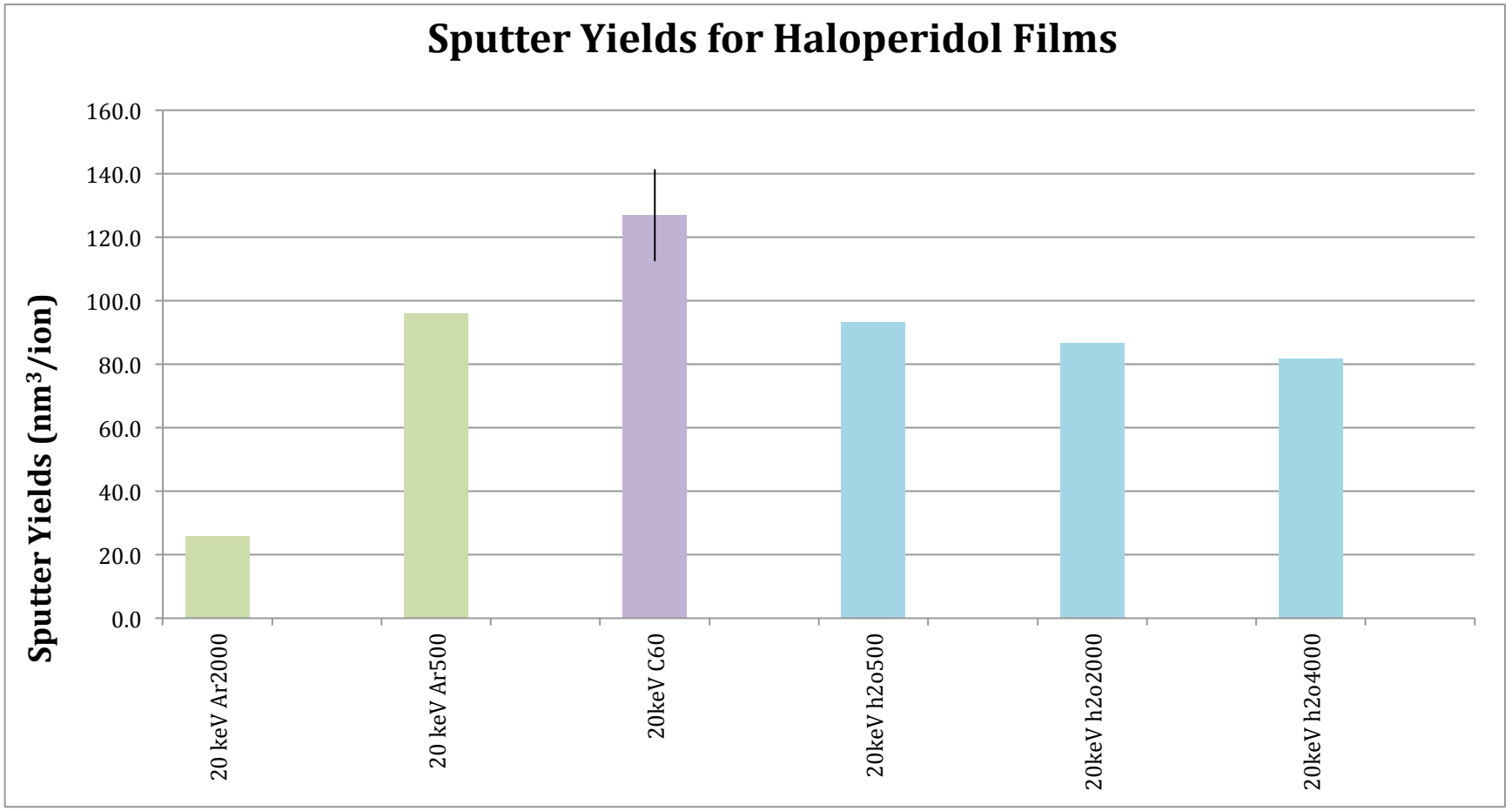

Figure 27: Sputter yield results for haloperidol films. All haloperidol sputter yield experiments were run once except for 20 keV C_{60}^+ primary ion experiments, which were run in duplicate. Similar to the sputtering of Arginine, 20 keV C_{60}^+ primary ions had the greatest sputtering effects and 20 keV Ar_{500}^+ cluster ions have a greater sputter yield than 20 keV Ar_{2000}^+ cluster ions. Variation within $(H_2O)_n^+$ cluster ions is not seen as $(H_2O)_{4000}^+$, $(H_2O)_{2000}^+$, and $(H_2O)_{500}^+$ primary ions all sputter between 80 and 90 nm^3/ion.

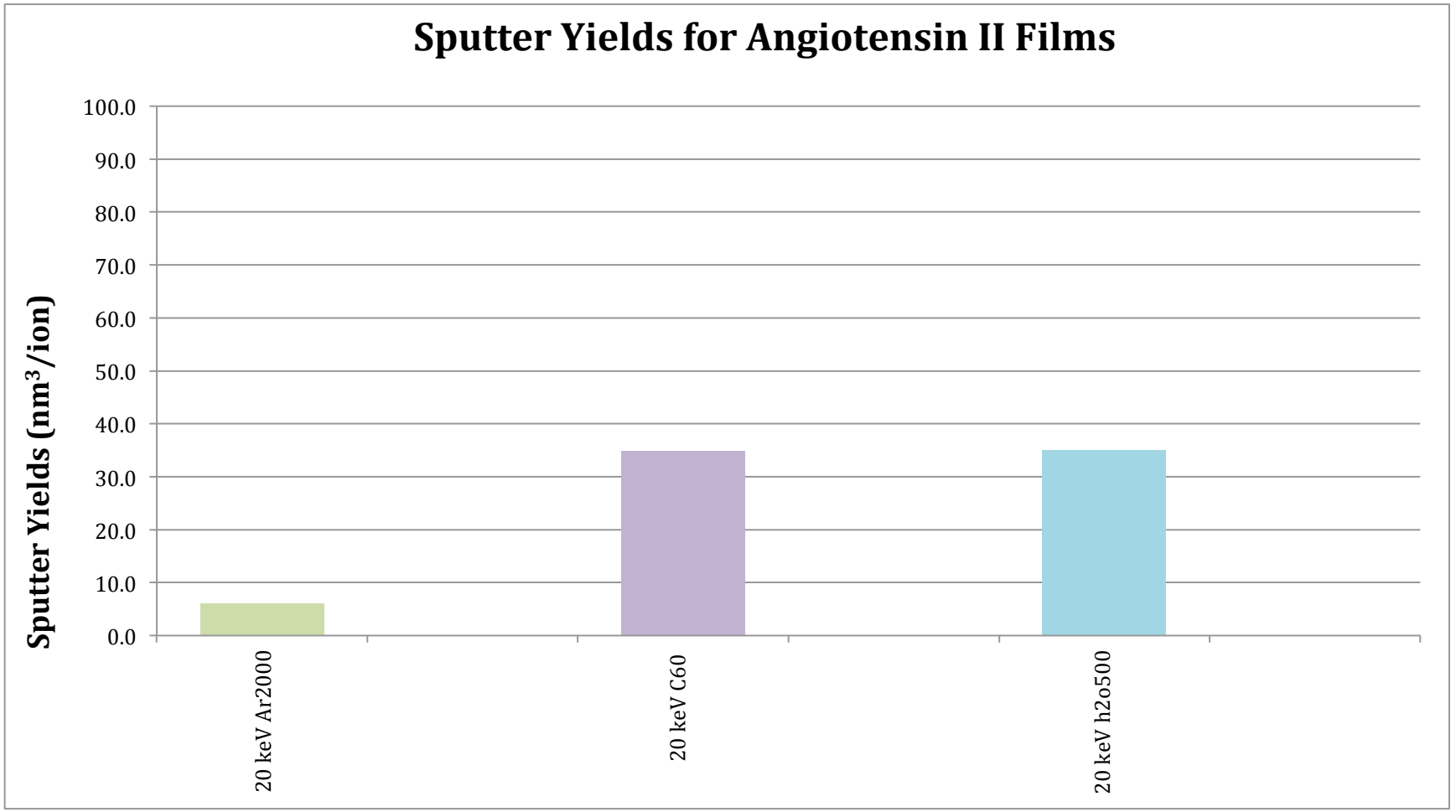

Figure 28: Sputter yield results for angiotensin II. All angiotensin II experiments were run once. Overall sputter yields are much less than Irganox 1010, arginine, or haloperidol. 20 keV Ar_{2000}^{+} primary ions sputter much less than 20 keV C_{60}^{+} or 20 keV $(H_2O)_{500}^{+}$ cluster ions. 20 keV C_{60}^{+} or 20 keV $(H_2O)_{500}^{+}$ cluster ions had similar sputter yields.

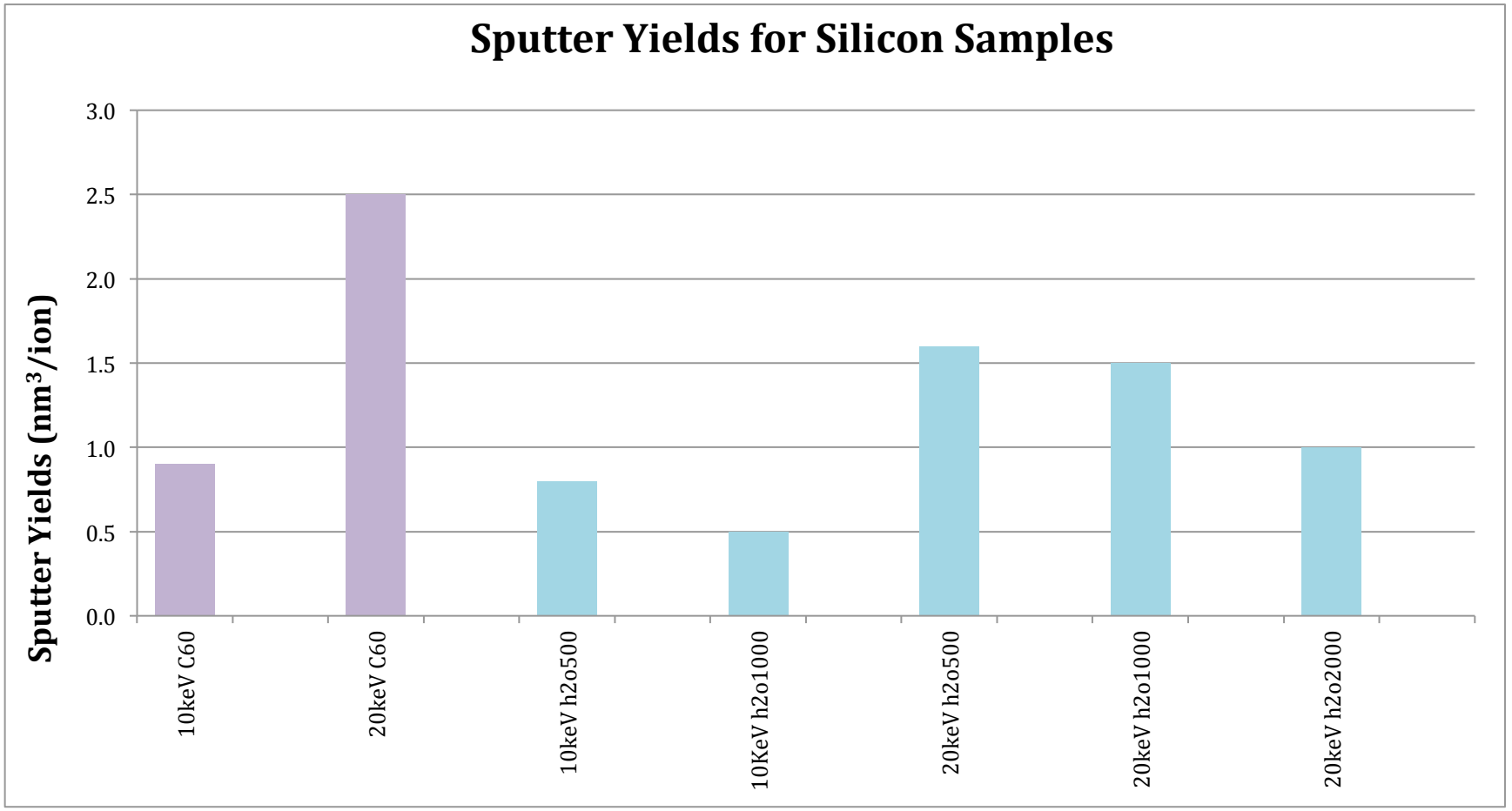

Figure 29: Sputter yield results from silicon sputtering. All silicon sputtering experiments were performed once. Ar_n^+ cluster ions were not tested since previous experiments performed in the lab showed no visible sputtering. Once again, sputter yields are greater when the kinetic energy is greater. 20 keV C_{60}^+ primary ions also once again had the greatest sputter yields.

6.4 Sputter Yield Discussion

6.4.1 Comparing $(H_2O)_n^+$ and Ar_n^+ sputter yields for Irganox 1010.

Ar_n^+ and $(H_2O)_n^+$ are both two newly discovered gaseous primary ions but the above data suggests that the sputter yields produced by these ions are different. While sputter yields are comparable for haloperidol and arginine films, there is a large difference when Irganox 1010 and angiotensin II are sputtered. Further evidence of the two beams' differences can be seen in (Figure 1, page 32), where water primary ions create as much as 50 times more secondary ions compared to argon yields.

One way of comparing the two beams is by looking at each beam's universal sputtering yield plot. Previous research has shown that there is a universal equation for sputter yields per primary ion (Figure 30), forming a linear regression when sputter yield per numbers of atoms in the primary cluster (Y/n) is plotted against energy per number of atoms (E/An) on a log-log plot.

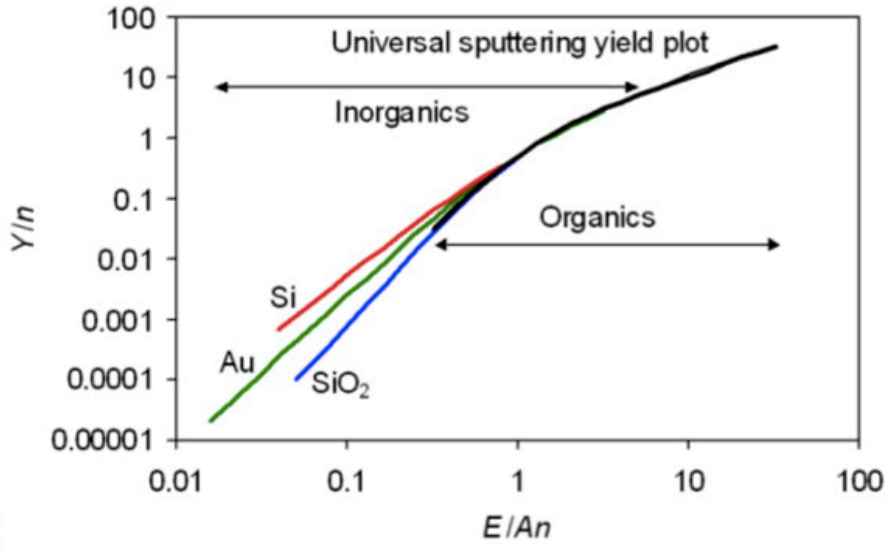

Figure 30: Log-log plot demonstrating the universal sputtering yield plot where Y/n is the sputter yield per numbers of atoms in the primary cluster and E/An is energy per number of atoms.[103]

The Seah 2013 paper describing the universal sputter yield of argon provides an excellent set of data for comparison. In Figure 31A (next page), Seah creates a sputtering yield plot for argon sputtering on Irganox 1010. When we compare our own water sputtering data on Irganox 1010 (Figure 31B), a similar line appears. When we graph own argon and water sputtering data, we find that the water cluster beam appears to have a higher sputter rate per nucleon than argon (Figure 31C).[103]

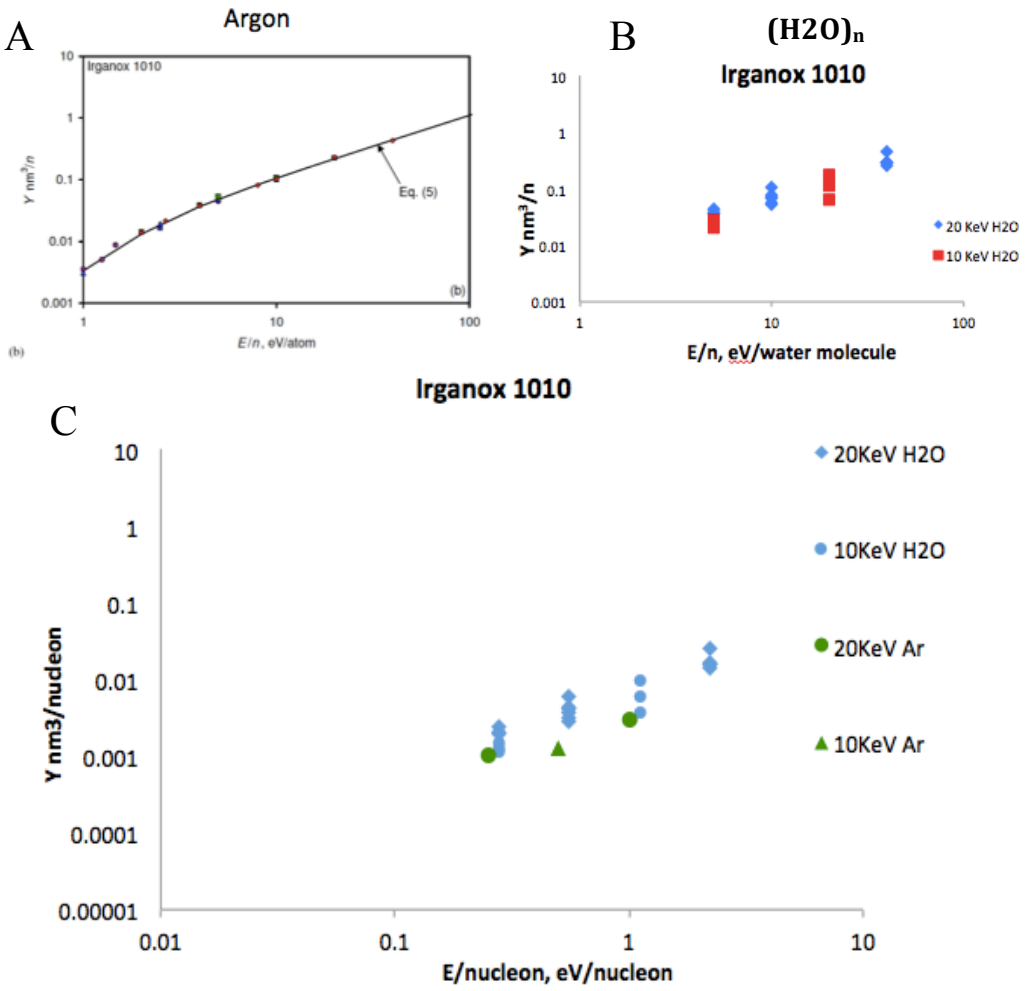

Figure 31: Universal sputter yield plots for argon and water cluster ion beams. (A) Seah 2013 data plotting argon sputtering on Irganox 1010 with linear regression fitting.[103] (B) Our data plotting water primary ions sputtering on Irganox 1010 for 10 keV $(H_2O)_{500}^+$, 10 keV $(H_2O)_{2000}^+$, 20 keV $(H_2O)_{500}^+$, 20 keV $(H_2O)_{2000}^+$, and 20 keV $(H_2O)_{4000}^+$. In order to compare Seah's argon results (A) with our water results (B), the units must be slightly different. Seah's data measures energy per number of atoms in the cluster, i.e. Ar_{4000}^+ would have 2000 atoms in each cluster and so the energy of each cluster would be divided by 2000. In order to accurately compare our data for water, which consists of both hydrogen and oxygen atoms, I chose to graph Energy per water molecule in each cluster, i.e. $(H_2O)_{4000}^+$ will have 4000 water molecules and so the energy of each cluster will be divided by 4000. This insures that our comparison is per *ion unit*. This comparison is not to determine a universal equation for the water cluster ion beam, but rather to demonstrate that our water data also appears to follow a similar universal sputter yield trend. While (A) and (B) are graphed per *ion unit*, they cannot be graphed on the same axes, thus for (C), our water sputtering data and our argon sputtering data are graphed using the unit Energy per *nucleon* (i.e. the combination of neutrons and protons within the atom or molecule – argon has 40 nucleons and water has 18 nucleons). (C) shows that the water cluster ion beam has a greater energy per nucleon than argon.

6.4.2 Comparing primary ion sputter yields of Arginine.

We can also use log-log plots to analyse C_{60}^+ and water cluster ion beams. The raw data (Figure 26) suggest that the sputter yield from the water cluster ion beam is equal to or less than the sputter yields of the C_{60}^+ primary ion beam at similar kinetic energies. In arginine film experiments specifically, the C_{60}^+ and water cluster ion beams behave similarly with the exception of 20 keV $(H_2O)_{4000}^+$ cluster ions, which sputtered three times less than the 20 keV C_{60}^+ primary ions. When all the experiments using arginine film are plotted on the log-log plots (Figure 32, next page), the C_{60}^+ primary ions sputtering appear on the top right, $(H_2O)_{500}^+$ cluster ions sputtering are in the middle, and $(H_2O)_{4000}^+$ cluster ions sputtering can be seen in the bottle left. These positions correlate to the "removal power" of each nucleon within the cluster ion. A nucleon is the heavy particles that make up the atom's nucleus, which includes protons and neutrons – this provides a better comparison than trying to compare a carbon atom and a water molecule. Table 7 calculates the sputtering per nucleon for the three experiments in Figure 32.

Experiment	Energy/nucleon	nm^3/ion	nm^3/nucleon
20 keV C_{60}^+	27.78	43.1	0.0599
20 keV $(H_2O)_{500}^+$	2.22	35.7	0.0040
20 keV $(H_2O)_{4000}^+$	0.28	16.3	0.0002

Table 7: Calculating the nm^3/ion nucleon for 20 keV C_{60}^+, 20 keV $(H_2O)_{500}^+$, and 20 keV $(H_2O)_{4000}^+$.

While each nucleon of a 20 keV C_{60}^+ primary ion beam removes 0.0599 nm^3, each nucleon of a 20 keV $(H_2O)_{4000}^+$ cluster ion beam removes 300 times less. This means that in a tissue experiment, the water cluster ion beam would provide more control over the amount of sputtering and the C_{60}^+ primary ion beams provide increased sputtering.

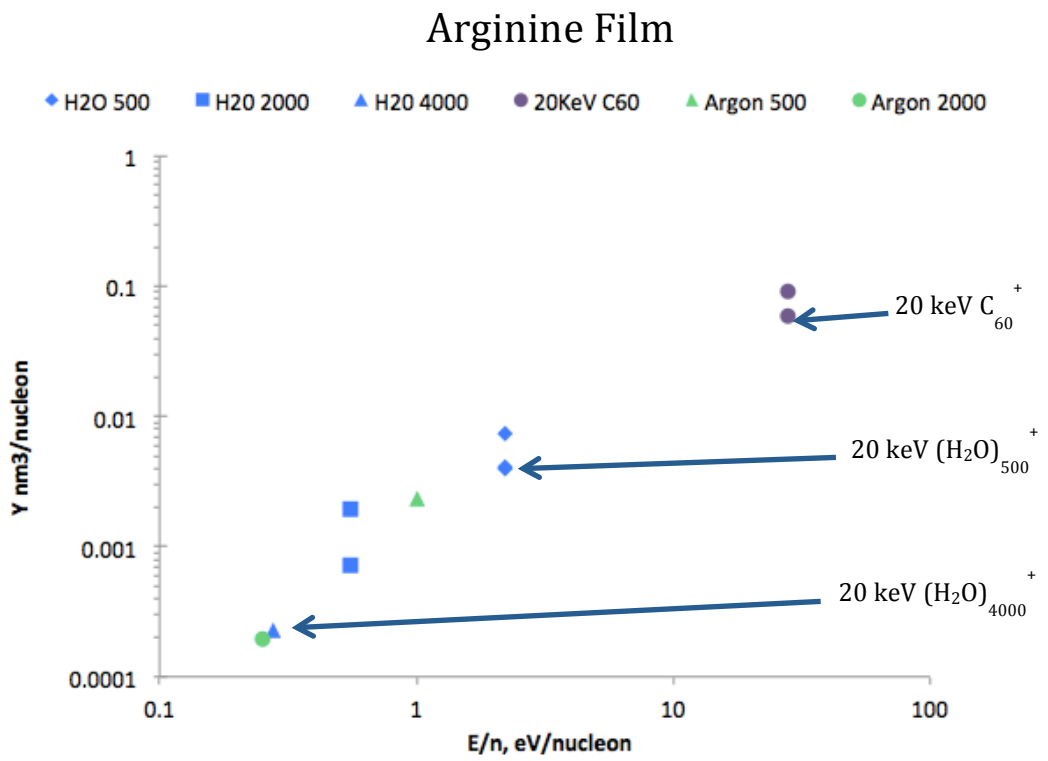

Figure 32: Log-log plot of the C_{60}^+, Ar_n^+, and $(H_2O)_n^+$ cluster ions on an arginine film. Three experiments are pointed to and the sputter yields of these three experiments are discussed above in Table 7.

When this data is compared with the previous data for *secondary ion production* on arginine films (Figure 10), it becomes clear that this increase in secondary ions seen with $(H_2O)_n^+$ cluster ions compared to C_{60}^+ primary ions is not due to an increased sputter yield, as $(H_2O)_n^+$ cluster ions sputter less than the C_{60}^+ primary ions experiments. Instead, this suggests that $(H_2O)_n^+$ cluster ions induce an increased yield of secondary ions through an unknown mechanism.

More recent secondary ion yields were measured again for arginine; this time, using beam energies of 20 keV (Figure 33A, next page). Two secondary ions for arginine were measured: 349 m/z: $[2M+H]^+$, an arginine dimer ion, and 523 m/z: $[3M+H]^+$, an arginine trimer ion. These results demonstrate a similar increase in secondary ion yields created by the water cluster ion beam. $(H_2O)_{500}^+$ and

$(H_2O)_{2000}^+$ cluster ions have secondary ion yields 1.25 to 1.5 times greater than the secondary ion yields of C_{60}^+ ions, but the secondary ion yields of $(H_2O)_{4000}^+$ are 2.5 to 3.5 times greater. Since each sputtering experiment received a 5×10^{11} ion dose, we are able to predict the relative sputter yields for each experiment (Figure 33B). This graph shows that $(H_2O)_{4000}^+$ cluster ion sputtering is only expected to remove a quarter of the material that would be expected with C_{60}^+ primary ion sputtering; however, $(H_2O)_{4000}^+$ cluster ion sputtering creates 10 to 14 times more secondary ions than would be predicted, suggesting that the $(H_2O)_n^+$ cluster ions form secondary ions through a new method.

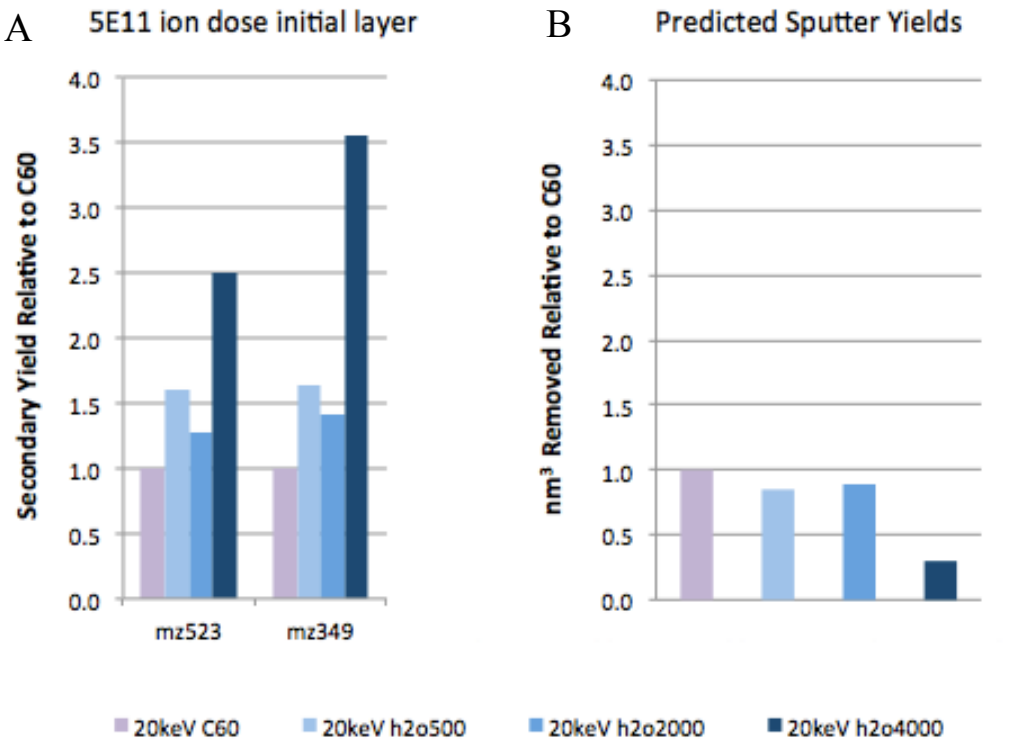

Figure 33: Comparison of secondary ion yields with predicted sputter yields for 20 keV C_{60}^+, 20 keV $(H_2O)_{500}^+$, 20 keV $(H_2O)_{2000}^+$, and 20 keV $(H_2O)_{4000}^+$. Each secondary yield experiment received 5E11 ion dose, and secondary ion yield is measured for the initial layer. Predicted sputter yields were calculated by multiplying the applied ion dose by the sputtering rates calculated above in Figure 26. The graphs illustrate that secondary ion yield rates of 20 keV $(H_2O)_{4000}^+$ are 10 to 14 times greater than the secondary ion yield rates of 20 keV C_{60}^+. Secondary ion yields were measured by Dr. Sadia Sheraz.

These early studies provide a general sense that the increased secondary ion yields seen in the water cluster ion beam are not due to the typically held mechanisms of sputtering. Water, while mostly H_2O, also contains varying concentrations of ^-OH, and H_3O^+. It might be that these charged water species induce increased *ionisation* by transferring or receiving free electrons and or protons. Experiments will continue in the Vickerman laboratory to better describe these increased secondary ion yields as well as to seek an explanation for this increased rate of secondary ion production.

In choosing a cluster ion beam for tissue samples, three other factors needed to be considered beyond secondary ion yields. The first was reproducibility. While the water cluster ion beam gives more, and a larger range of, secondary ions, the beam is still a prototype and was under development for a large part of my time. The second issue to consider was tissue charging. The Ar_n^+ cluster beam was unable to sputter cholesterol-rich portions of the brain without charging, thus leaving large portions of images without signal. Finally, spot size needed be taken into consideration. Both the water cluster ion beam and the argon cluster beam struggled to obtain spot sizes smaller than 10-15 μm, while the C_{60}^+ cluster ions could achieve a spot size of better than 3.5 μm. Thus, for the tissue experiments in the next chapter, I chose to use the C_{60}^+ cluster ion beam because it provided the best spot size, the best reliability, and did not exhibit excessive charging.

7. Mouse Brain Tissue Analysis

7.1 Tissue Staining and SIMS Analysis Introduction

7.1.1 Project Aims

After our study to determine the sputtering rates of the various ion cluster beams, the project transitioned to tissue sample analysis. Brain tissue samples were collected from triple transgenic mice designed to develop Alzheimer's disease – the 3xTg-AD mouse model. While ToF-SIMS provides a picture of the lipid distribution in these diseased tissues, the amyloid plaques cannot be seen since they can be hundreds of thousands of kilodaltons and thus are outside the range of detection. Further, if these proteins were analysed to determine a characteristic fragment, there would be no way to determine if this characteristic fragment came from a monomer or a vast neurotangle. Thus as part of my project, I set out to determine a way of detecting the oligomers and large plaques using ToF-SIMS so that these characteristic markers of Alzheimer's disease could be correlated to the lipid and metabolite localisation that is readily seen in ToF-SIMS analysis.

In a previous lab, I had used Thioflavin T to determine neurodegenerative protein aggregation rates and thus knew that this molecule binds to oligomers and larger aggregates and falls within the detection range of ToF-SIMS. Thioflavin T is typically used to stain tissue and many protocols exist for its use, thus the application to tissue was very easy. Finally, Thioflavin T exists as a salt with a monoisotopic mass of 318.0957, composed of a Thioflavin T positive ion in conjunction with chloride, making detection of Thioflavin T with positive ion SIMS ideal.

Early trials with Thioflavin T in ToF-SIMS found the secondary ions yields to be excellent but the secondary ions overwhelmed the tissue images, thus the right stain concentration had to be found. The ideal Thioflavin T staining concentration and protocol were devised. Tissue samples were analysed, then stained, and then analysed again, which allowed the correlation of areas of aggregation with the unaltered pre-stain images.

In the last part of this chapter, I will briefly discuss the localisation of lipids surrounding the amyloid plaques in a few of the samples that were analysed. While the study correlating amyloid plaques with localised chemistry are only preliminary, the method for detecting amyloid plaques has been established and will be used in this laboratory in the future.

7.1.2 Previous Research

While the usage of SIMS for tissue analysis is widely utilised, the use of tissue stains and SIMS has been limited. This dissertation might describe the first instance of analysing a stain with ToF-SIMS in order to gain additional information from the tissue. While there is no documentation concerned with the use of ToF-SIMS to analyse a histological stain, there have been several previous papers where tissue stains and ToF-SIMS images have been compared or overlaid. The first of these is an article by Alain Brunelle in which he examines whether optical images from the stained samples could be overlaid with images produced from ToF-SIMS analysis.[104] Brunelle stained healthy rat brains with Hematoxylin and eosin in an effort to correlate stained cholesterol deposits with the cholesterol secondary ions seen using ToF-SIMS. The study, however, found that the two images could not be

easily overlaid due to distension in the tissue. The distension occurred as tissue samples were imaged under high vacuum for ToF-SIMS, but under atmospheric pressure for microscopic images. This variation in pressure, along with the dehydration of the tissue that is experienced when the tissue is under a microscopic light for an extended period of time, causes the tissue's structure to be variable. While the use of a fixation agent is designed to prevent this distension, Brunelle shows that fixation agents caused a loss of signal in ToF-SIMS acquisitions. While their goal to overlay ToF-SIMS acquisitions and histological stains was not achieved, their work provided a framework for the experiments described in this dissertation.

The Johansson group at the Karolinska Institutet in Stockholm, Sweden also published a paper that used both ToF-SIMS and stains. This paper described the co-localisation of cholesterol and amyloid-beta plaques in 18-24 month old triple transgenic Alzheimer's disease (3xTg-AD) mouse models.[105] The cholesterol was imaged with a ToF-SIMS ION-TOF and the amyloid plaques were stained via p-FTAA, an amyloidotropic fluorescent dye developed by the Johansson group. These studies overlaid the ToF-SIMS and histological stains, demonstrating the co-localisation of the stains and surrounding cholesterol. Their figure (next page) depicting the ToF-SIMS cholesterol deposits (Figure 34A) and then with the added overlay of the p-FTAA stain (Figure 34B) provides a convincing case for the co-localisation of cholesterol and amyloid plaques in triple transgenic AD mouse models.

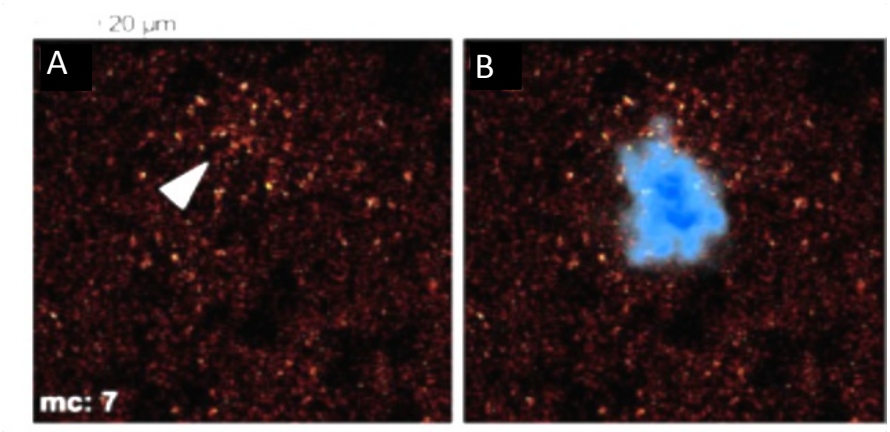

Figure 34: Johansson Group Image from published article demonstrating the co-localisation of ToF-SIMS-identified cholesterol, m/z 369 (white arrow, A) and p-FTAA stained amyloid-beta aggregates (blue spot, B).[105]

The Johansson paper does not comment on any problems with distention or problems overlaying these two images. This paper provided an excellent benchmark for the identification of amyloid plaques and an introduction to the chemistry surrounding these plaques.

7.1.3 Structure of the Mouse Brain

Amyloid plaques are most often found in either the isocortex or hippocampus regions of the brain (Figure 35). These regions are surrounded by white matter that is rich in lipids and cholesterol. While these regions can be initially difficult to

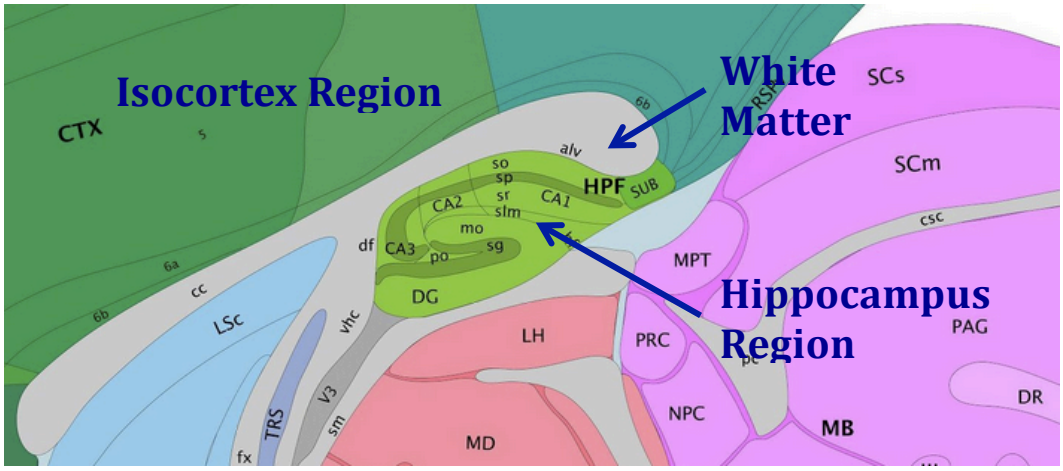

Figure 35: Anatomical image of a sagittal cut mouse brain.[106]

identify in SIMS and fluorescent microscopy images, identification is easier once the white matter has been identified. The white matter has the appearance of a golf club cradling the hippocampus and the isocortex is then found between the white matter and the edge of the brain (Figure 36, next page). Figure 36A is a fluorescent microscopy image where within the hippocampus the pyramidal neurons can be seen forming a backwards "s" shape.[107] It is within these neurons that hippocampus aggregation occurs.[108] Figure 36B is a ToF-SIMS image that shows a wider view so that a large portion of the isocortex can be seen.

Once the structure of the brain has been determined, the identification of plaque is the next step. Figure 37 (page 89) gives a demonstration of what a Thioflavin-stained aggregate looks like on a fluorescent microscopy image. These blotches of high fluorescent intensity are generally 20 μm to 70 μm in diameter

depending on the age of the mice. Further, rarely are they perfect circles but rather as a slowly added jumble resembling a nest, as can be seen in the electron microscope image of an amyloid-beta aggregate in Figure 38 (next page).[109]

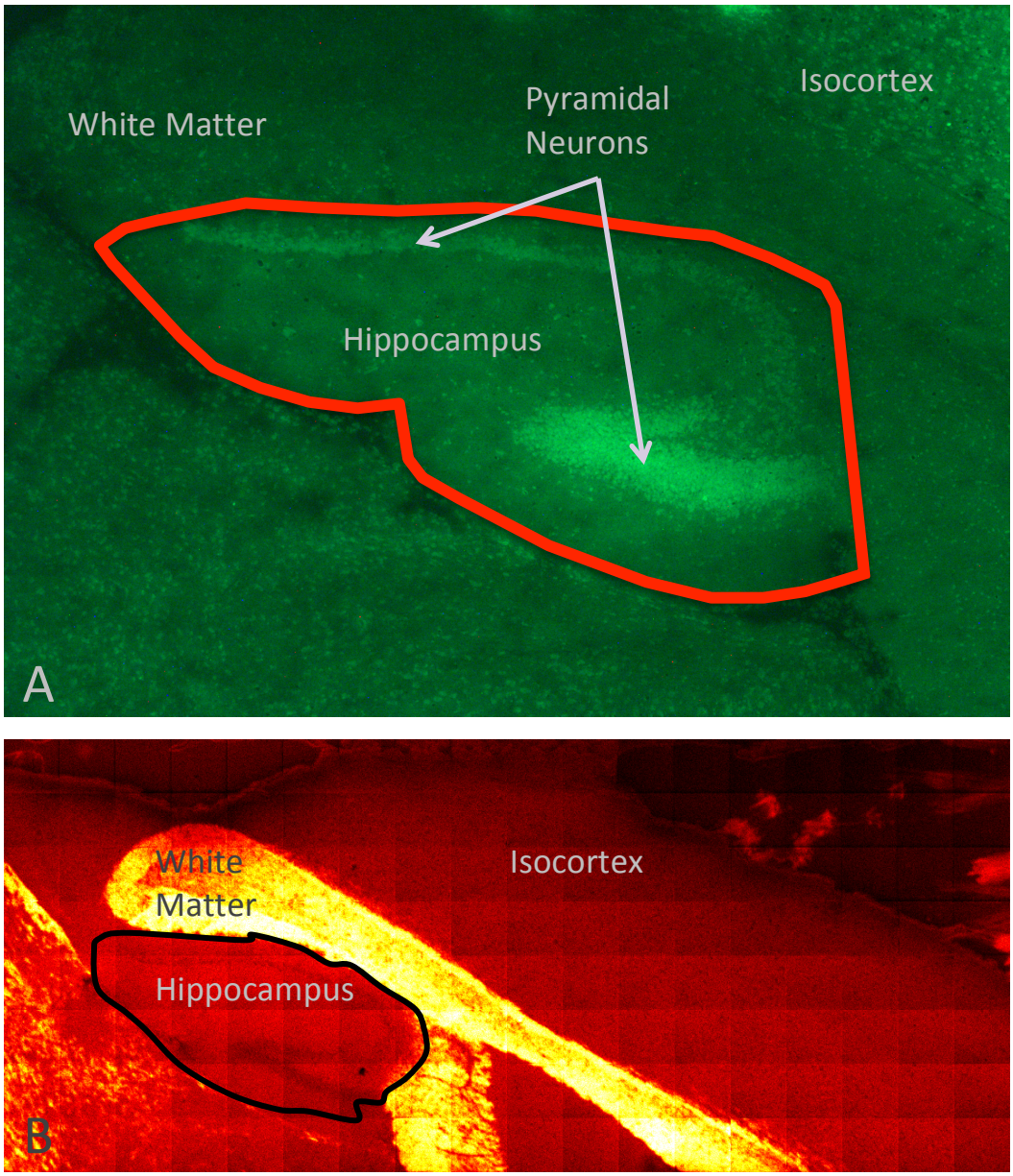

Figure 36: Anatomy of the brain identifying the isocortex and hippocampus for A) fluorescent microscopy and B) ToF-SIMS images.

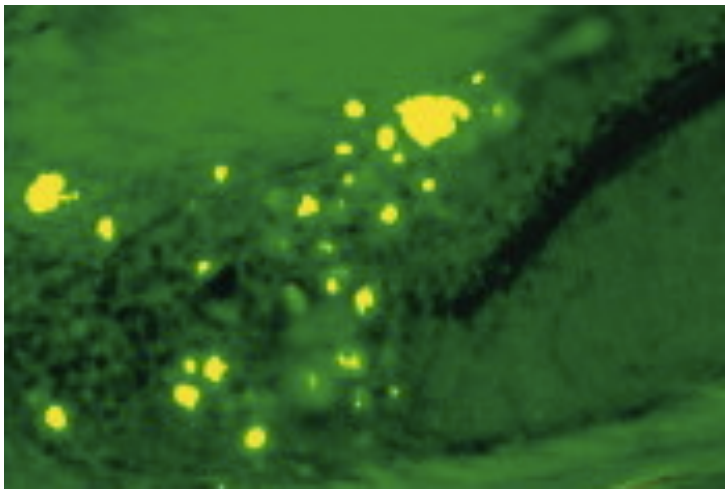

Figure 37: 3xTg-AD mouse model brain tissue stained with Thioflavin S depicting increased fluorescent due to amyloid-beta aggregates found in the pyramidal neurons of the hippocampus.[108]

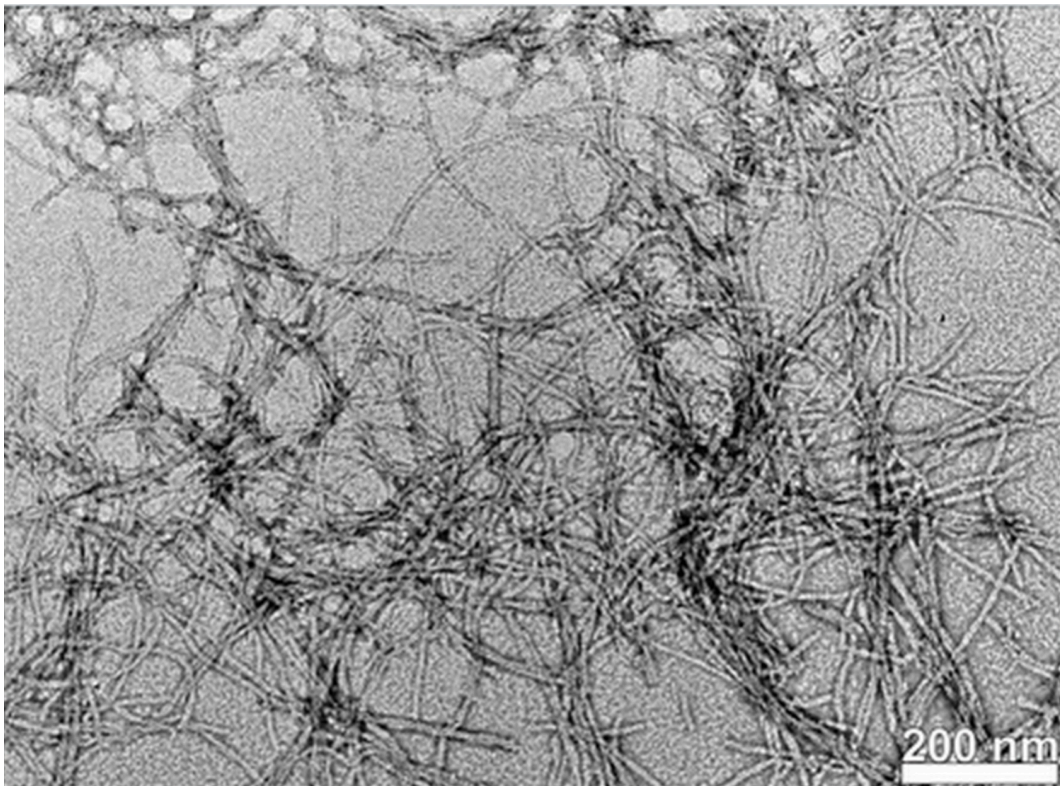

Figure 38: Electron microscope image of an amyloid-beta plaque demonstrating the stringy aggregates forming clumping together to form a mesh-like structure.[109]

7.2 Tissue Analysis Experimental Design

7.2.1 Collecting Mouse Brain Samples

The model mice and wild-type mice used in this experiment were raised and provided by Dr. Hervé Boutin. The triple transgenic mice, 3xTg-AD, have had three genes modified with four point mutations inserted: APP (KM670/671NL), MAPT (P301L), and PSEN1 (M146V). This widely used strain develops both extracellular plaques and tangles after 12 months.[108,110] The triple transgenic mice used in these experiments were sacrificed after 15 months. Wild-type mice were not raised with the 15-month 3xTg-AD mice, so instead 9-month wild-type mice were used, but these were raised under similar conditions and regimens. Mice were allowed ad libitum access to water and food and were raised under humidity, temperature, and light-controlled conditions. All animal procedures were performed under the University of Manchester project license number (40/3076) and adhered to the UK Animals (Scientific Procedures) Act (1986).[111]

Mice were deeply anesthetised with isoflurane and decapitated, and the brain was snap frozen in isopentane at -40°C. The brains were stored in the -80°C freezers for a few weeks until they were sectioned to 8 μm using a cryostat in a sagittal orientation and placed onto small silicon wafers. All sectioning took place at -20°C. The silicon wafers with adhered tissue were placed into test tubes, sealed with lids, and wrapped in parafilm to prevent water from seeping in and ruining the samples. Samples were placed into a cooler with dry ice, quickly transported back to the lab, and finally placed into an -80°C freezer until they were stained or analysed.

7.2.2 Staining Protocol Development

Before the analysis of the tissue could begin, the staining protocol first had to be developed. The process of staining the mouse brains for amyloid plaques had to overcome multiple obstacles. The first of these was to determine if a characteristic secondary ion for Thioflavin T could be detected using ToF-SIMS. To determine this, a film of pure Thioflavin T was made and then analysed. Thioflavin T (Sigma) was dissolved in 100% ethanol. This solution was then filtered through a 0.2 μm membrane filter (Whatmann) and 5 mL was then added to an unwashed silicon wafer. Instead of spin casting the film, the solution was allowed to sit for 20 minutes as the ethanol evaporated. Once dry, another 5 mL would be added and then allowed to sit for 20 minutes. This was repeated once more for a total of 15 mL of total volume added to the silicon wafer.

The newly formed film was then placed inside the J105 3D Chemical Imager. The Thioflavin T film was analysed in positive ion mode. Since Thioflavin T exists as a positive ion associated with a negative chloride ion, it was most likely that the detection of Thioflavin T would be in positive ion mode. The film was analysed with a 4.5 μm spot size and an ion dose of 2.18E12 ions/cm^2, producing the mass spectrum seen on the next page (Figure 39). While the Thioflavin T and chloride conjugate has a monoisotopic mass of 318.1 Daltons, the Thioflavin T ion has a monoisotopic mass of 283.1 Daltons. This mass of 283.1 m/z can be seen in the spectrum below as the largest ion fragment $[M\text{-}Cl]^+$, yet this was not the most prolific secondary ion detected. Instead a secondary ion with the molecular mass of 267.1 m/z was by far the most abundant species. This secondary ion is most likely created as a result of a loss of $–NH_2$ or $–CH_4$ group $[M\text{-}Cl\text{-}NH_2]^+$ or $[M\text{-}Cl\text{-}CH_4]^+$.

Thus, the presence of two secondary ions, 267.1 and 283.1 m/z, indicate the presence of Thioflavin T and thus the location of amyloid-beta aggregates.

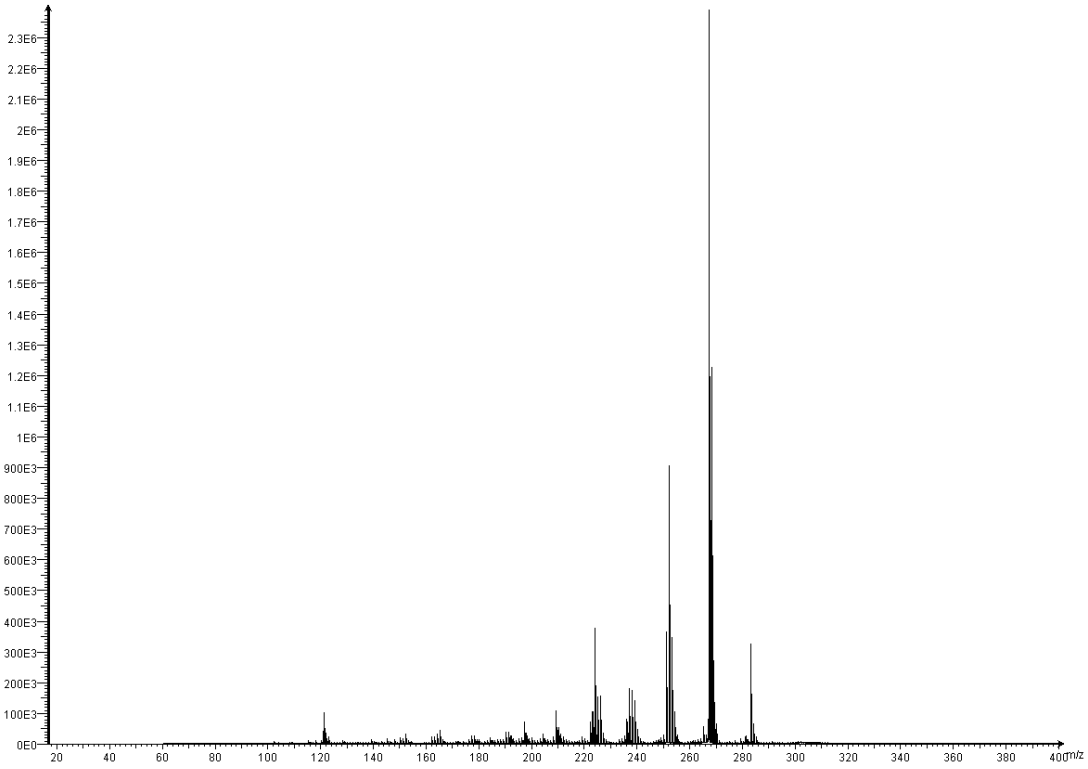

Figure 39: Mass Spectrum of Thioflavin T film. Experiment was conducted with the C_{60}^{+} primary ion beam, a 4.5 µm spot size, 11 pA, 500 shots, a tile 290 µm x 290 µm, 64 pixels/square, and a 12% Duty cycle for a total ion dose of 2.18E12.

After determining that the stain was detectable in ToF-SIMS, the next step was to determine the best staining protocol. The first consideration of the staining protocol was the concentration of the histological dye. While it was imperative to stain the amyloid plaques sufficiently, over staining would cause an excessively bright background. During an early experiment, a Thioflavin T stain concentration of 0.02% was used to stain a triple-transgenic Alzheimer's-diseased mouse brain. The tissue was imaged prior to and after staining. The total ion image for pre- and post-stains can be seen below in Figure 40. The post-stain image (Figure 40B) is oversaturated due to an overly concentrated Thioflavin T stain. Even though the

tissue is washed thoroughly, the small molecule is still in excess due to the high concentration of the stain. Thus, a less concentrated stain of 0.002% was developed which provided excellent differentiation, as seen in Figure 60.

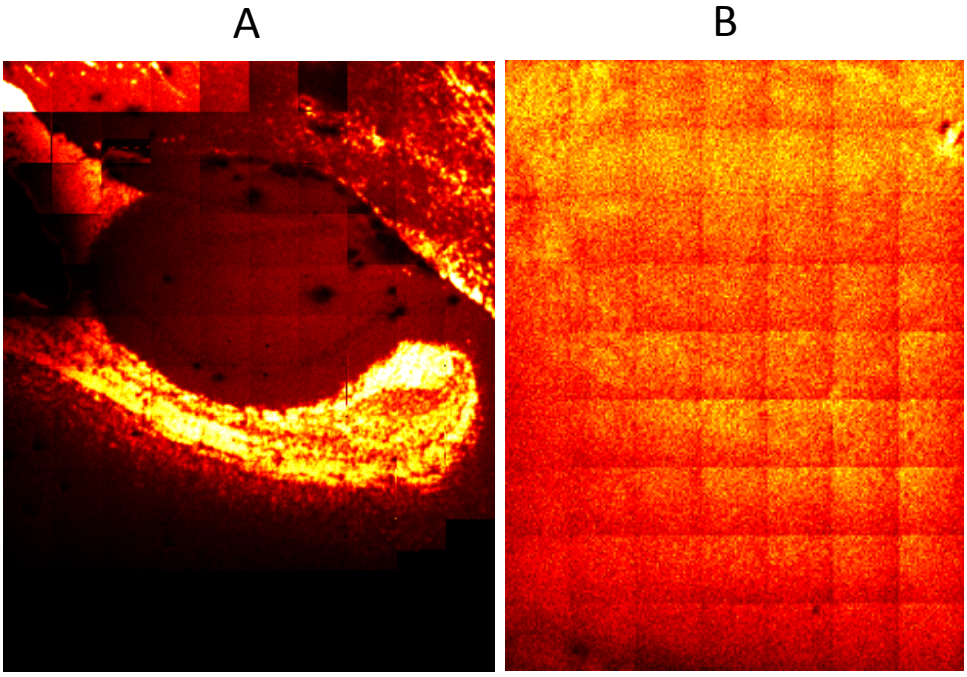

Figure 40: Total Ion Images for pre (A) and post (B) 0.02% Thioflavin T staining of a triple transgenic mouse brain, hippocampus region. A) Analysed with the C_{60}^{+} primary ion beam, a spot size of 7.8 µm, a current of 10 pA, 250 µm x 250 µm tile size, 32 x 32 pixels, ion dwell was 200 shots, a 50% duty cycle, for a total ion dose of 2.05E12. B) Analysed with the C_{60}^{+} primary ion beam, a spot size of 7.8 µm, a current of 4 pA, 250 µm x 250 µm tile size, 32 x 32 pixels, ion dwell was 200 shots, a 75% duty cycle, for a total ion dose of 1.23E12.

Additionally, most staining protocols call for a fixation agent to be used to prevent distension. This however was not possible since such fixation agent would be everywhere in the tissue and would thus overwhelm the mass spectrum analysis, leading to oversaturation or a loss of signal as described by Brunelle.[104] Therefore, extreme care had to be taken to limit the damage to the tissue. A common means of washing the tissue after staining is by placing the tissue under slowly moving water, but without a fixation agent, this would result in the total degradation of the tissue. Instead the tissues on silicon wafers were carefully placed into small glass tubes for

all the washings. Some protocols called for very long washes but these were shortened to maintain tissue integrity.[112,113] Instead of long washes as the literature suggests, each wash was only performed for 1 minute, thus preventing tissue decay.

Another consideration was the concentration of the dehydration and washing solutions. Most protocols call for dehydration and washes to be done in pure or very concentrated ethanol for an extended period of time.[114-116] However, such strong concentration of ethanol would dissolve the lipids and cholesterol when left to wash for 20 to 30 minutes. This was something that could not be avoided. No matter how short these washes were, most of the lipids would dissolve. Figure 41 compares the cholesterol distribution in a wild type mouse brain prior to ethanol wash (Figure 41, A) and then post ethanol wash (Figure 41, B). The cholesterol clearly has been dissolved in the ethanol washes. Since a large portion of this study was to correlate the lipid distributions to the location of the amyloid plaques, a procedure was developed where SIMS would be performed before and after staining. Once the location of the plaques was determined in the post-stain image, the pre-stained images could be analysed on the computer to determine the lipid chemistry surrounding the plaques.

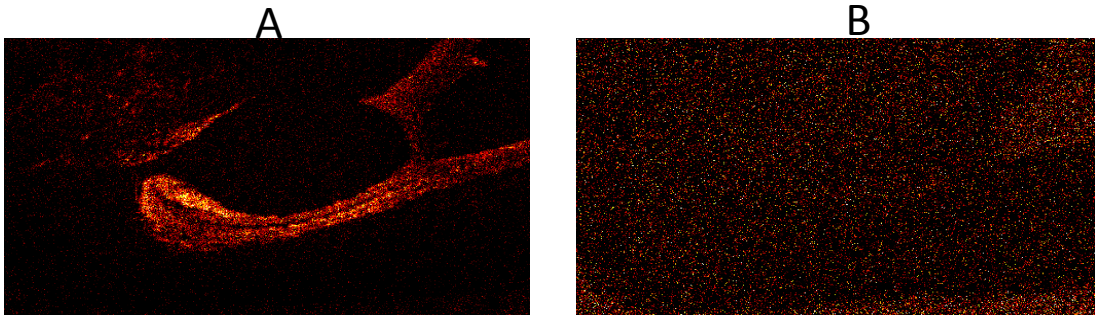

Figure 41: Pre and post stains of wild type mouse brain, hippocampus region, looking at cholesterol distribution (369 m/z). Tissue was stained as described in the next section, 7.2.2. Both tissue were images with the C_{60}^{+} primary ion gun with a 7.7 µm spot size, 22 pA, 250 µm x 250 µm tiles, 200 shots, 32 x 32 pixels, 24% duty cycle, 16 x 10 tiles for an ion dose of 2.16E12.

While the presence of ethanol dissolves the lipids, ethanol was essential for the washing away of unbound Thioflavin T from the tissue samples. If the ethanol solution was too strong, this could contribute to the disintegration of the tissue, but if the ethanol concentration were not strong enough, then oversaturation would occur. Thus an appropriate concentration for the washes had to be determined.

Finding this proper balance in ethanol concentration required much trial and error. So instead of staining and then analysing each trial with ToF-SIMS, a process that would take 5 hours for each sample, the tissue would be stained and then analysed with fluorescent microscopy, which only took minutes. Oversaturation and under staining can both be easily recognised with florescent microscopy, which allowed for a large number of trials. The concentration of ethanol washes ranged from 0% (all water) to 100% in these trials. Figure 42 compares, the fluorescent microscope images for two different wash protocols to illustrate the effect of different ethanol concentrations. Figure 42A was washed first with 80% ethanol and then 70% ethanol for 1 minute each, while Figure 42B was washed twice with 50% ethanol for a minute each. The stain washed with 80% ethanol and then 70% ethanol provides an excellent contrast between the stained plaques and the background while the two 50% ethanol washes result in an oversaturated background. Thus, the 80% ethanol and 70% ethanol one-minute washes were used for the staining protocol in this project as they provided excellent differentiation but were short and therefore preserved the integrity of the tissue.

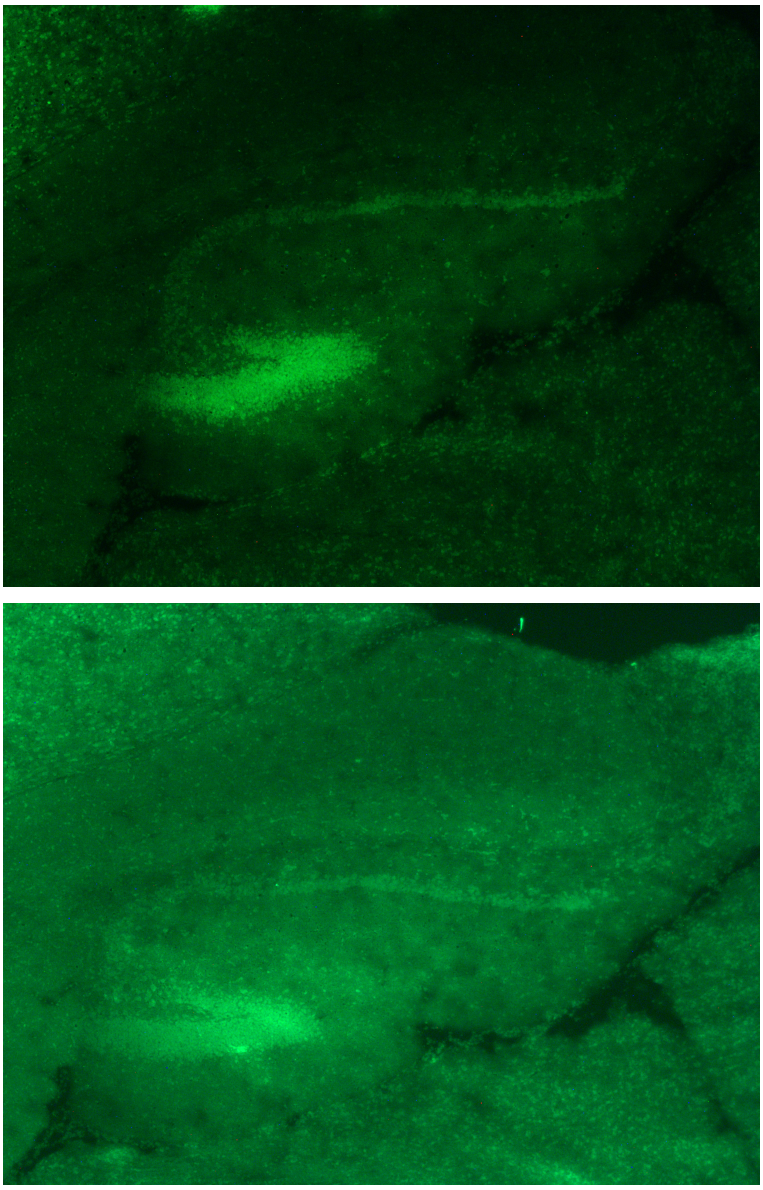

Figure 42: Fluorescent microscopic images of stained wild-type mouse brain, hippocampus region. Both tissues were dehydrated in 70% ethanol and 80% ethanol each for 1 minute before being stained in 0.002% Thioflavin dissolved in 80% ethanol for 8 minutes. A) This sample was washed in 80% ethanol and 70% ethanol for 1 minute each before being rinsed twice in deionised water each for a minute. B) This sample was washed twice in 50% ethanol for 1 minute each before being rinsed twice in deionised water each for a minute.

7.2.3 Staining Protocol

After initial ToF-SIMS analysis, samples were removed from the J105 3D chemical imager and placed into a desiccator with a vacuum pump attached. The samples were kept in the desiccator for an hour before they were removed. During this time, the Thioflavin T solution was prepared. 0.01 grams of Thioflavin T was dissolved in 80% ethanol to create a 0.02% Thioflavin T solution. A 1.5 mL aliquot from the 0.02% Thioflavin T solution was then added to 13.5 mL of 80% ethanol to form a 0.002% Thioflavin T solution. To remove undissolved micelles, the solution was then filtered through a 0.2 μm membrane syringe into a new glass container.

After desiccation, the tissue was removed and placed into a solution of 70% ethanol for 1 minute. Next it was placed into a solution of 80% ethanol for 1 minute before being moved into the 0.002% Thioflavin T solution for 8 minutes. After the staining, the tissue was a bright yellow and needed to be differentiated with washes. The tissue was then placed into an 80% ethanol solution for a minute followed by washing another minute in a 70% ethanol solution. Finally, the tissue was placed into deionised water for 1 minute and then moved to another glass container of deionised water and allowed to wash for an additional minute. After the washes were complete, the tissue lost the majority of its colouring and was placed back into the desiccation vacuum for an hour. Once desiccation had been completed, the tissue was placed back into the ToF-SIMS for post-stain analysis.

Fluorescent imaging was carried out after the post-stain ToF-SIMS analysis. All fluorescent imaging used the Olympus BX51 fluorescent microscope with a FITC filter. Fluorescent images were captured by the computer program Olympus Cell^{F} and saved to a flash drive.

7.2.4 SIMS Conditions

The 20 keV C_{60}^+ primary ion beam was used for all tissue analysis done in this dissertation. Attempts were made with the Ar_n^+ cluster ion beam, but the charging with this beam was unable to be resolved. All tissue samples, whether stained or unstained, were desiccated under vacuum for one hour prior to analysis. The silicon with the tissue sample was secured to a copper sample stub by small screws. This stub was placed into the ToF-SIMS sample prep and moved into the analysis chamber using the Ionoptika automated sample handling. Once in the ToF-SIMS analysis chamber, the current of the ion beam was measured in a Faraday cup on the sample stub and then noted. Next, the spot size was determined by measuring the edge of a mesh grid, which covered a different Faraday cup on the sample stub. The spot size correlated to the size beam and the spot size thus would be the size of the pixels (e.g. if the spot size was 7.5 μm, then each pixel would be 7.5 μm). Once spot size and current were determined, the optical gate was aligned on the edge of the silicon wafer, but not on the tissue. The optical gate is the field of secondary ions that is produced by sputtering. When the optical gate is aligned, this ensures that the extraction field is directly above where the secondary ions are being produced, which maximises secondary ion yields. After alignment, the optical gate was checked on the tissue, either using very weak beam strength or on an unwanted portion of the tissue. This was performed because the optical gate shifts as the height of the sample changes and the tissue is slightly higher than the silicon wafer. Finally, the stage bias was checked. The bias voltage was checked at several values to determine which voltage resulted in the greatest secondary ion yields.

Once the stage bias was determined, experimental conditions were set. The total ion dose, which is the total amount of ions that impact each cm^2 of tissue, is the most important to keep consistent from experiment to experiment because this allows the secondary ion yields to be compared from tissue to tissue. In order to keep the total ion dose consistent, there were several variables that could be adjusted. The first of these was the current of the primary ion beam. If the beam current were increased, this would cause an increase in total ion count. Additionally, if the number of pixels per raster area were increased, this would increase the number of shots and thus increase the total ion dose. Finally, the duty cycle could be changed to control the total ion dose. The duty cycle controls how many ions are being allowed to hit the sample (i.e. if the duty cycle is 50%, then the ion beam is on for 50% of the time).

For the experiments described in this section, the total ion dose was maintained as close as possible to 2.0E12 ions/cm^2. The current ranged from 8 pA to 22 pA and the spot size ranged from 4.5 μm to 8 μm. The total shots were maintained at approximately 200 shots, but in later experiments were increased to 500 shots. The duty cycle ranged the most extensively, from 15% to 80%, but this was varied to maintain a consistent total ion dose. Pixels per rastered area generally was 32 by 32, but this was dependent upon the spot size.

Early experiments imaged the entire mouse brain, but these would often take 8 to 16 hours, so later experiments focused only on the isocortex and the hippocampal regions. Data collected from experiments were analysed using Image Analyser, by which the total ion mass spectrum and individual ion images were generated.

7.3 Tissue Analysis Results

To determine if the stain was successful, the post-stained transgenic brain tissue images were examined for high intensity spots of Thioflavin T's secondary ions of approximately 20 μm to 70 μm in size – correlating to amyloid plaques. After seeing these on several of the stained transgenic tissues, the post-stained wild-type tissue images were examined to demonstrate that these spots were something truly unique to the transgenic mice brains. Finally, fluorescent images of the transgenic mouse brains were taken to confirm that the high areas intensity area of Thioflavin T secondary ions were in fact Thioflavin T. The first set of representational images for the unstained wild type mouse brain (Figure 43-Figure 49) is presented below:

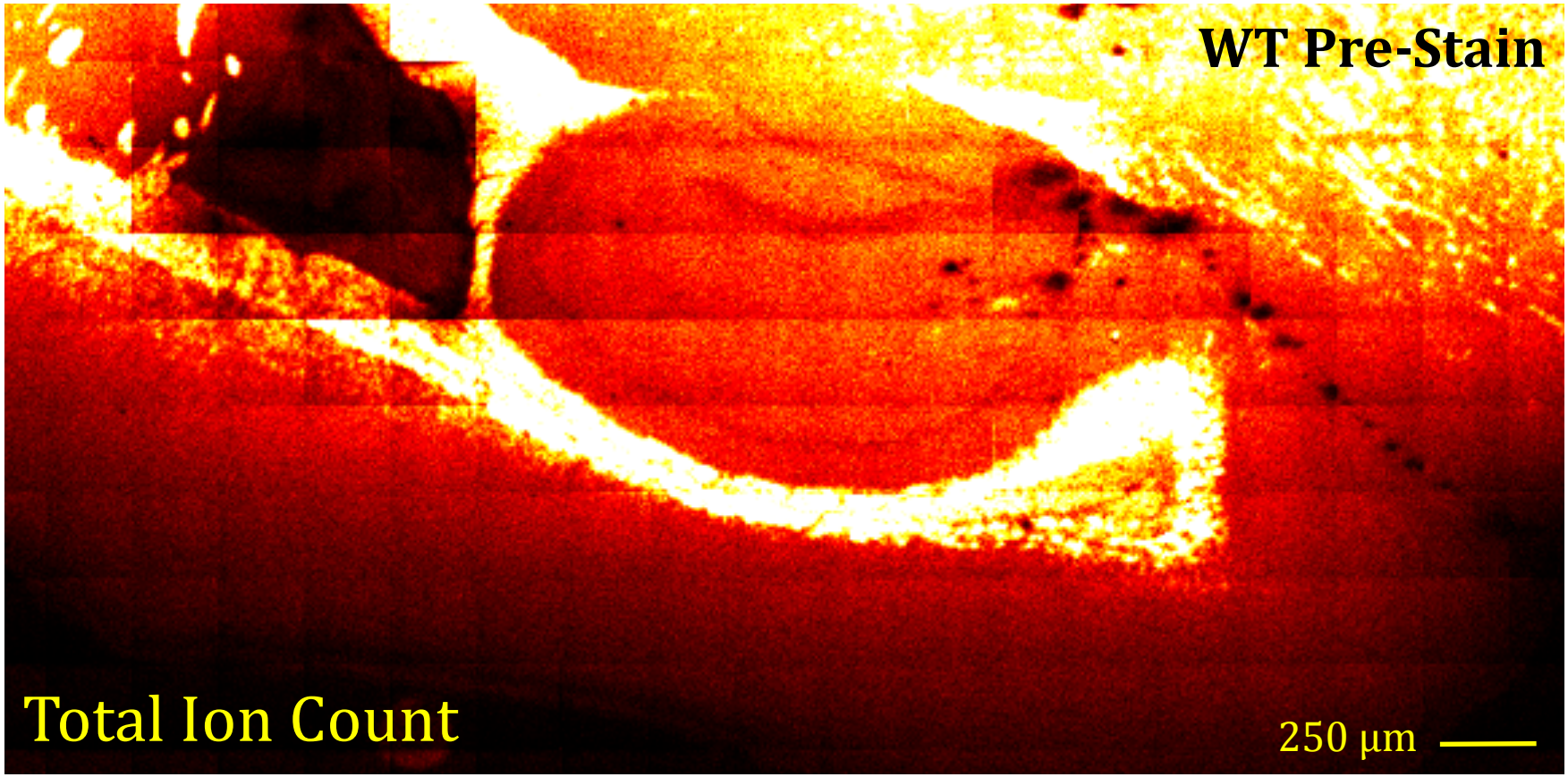

Figure 43: Total Ion Count for wild-type mouse brain anaylsis - hippocampus and isocortex regions shown. Pre-stain analysis was done with the following parameters: C_{60}^{+} primary ion beam, spot size 7.8 µm, current 10 pA, tile size 250 µm x 250 µm, pixels 32 x 32, ion dwell 200 shots, duty cycle 50%, total ion dose 2.03E12 ions/cm^2. A stage bias of 45 Volts was added to the sample. Analysis was done with Image Analyzer.

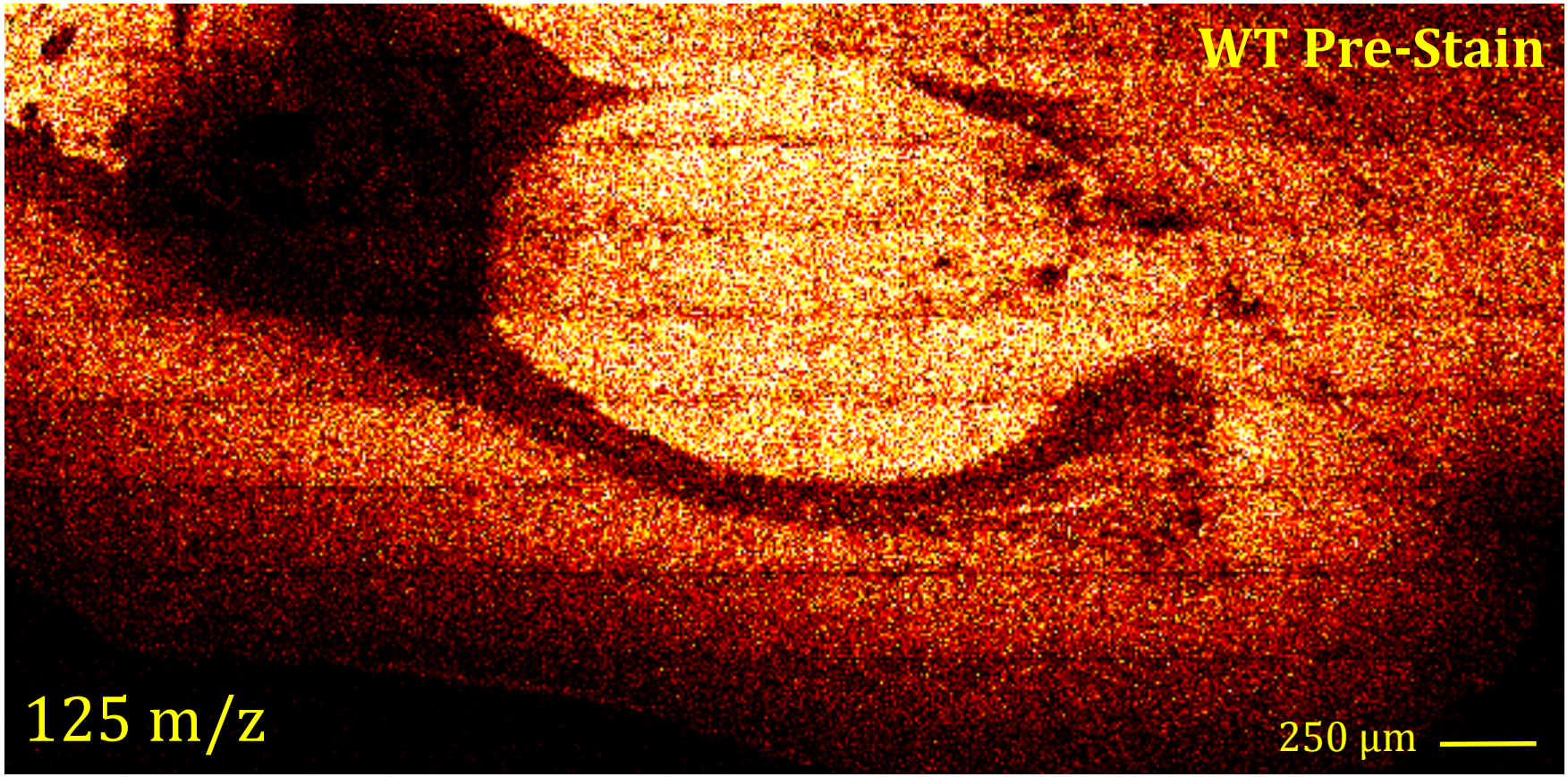

Figure 44: The same sample as Figure 43, but image depicts the yields for the secondary ions with a mass-to-charge ratio of 125 m/z. This fragment is from the phosphate head of phosphonosphingolipids. These phosphate heads are present throughout the hippocampus and isocortex regions, but very few are found in the white matter.

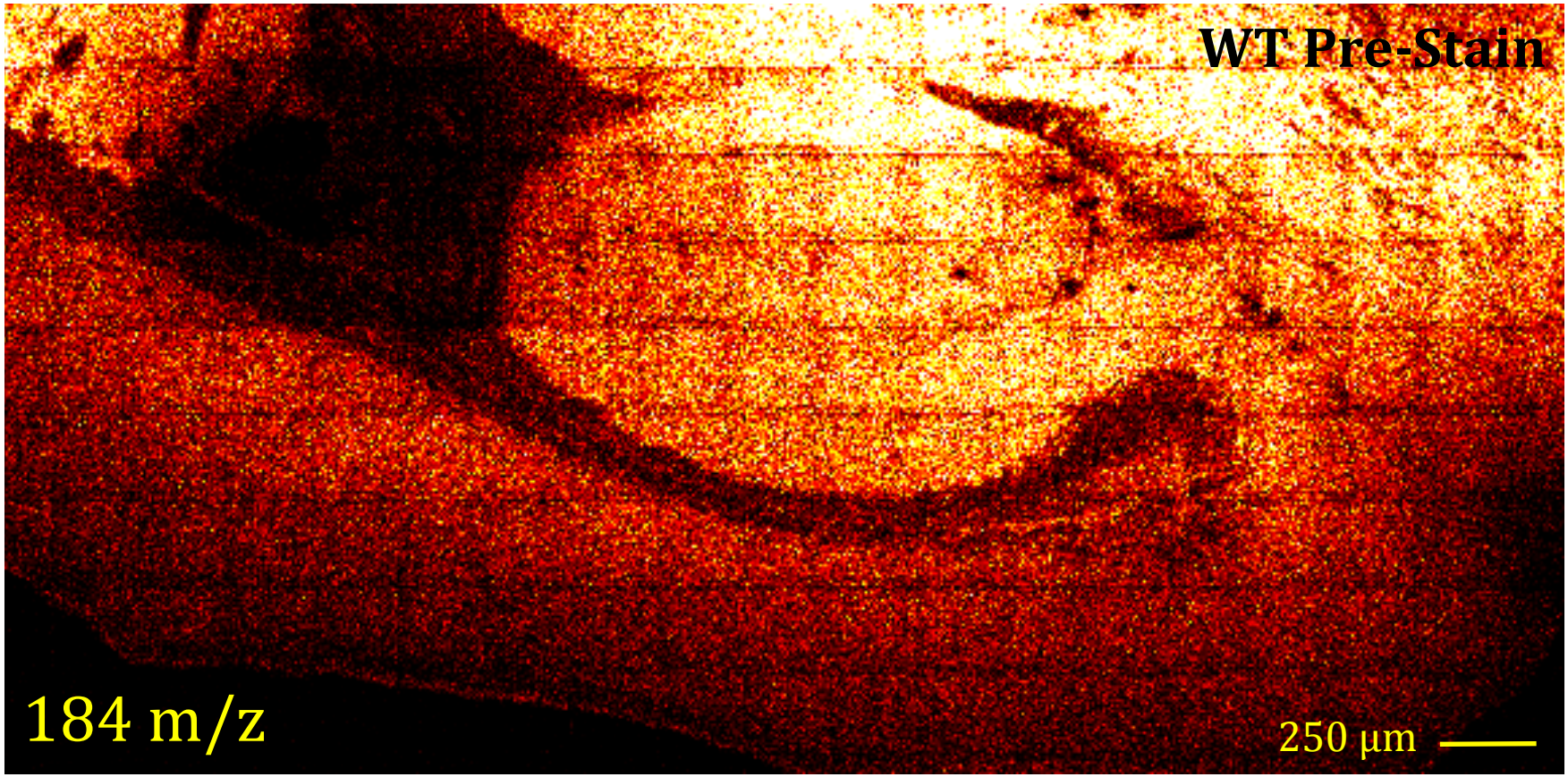

Figure 45: The same sample as Figure 43 &Figure 44, but image depicts the yields for the secondary ions with a mass-to-charge ratio of 184 m/z. This fragment is a larger ion from the phosphate head of phosphonosphingolipids. Again these phosphate heads are present throughout the hippocampus and isocortex regions and have a similar concentration as the 125 m/z fragments.

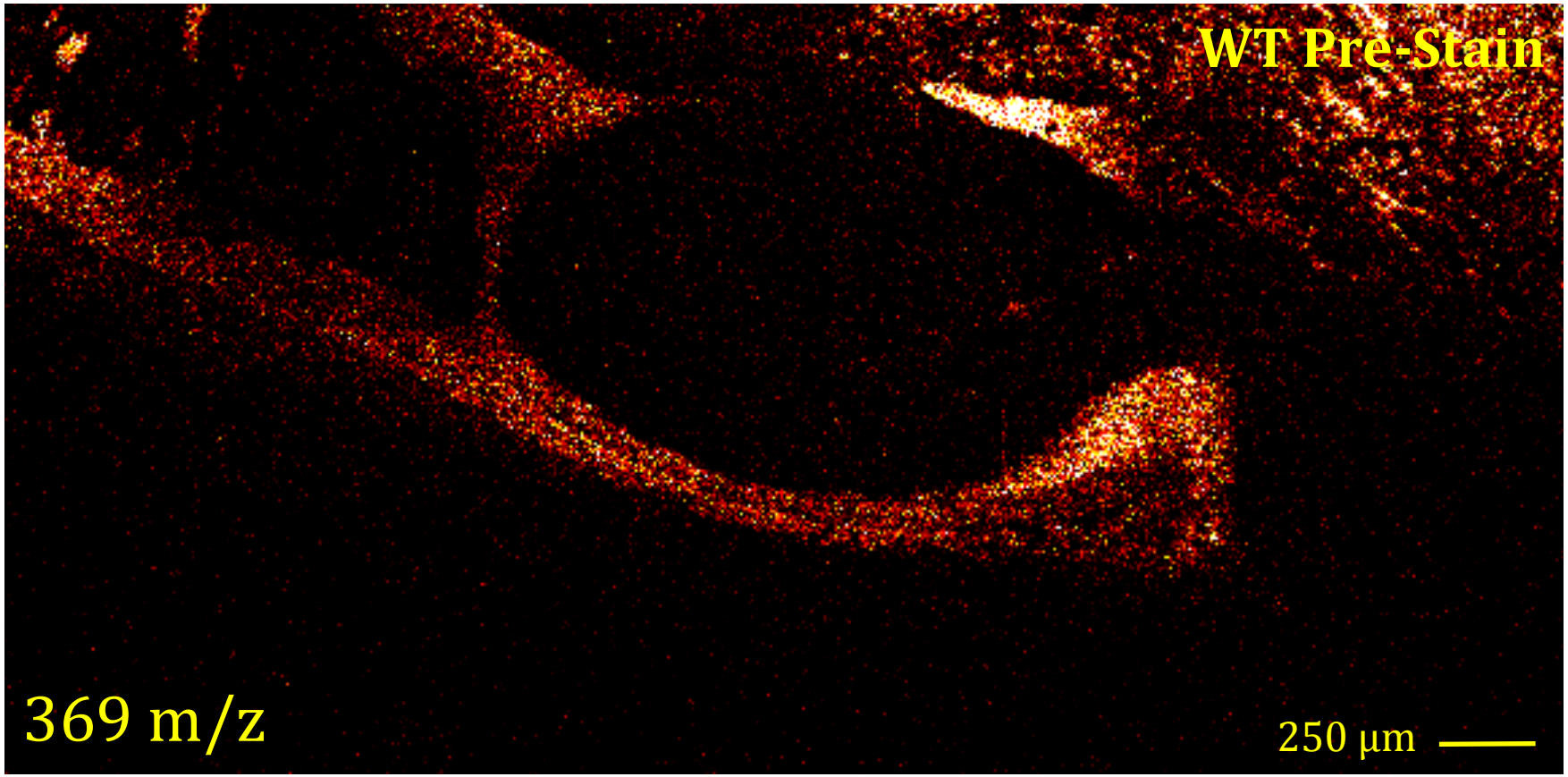

Figure 46: The same sample as Figure 43-Figure 45, but this image depicts the yields for the secondary ions with a mass-to-charge ratio of 369 m/z. This secondary ion is a fragment of chloestrol. Cholesterol is seen in high frequency in the white matter regions surrounding the hippocampus. Very little cholesterol is found in the hippocampus or isocortex.

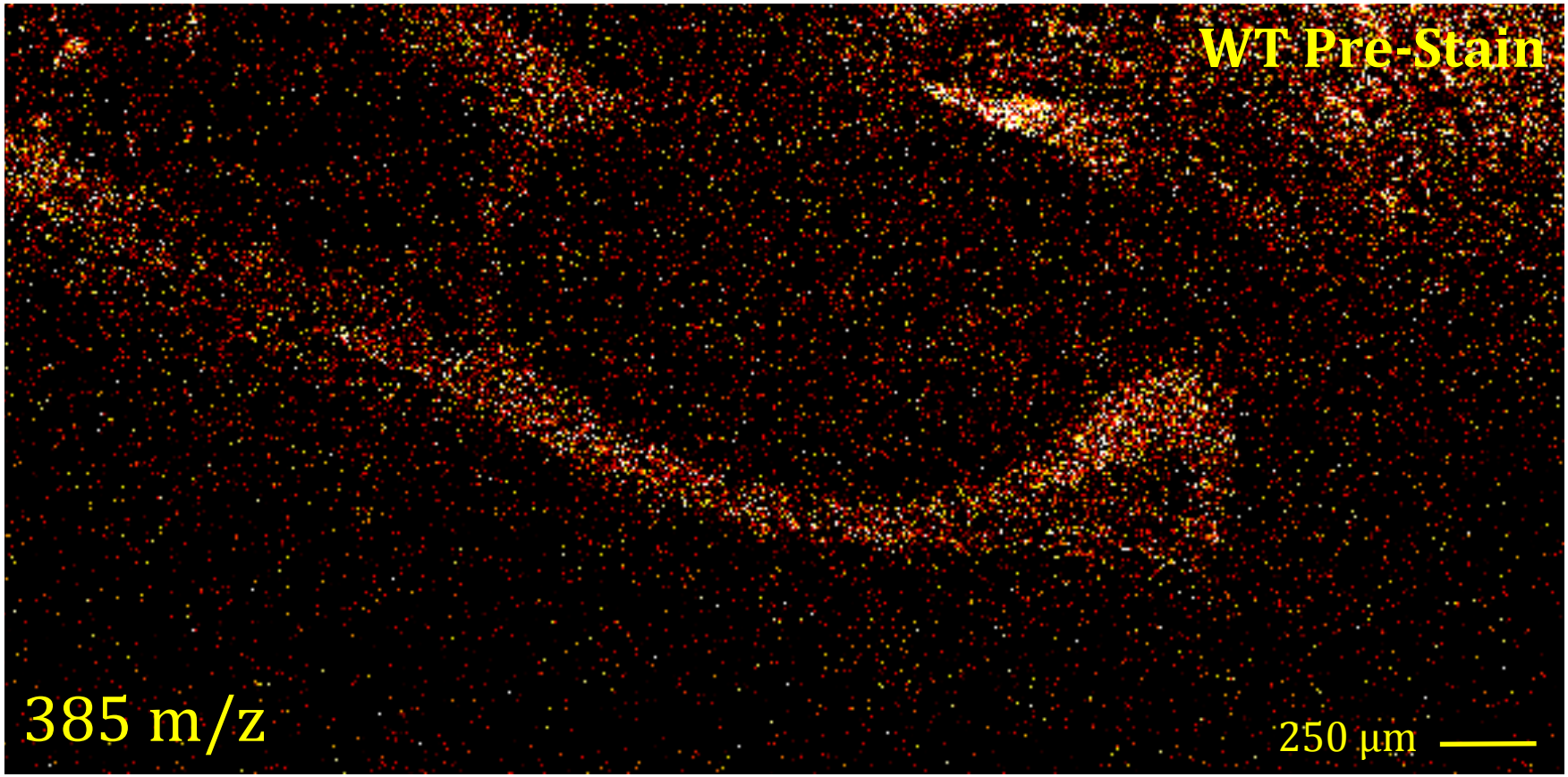

Figure 47: The same sample as Figure 43-Figure 46, but this image depicts the yields for the secondary ions with a mass-to-charge ratio of 385 m/z. This secondary ion is a larger fragment of cholestrol. This fragment is seen with less intensity in the white matter than was seen with the secondary ion 369 m/z, however there does appear to be a greater frequency of this cholesterol fragment in the hippocampus and isocortex.

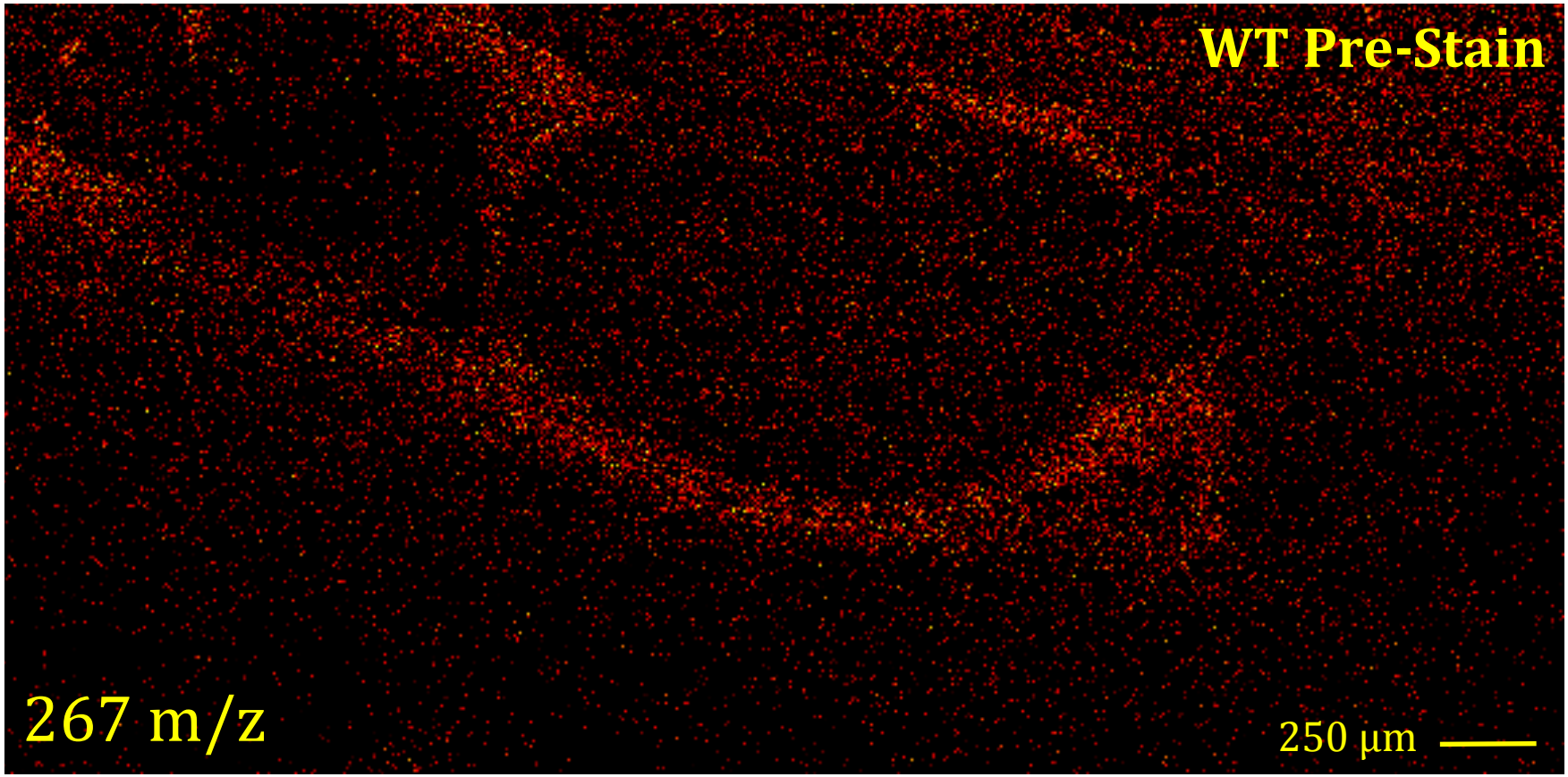

Figure 48: The same sample as Figure 43-Figure 47, but this image depicts the yields for the secondary ions with a mass-to-charge ratio of 267 m/z. The secondary ion with a mass-to-charge ratio of 267 m/z is the characteristic fragment for the Thioflavin T molecule as determined in earlier experiments. Areas of high intensity are not seen, but rather diffused background.

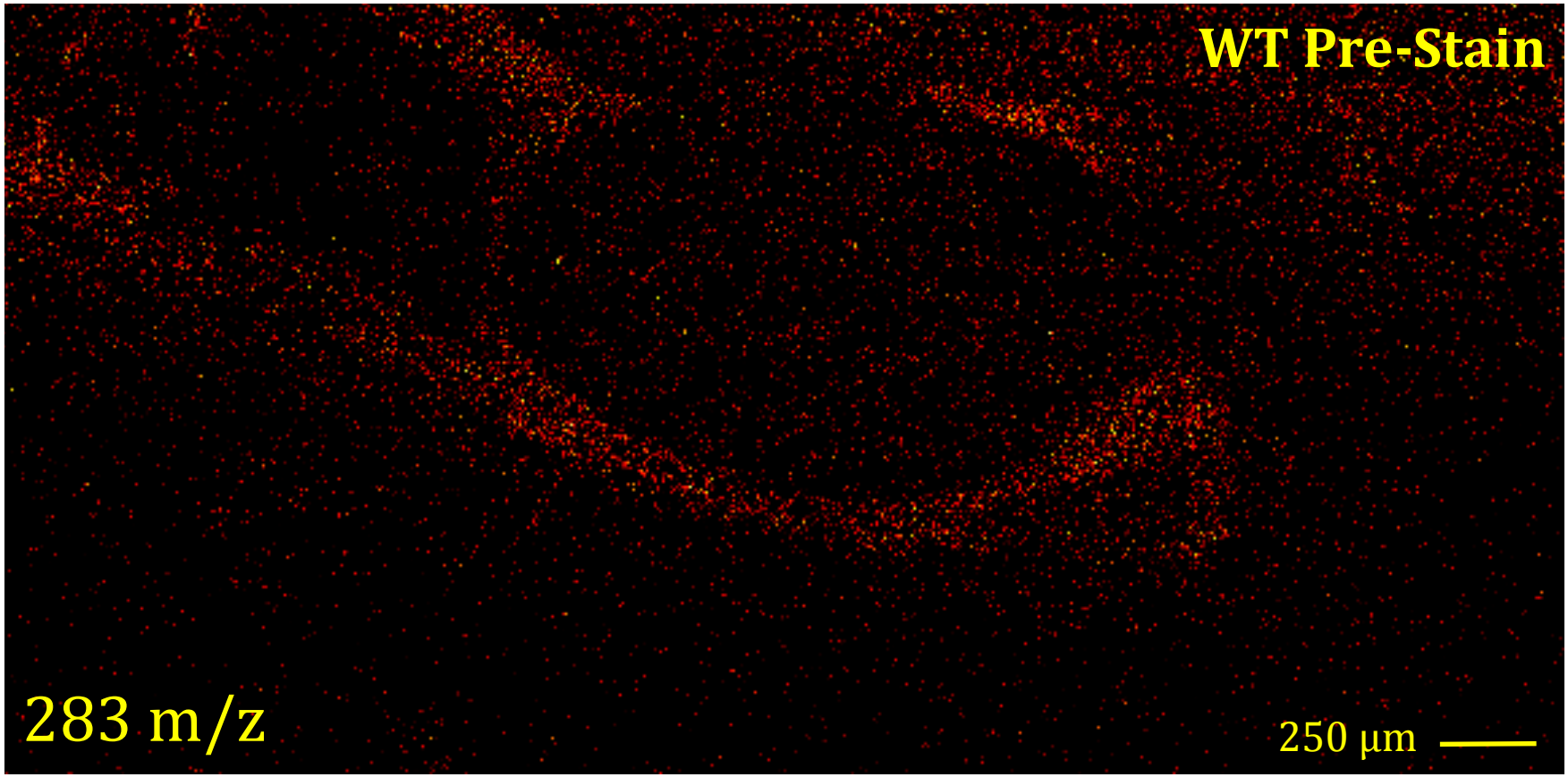

Figure 49: The same sample as Figure 43-Figure 48, but this image depicts the yields for the secondary ions with a mass-to-charge ratio of 283 m/z. This secondary ion is the second most frequent fragment for the Thioflavin T molecule as determined in earlier experiments.

These seven figures provide a baseline for all other experiments. The first (Figure 43) provides the Total Ion Count, illustrating the frequency of all ions. The dark area near the top left of this image is a cross section of the lateral ventricle, part of the larger ventricular system in the brain that contains the cerebrospinal fluid. In the image above, no cerebrospinal fluid remains, but instead what is seen in this empty space is the silicon wafer below. Another area of darkness can be seen at the bottom of the image; this is where the brain tissue ends and once again only the silicon wafer is present. Areas of high intensity can be found in the white matter surrounding the hippocampus and isocortex, correlating to the rich cholesterol deposits found in this region.

Figure 44 & Figure 45 show the mass spectrum images for fragments of the phosphate head of phosphonosphingolipids, 125 m/z and 184 m/z respectively. As expected, the phosphate head of phosphonosphingolipids is plentiful in both the isocortex and the hippocampus region. The distribution of the ions can be seen throughout these two regions, but there might be some charging occurring near the bottom edge of the sample. There is also a noticeable lack of phosphate head fragments in the white matter surrounding the hippocampus – also an expected result.

In Figure 46 & Figure 47, the single ion images, 369 m/z and 385 m/z respectively, for cholesterol are presented. The frequency and distribution of these ions are different than the fragments presented in Figure 44 & Figure 45. Here, areas of high intensity are found in the white matter of the brain with a few diffuse deposits of cholesterol appearing in the hippocampus region. The intensity of the

369 m/z fragments is greater than that of the 385 m/z fragments, but these larger fragments are less common when using the C_{60}^{+} primary ion beam.

Finally, Figure 48 & Figure 49 are included to serve as a negative control, by showing that no major ion fragment is present at 267 m/z or 283 m/z, which is characteristic of Thioflavin T. While some background exists (most likely a less common fragment of cholesterol), there are no intense secondary ion fragments at this mass-to-charge ratio. Thus we are confident that fragments measured in stained samples are truly Thioflavin T fragments, not background noise.

The next set of images (Figure 50 through Figure 53) are from the same tissue that was seen in Figure 43-Figure 49, but these have been stained according to the protocol described in section 7.2.3. This set of images serves as another control, demonstrating that areas of high intensity are not seen when only the stain and no aggregates are present. Finally, Figure 53 is a fluroescent image of this post-stain sample, once again demostrating that no aggregates are present.

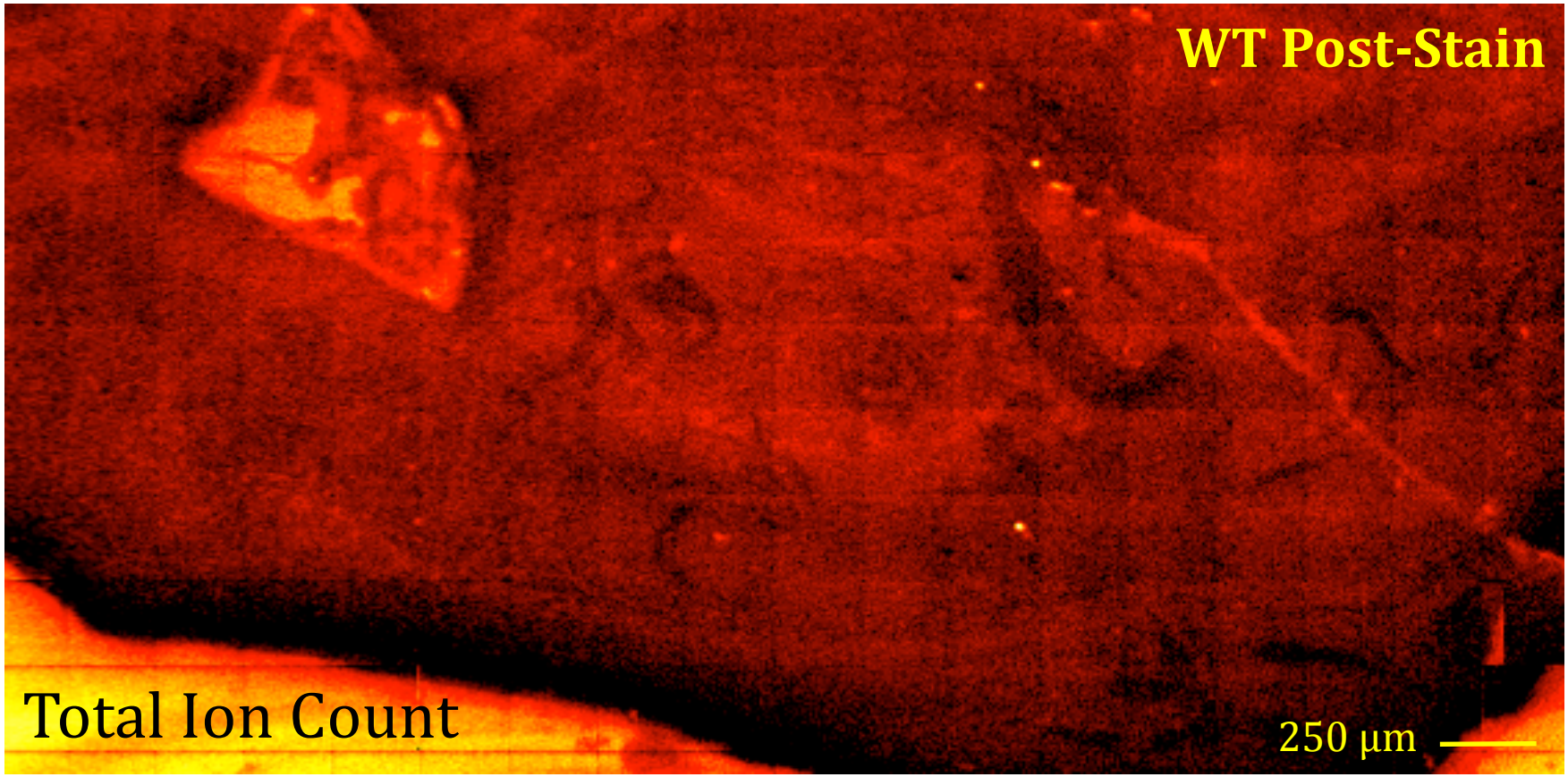

Figure 50: Same tissue as Figure 43-Figure 49, but the tissue has been stained according to the stain protocol described in section 7.2.3. Total Ion Count for wild-type mouse brain anaylsis - hippocampus and isocortex shown. Post-stain analysis was done with the following parameters: C_{60}^{+} primary ion beam, spot size 7.8 µm, current 19 pA, tile size 250 µm x 250 µm, pixels 32 x 32, ion dwell 200 shots, duty cycle 23%, total ion dose 2.02E12 ions/cm^2. A stage bias of 40 Volts was added to the sample.

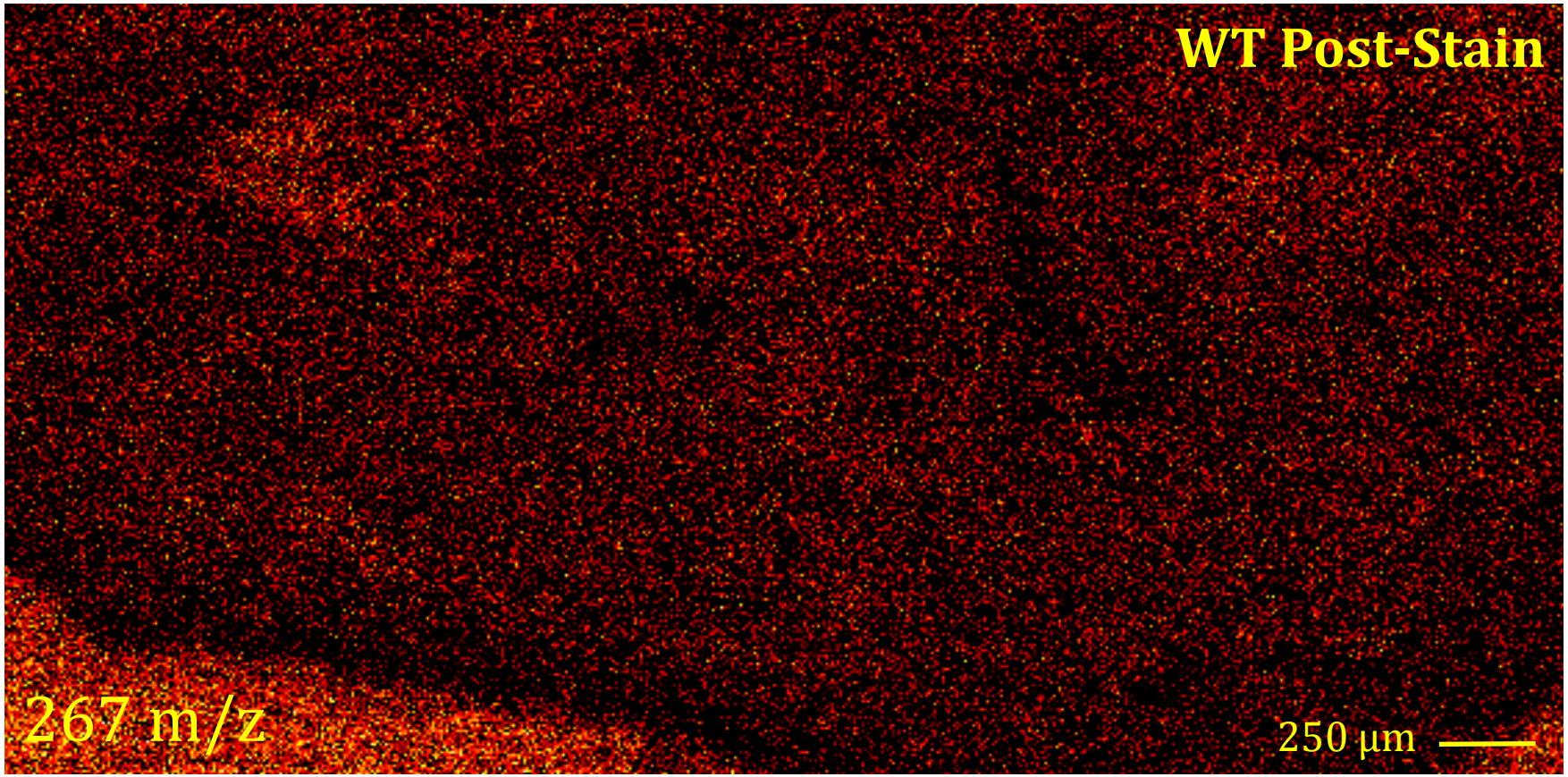

Figure 51: Same tissue sample as Figure 43-Figure 50, but this image depicts the yields for the secondary ions with a mass-to-charge ratio of 267 m/z - the characteristic fragment of Thioflavin T. This tissue has been analysed post-stain but there are no areas of high intenisty, which is consistent with the expectation that no amyloid aggregates would be present in the wild-type mice. This image was provided to illustrate that the stain is not responsible for production of areas of high intensity secondary ions that are seen when amyloid-beta aggregates are present.

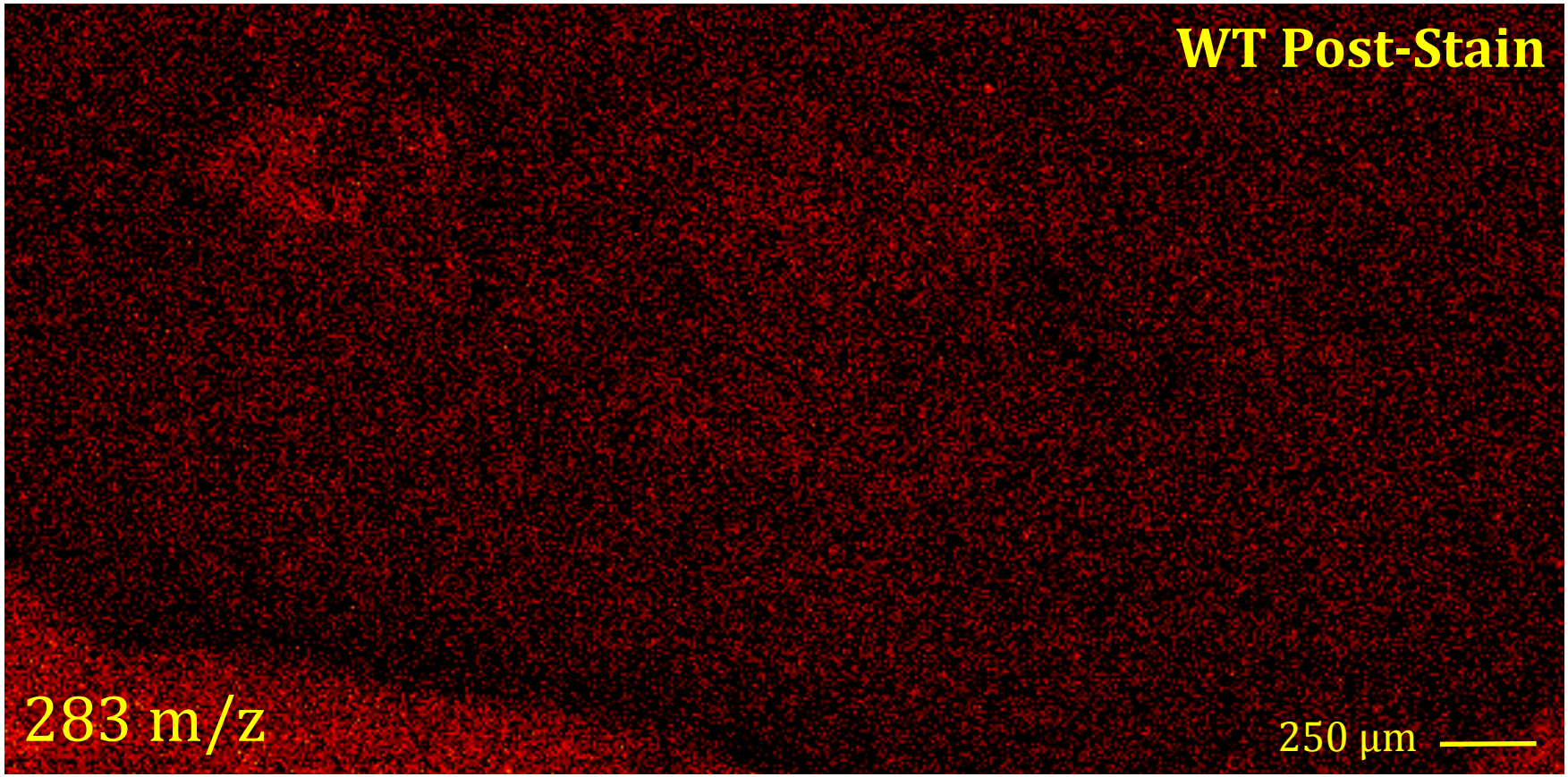

Figure 52: Same tissue sample as Figure 43-Figure 51, but this image depicts the yields for the secondary ions with a mass-to-charge ratio of 283 m/z – the second most abundant ion from Thioflavin T. Like the image above, only a background from the stain is seen and no areas of high intensity are found.

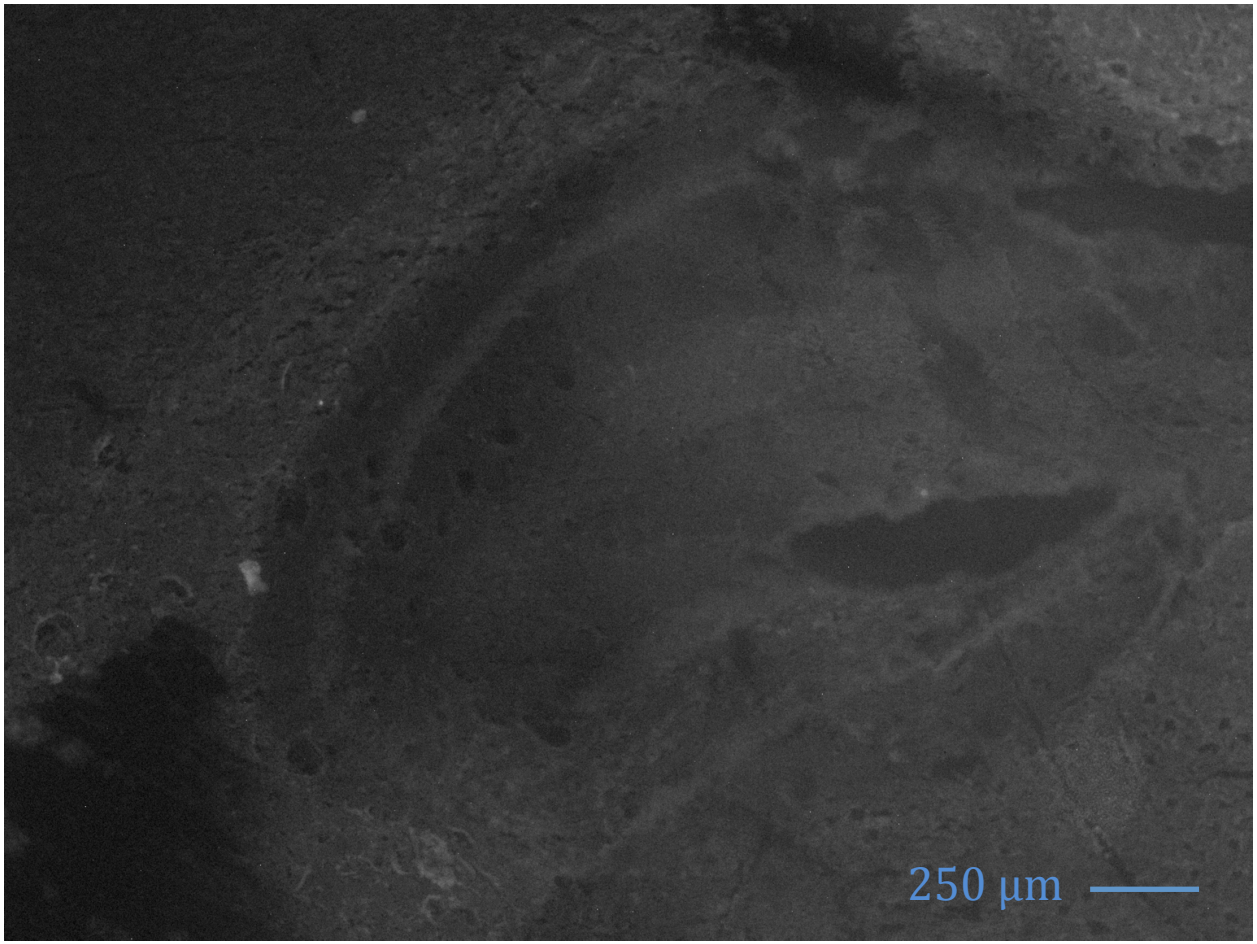

Figure 53: Fluorescent microscopy image of the hippocampal region of the tissue used in Figure 43-Figure 52. Tissue was imaged as described above in section 7.2.3. No areas of fluorescent intensity (like are seen in Figure 37) are seen in this image. This lack of fluorescent intensity/amyloid plaques is to be expected since this is a wild-type tissue sample.

Figure 50 is a total ion count image of a stained wild-type mouse brain and several noticeable differences can be seen when this is compared with the unstained wild-type total ion count image in Figure 43. Unlike the pre-stain TIC images in which the empty spaces in the tissue and the silicon wafer were dark, these areas are bright in the post-stained images due to unwashed away Thioflavin T ions. When this stain is compared to the stain in Figure 40, this staining protocol does not cause oversaturation. Additionally, in this post-stain TIC image, the white matter of this image is noticeably absent because the ethanol washes dissolved most of the lipids, though the overall structure of the tissue is intact because the structural proteins of the tissue do not dissolve.

In Figure 51 & Figure 52 of the post-stained wild type tissue, single ion images are generated for 267 m/z and 283 m/z, respectively – both characteristic fragments of the Thioflavin T stain. The purpose of these two mass spectrum images is to illustrate that no areas of high intensity are present due to staining process itself. Figure 53, the fluorescent microscope image of the same tissue, illustrates that there are no amyloid aggregates present, as is expected in the control sample. These three images serve as a negative control.

The next set of images (Figure 54-Figure 59), the triple transgenic mouse models (3xTg-AD) pre-stained tissue are analysed. These images will be compared to the stained 3xTg-AD tissue samples to see if any abnormal lipid distribution is seen surrounding the amyloid plaques.

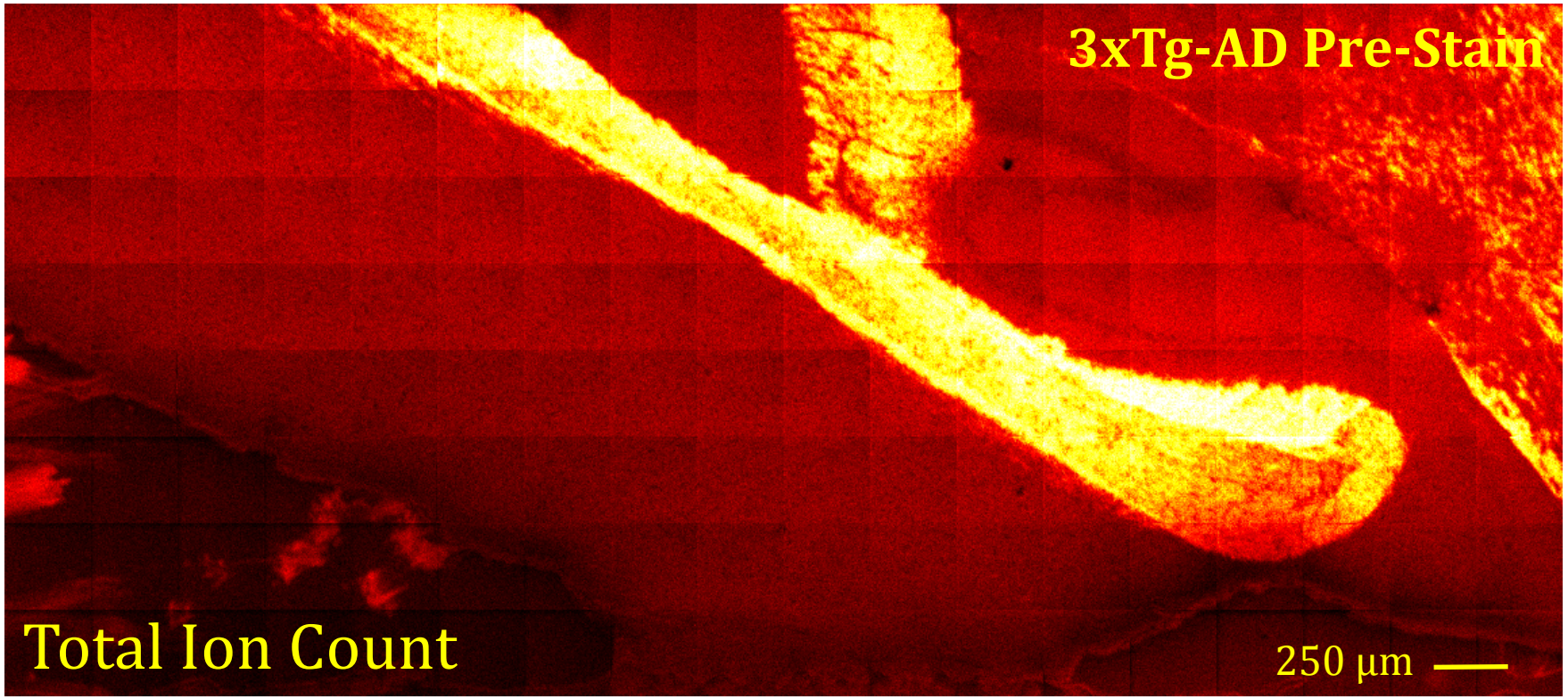

Figure 54: Total Ion Count for 3xTg-AD mouse model brain anaylsis - hippocampus and isocortex shown. Pre-stain analysis was done with the following parameters: C_{60}^{+} primary ion beam, spot size 4.5 µm, current 12 pA, tile size 290 µm x 290 µm, pixels 64 x 64, ion dwell 500 shots, duty cycle 12%, total ion dose 2.19E12 ions/cm^2. A stage bias of 40 Volts was added to the sample.

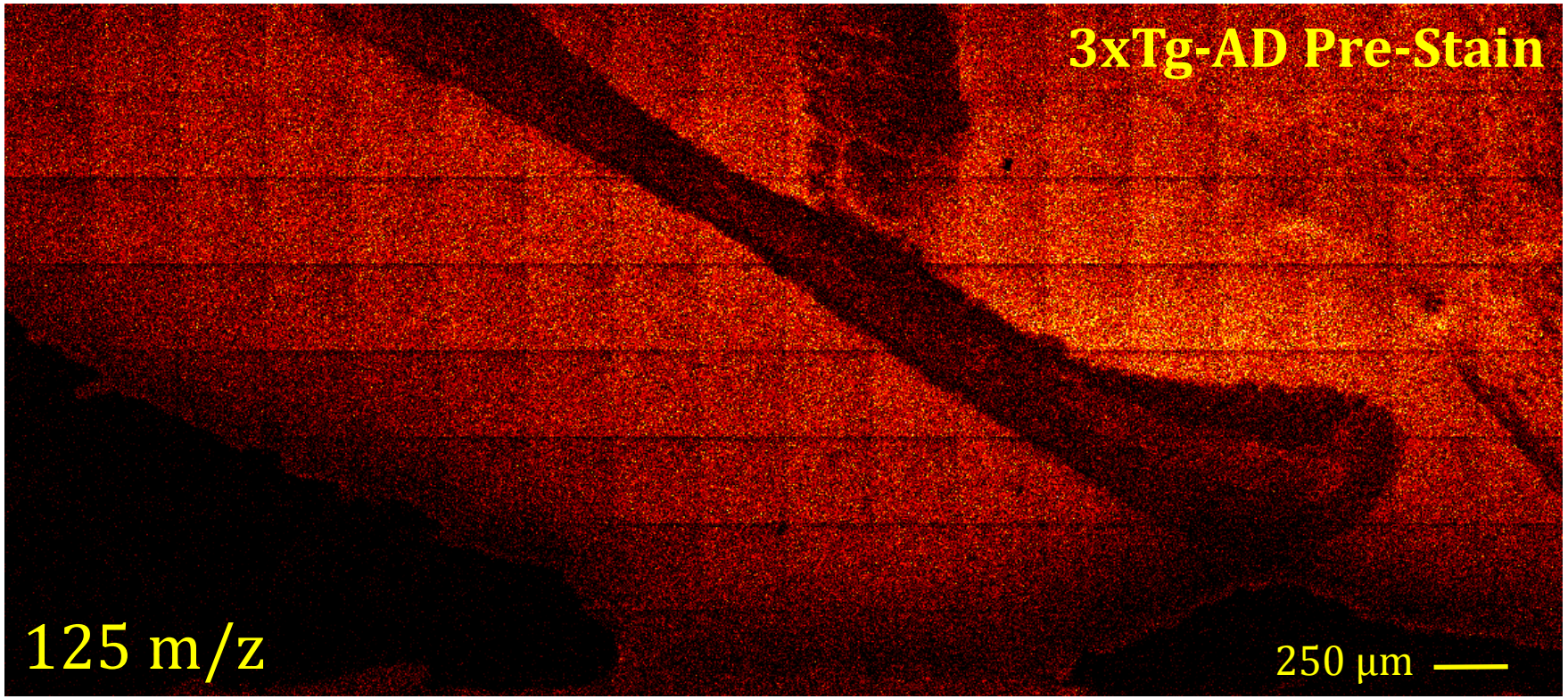

Figure 55: The same sample as Figure 54, but image depicts the yields for the secondary ions with a mass-to-charge ratio of 125 m/z - a fragment from the phosphate head of a phosphonosphingolipid. Once again, these phosphate heads are present throughout the hippocampus and isocortex regions, but very few are found in the white matter.

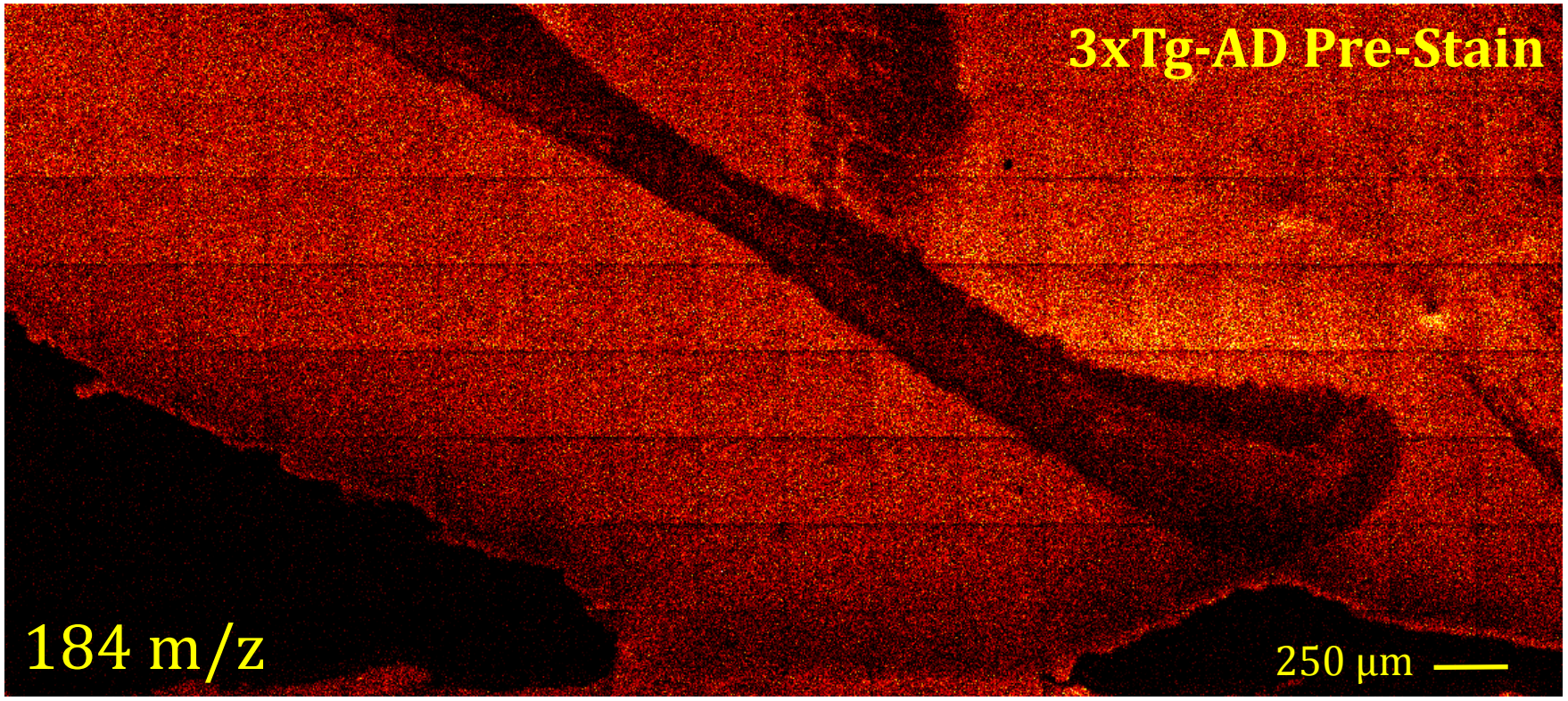

Figure 56: The same sample as Figure 54 & Figure 55, but image depicts the yields for the secondary ions with a mass-to-charge ratio of 184 m/z. This fragment is a larger ion from the phosphate head of a phosphonosphingolipid.

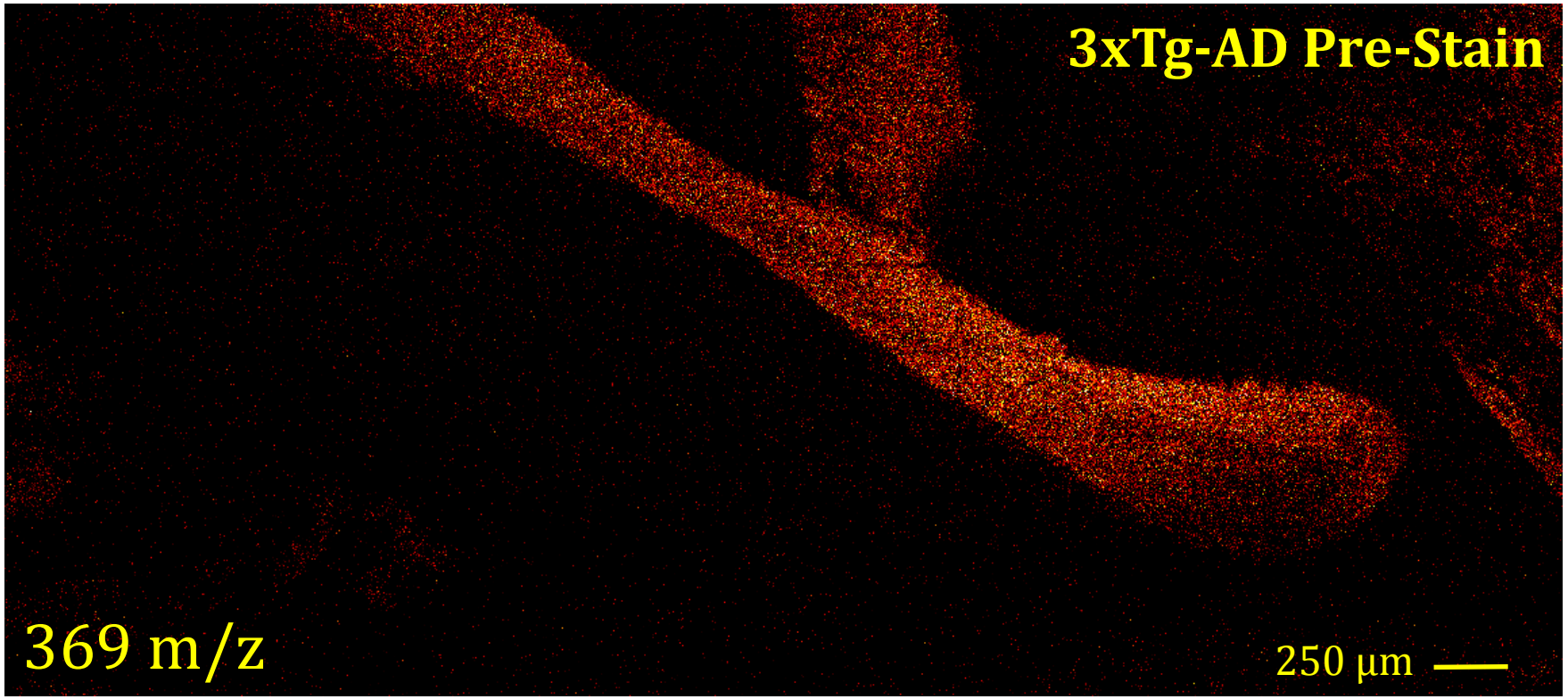

Figure 57: The same sample as Figure 54-Figure 56, but this image depicts the yields for the secondary ions with a mass-to-charge ratio of 369 m/z - a fragment of cholesterol. As in the wild-type tissue, the cholesterol is seen in high frequency in the white matter regions surrounding the hippocampus. The 3xTg-AD tissue does however have less cholesterol in the hippocampus or isocortex than the wild-type tissue.

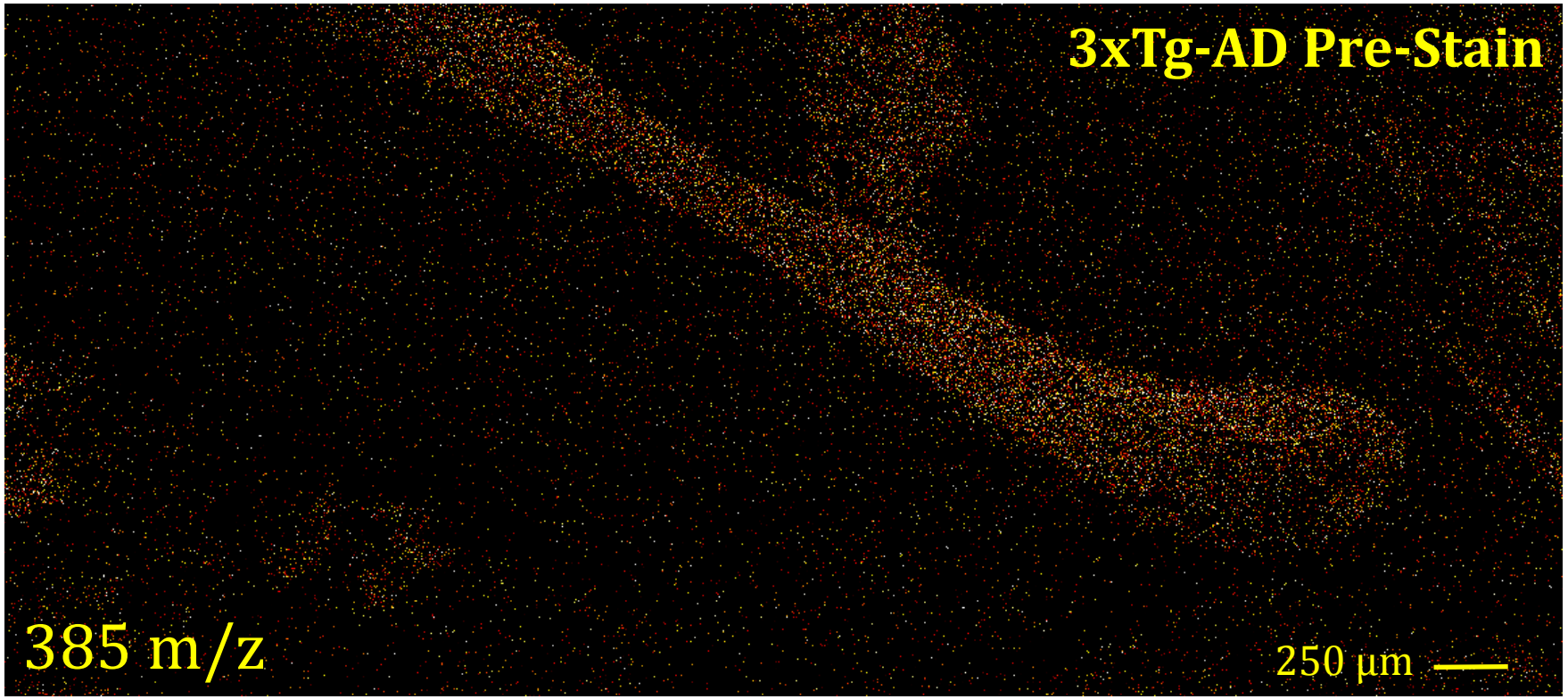

Figure 58: The same sample as Figure 54-Figure 57, but this image depicts the yields for the secondary ions with a mass-to-charge ratio of 385 m/z. This secondary ion is a larger fragment of cholesterol, but a less frequent secondary ion when compared to the cholesterol ion with a charge-to mass ratio of 369 m/z.

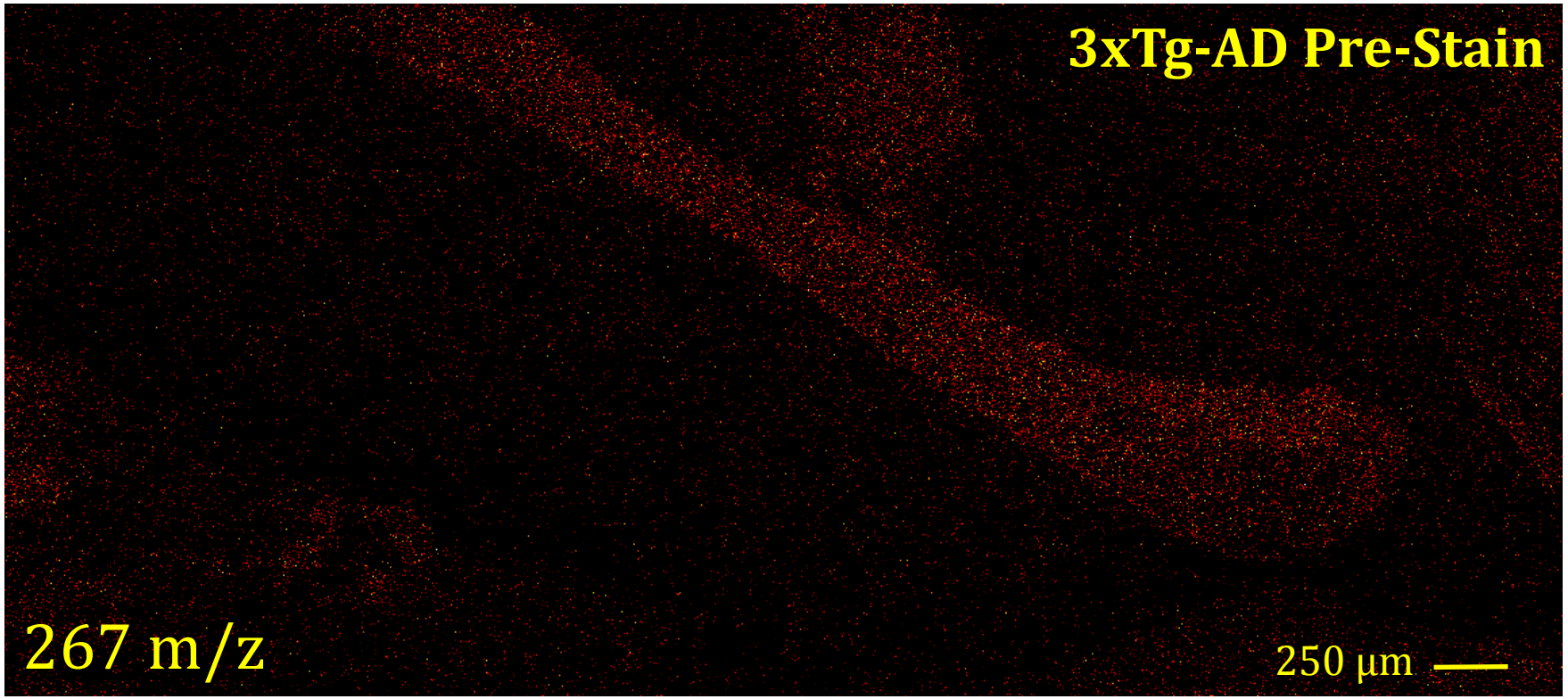

Figure 59: Same tissue sample as Figure 54-Figure 58, but this image depicts the yieids for the secondary ions with a mass-to-charge ratio of 267 m/z - the characteristic fragment of Thioflavin T. This a control showing that no areas of high intenisty can be seen prior to staining.

Figure 54 depicts the total ion count for the unstained 3xTg-AD mouse model brain tissue and the characteristic white matter can be clearly seen. This sagittal section was made closer to the midline of the brain than in the wild-type brain sample (Figure 43), which explains why the shape of the hippocampus and white matter appear slightly different and why the lateral ventricle is not seen. There is no evidence to suggest that either the medial or lateral portion of the hippocampus has an increased propensity to aggregate, so the depth of the sample should not matter.

In the single ion images for the 125 and 184 m/z fragments (Figure 55 & Figure 56, respectively), there appears to be very little variation when these are compared to the corresponding wild-type single ion images (Figure 44 & Figure 45). A similar ion distribution is seen and the intensity decreases as it nears the edge of the sample, most likely due to a bit of charging.

In the single ion images (Figure 57 & Figure 58) for cholesterol fragments, 369 m/z and 385 m/z, there appears to be a decrease in the frequency of cholesterol fragments in the isocortex and cortex. While several cholesterol deposits can be seen in the wild-type tissue samples (Figure 46 & Figure 47), they are notably absent in these mass spectrum images. The dispersed scattering of fragments in the bottom right corner correspond to the silicon wafer and might have been due to a bit of smudging when the tissue was placed on the silicon wafer.

Finally, Figure 59 gives the single ion image for characteristic fragment for Thioflavin T, 267 m/z, demonstrating once again that in this particular tissue, there are no corresponding fragments that could produce a false positive.

In the final set of images (Figure 60 - Figure 62), the stained 3xTg-AD tissues will be presented, demonstrating the areas of aggregation. Following these, the fluorescent image in Figure 63 shows that there appears to be aggregation present in this sample. Finally in Figure 64 & Figure 65, the fluorescent microscopy image will be overlaid onto the single ion mass spectrum images to illustrate the co-localisation of the stain.

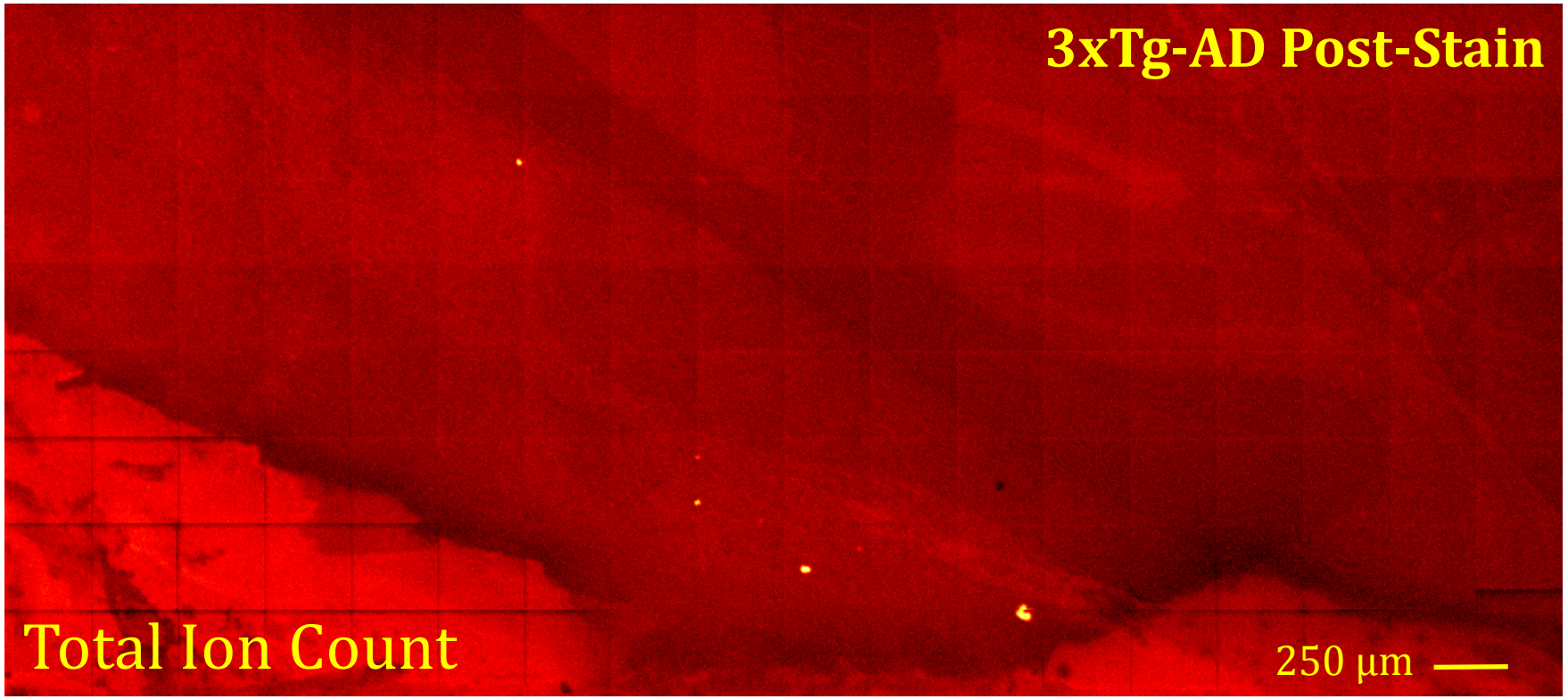

Figure 60: Same tissue as Figure 54-Figure 59, but the tissue has been stained according to the protocol described in section 7.2.3. Total Ion Count image of 3xTg-AD mouse model brain anaylsis - hippocampus and isocortex shown. Post-stain analysis was done with the following parameters: C_{60}^{+} primary ion beam, spot size 4.5 µm, current 11 pA, tile size 290 µm x 290 µm, pixels 64 x 64, ion dwell 500 shots, duty cycle 13%, total ion dose 2.18E12 ions/cm^2. A stage bias of 40 Volts was added to the sample. As was seen in the wild-type tissue, the ethanol washes dissolved most of the lipids resulting in less pronounced white matter.

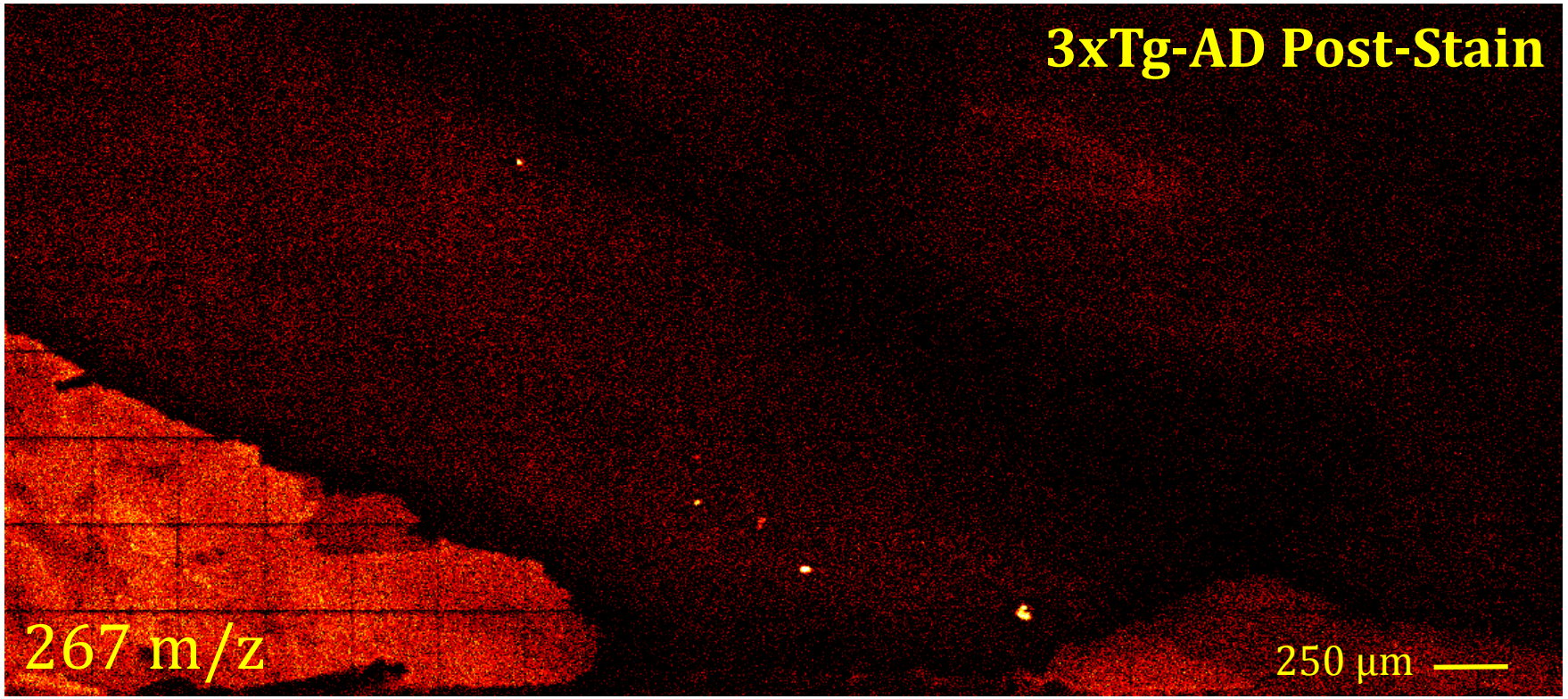

Figure 61: Same tissue sample as Figure 54-Figure 60, but this image depicts the yields for the secondary ions with a mass-to-charge ratio of 267 m/z - the characteristic fragment of Thioflavin T. The small dots of greater intensity are believed to be areas where Thioflavin T has bound to amyloid-beta aggregates and the increased concentration of Thioflavin T produced an increased secondary ion yield in those locations. The aggregates range in size from 50 µm to 20 µm in diameter. Fluroescent imaging was used to confirm that these were aggregates (shown in Figure 30).

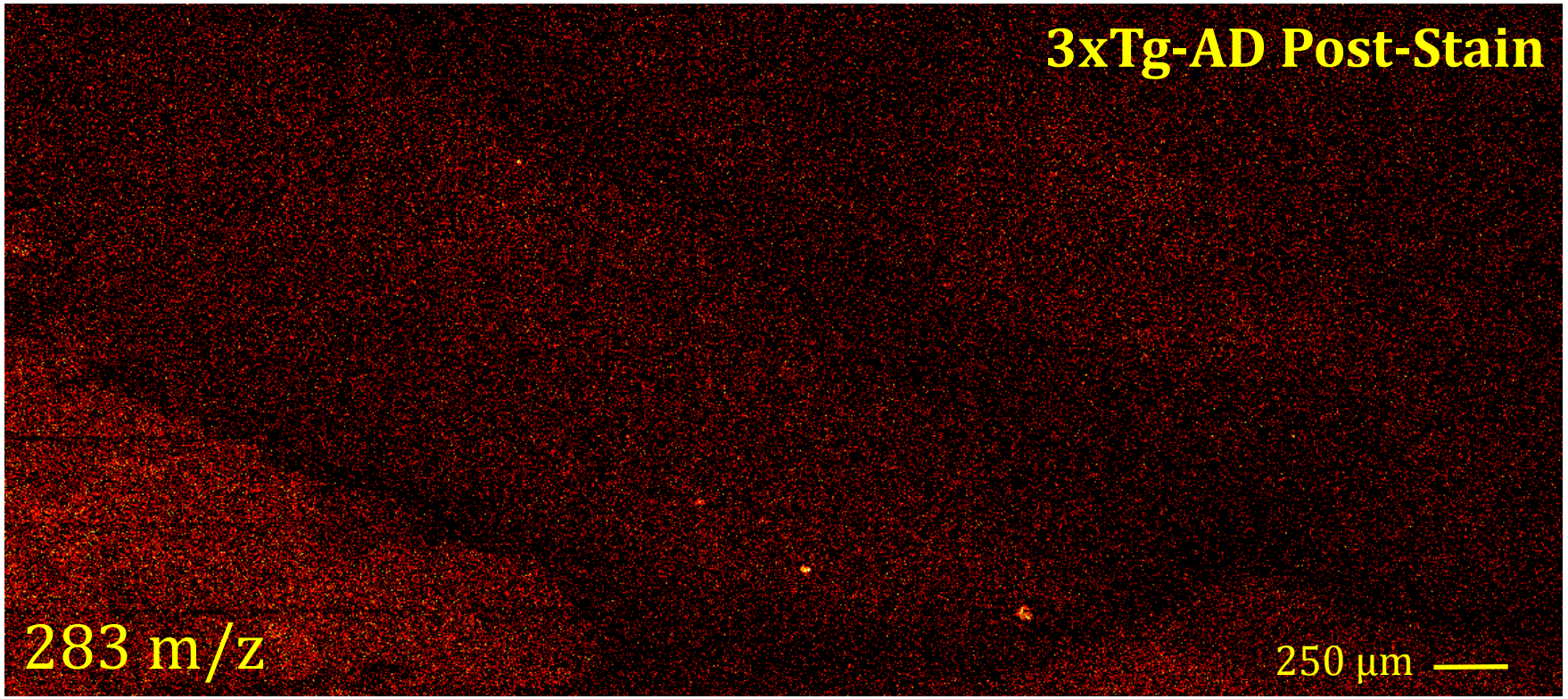

Figure 62: Same tissue sample as Figure 54-Figure 61, but this image depicts the yieids for the secondary ions with a mass-to-charge ratio of 283 m/z – the second most abundant ion from Thioflavin T. As in Figure 61, aggregates are seen in the isocortex but with less intenisty. This lesser intensity is due to the fact that this particular ion is a less abundant fragment of Thioflavin T. The co-localisation of these secondary ions provides further evidence that these areas of intensity correlate to Thioflavin T ions bound to amyloid-beta aggregates.

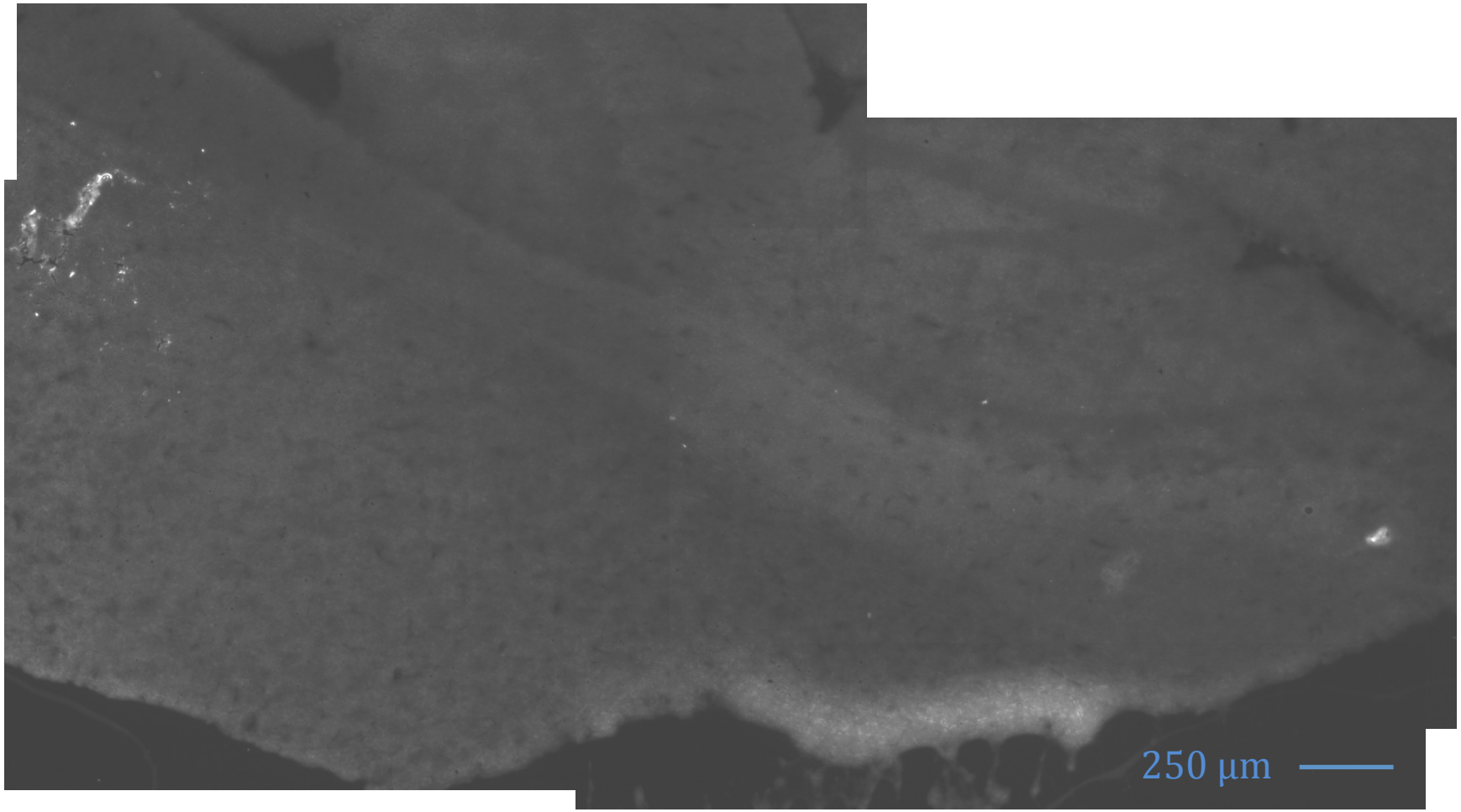

Figure 63: Fluorescent microscopy image of the tissue sample from Figure 54-Figure 62 – hippocampus and isocortex regions. Tissue was imaged as described in section 7.2.3. Several areas of fluorescent intensity are seen in this image corresponding the location of amyloid plaques. Image is a composite of several images stitched together to form a single larger image of the tissue.

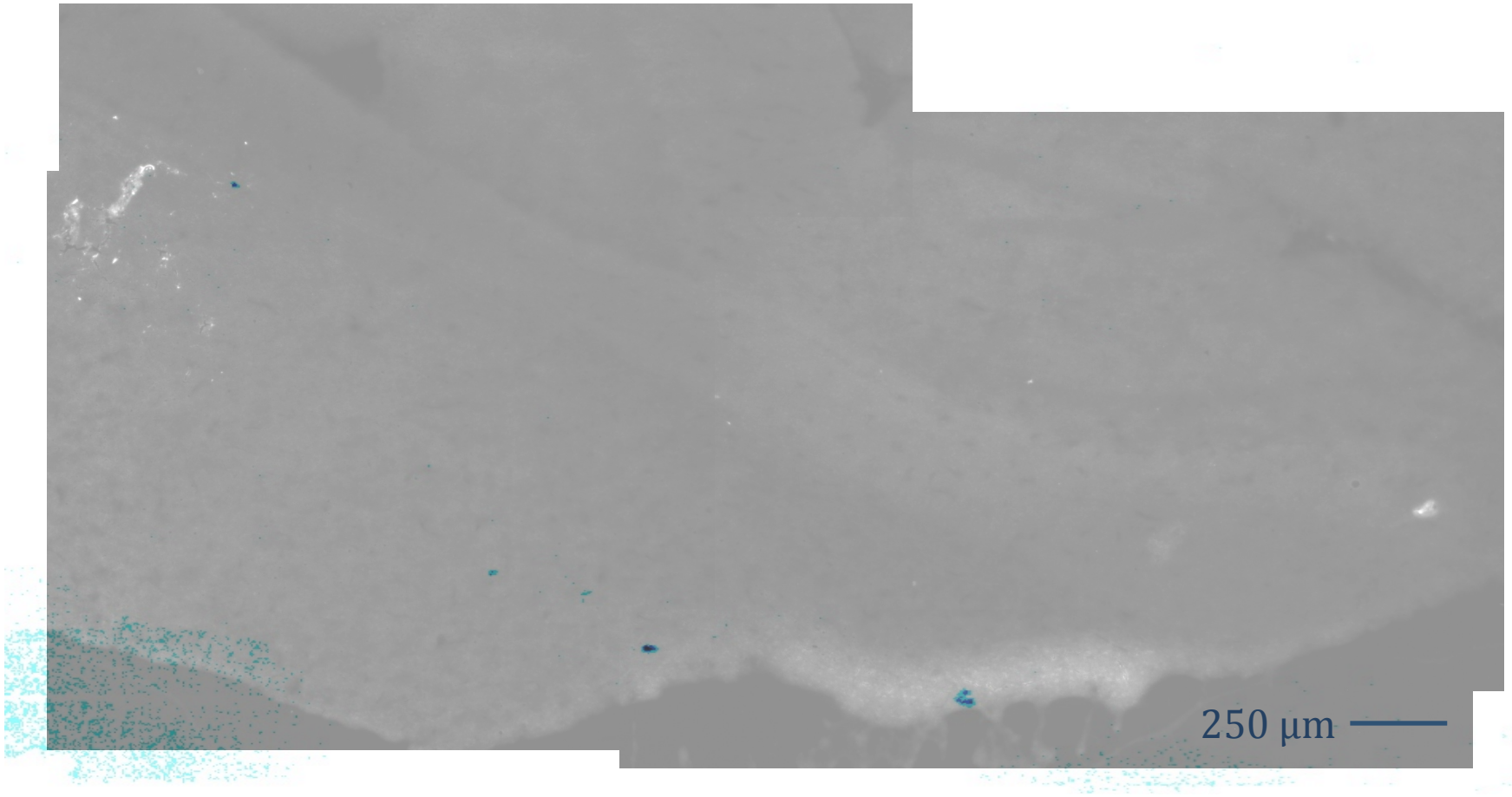

Figure 64: Overlay of Thioflavin T characteristic fragment 267 m/z mass spectrum image and fluorescent microscopy image. Distension is strongly evident between the two images, thus overlays were very difficult to attempt. Brunelle describes this same problem in his 2013 H&E paper where SIMS images and microscopic images could not be overlaid due to variability in the tissue structure.[104]

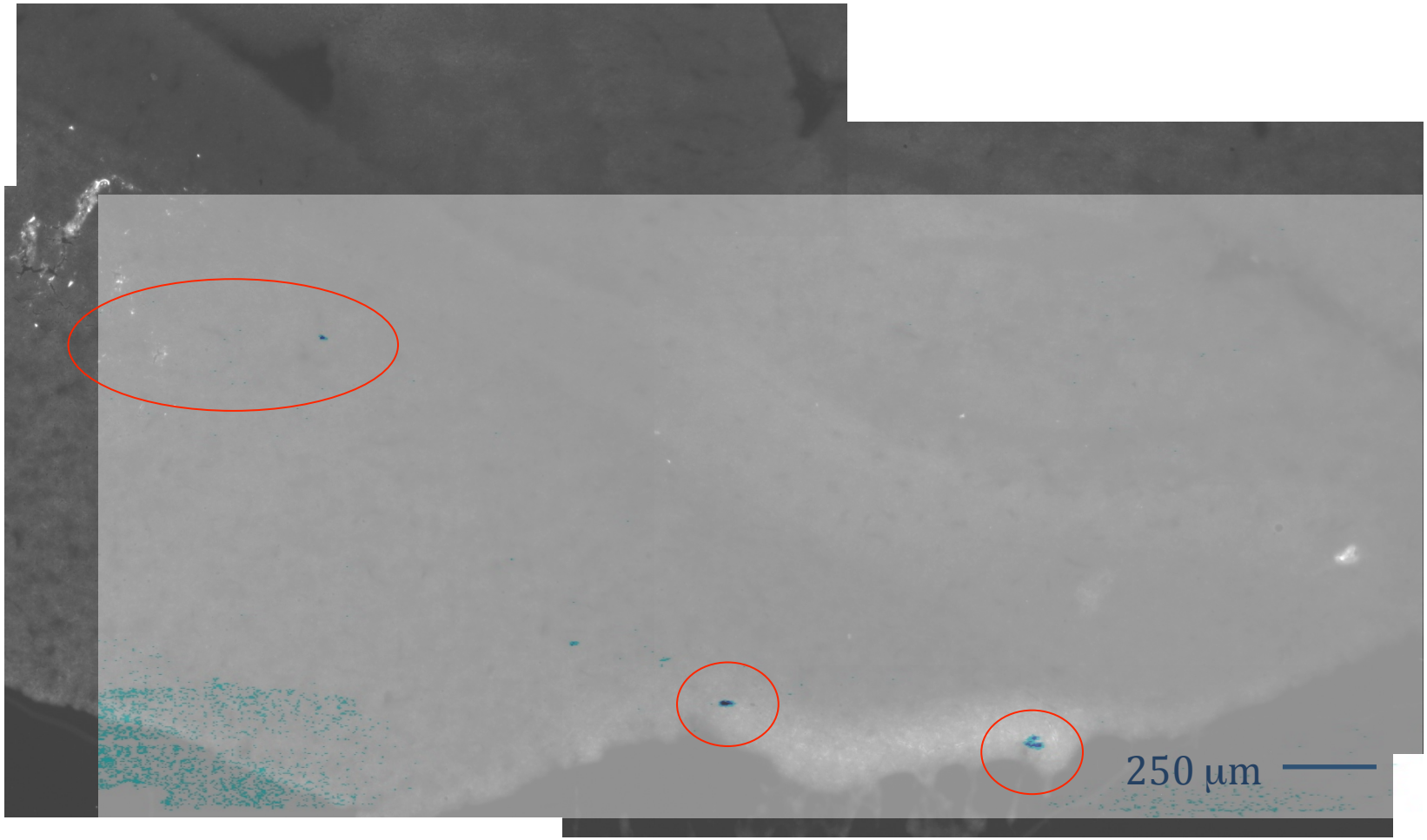

Figure 65: Adjusted overlay of Thioflavin T characteristic fragment 267 m/z mass spectrum image and fluorescent microscopy image. Images were stretched to align the likely areas of fluorescent intensity with secondary ion intensity. Even this process failed to align the intensity areas at the top right.

Figure 61 & Figure 62 depict areas of high secondary ion intensity in the isocortex for the characteristic fragments for Thioflavin T, which range in size from 20 μm to 50 μm. Both the size and location of the amyloid plaques correspond with expectations. The three negative controls (Figure 48, Figure 51, and Figure 59) were analysed along with the experiment for ions with a mass-to-charge ratio of 267 m/z to determine whether the areas of high intensity were artifacts of the stain or the tissue.

Figure 45, a wild-type image prior to staining, demonstrates that no other ion is found in high quantities in an unstained healthy tissue. Figure 51, a wild-type image after staining, illustrates that in a stained healthy tissue the stain wash removes the majority of Thioflavin T molecules, leaving only a slight background,. Finally, Figure 59, a transgenic image prior to staining, argues that this particular tissue has no other ions in high concentrations with a mass-to-charge ratio of 267 m/z before staining. Thus, these areas with high concentrations of Thioflavin T secondary ions (mass-to-charge ratio of 267 m/z) are most likely due to the binding of Thioflavin T to amyloid-beta plaques.

The fluorescent images support the hypothesis that these areas of intensity are in fact fluorescent Thioflavin T. While the distension in the tissue prevents a perfect overlay (Figure 64), if the images are stretched and reduced to account for the distension, the areas of high intensity in the two images correlate better (Figure 65). When the fluorescent images from the wild-type tissue (Figure 53) and transgenic tissue are compared (Figure 63), the splotches of fluorescent intensity of the Thioflavin T are abundant in the transgenic tissue indicating the presence of amyloid-beta plaques, and these intensities are not seen in the wild-type tissue. So

while the overlay of the two images is difficult, there clearly are areas of fluorescent and Thioflavin T secondary ions intensities found in the transgenic tissue that are absent in the wild-type tissue.

The introduction to this chapter discussed an article by the Johansson group that demonstrated co-locations of amyloid aggregates and cholesterol clusters in 18-24 month triple transgenic mice samples. This co-location is not seen in 15-month triple transgenic mice. Despite using the same technique to determine the location of the cholesterol deposits, the two findings are disparate. The cholesterol distribution for the transgenic mouse (Figure 46 & Figure 47) is more comparable to the cholesterol distribution of the wild-type mouse samples (Figure 57 & Figure 58) than to the cholesterol distribution described by the Johansson group (Figure 34).

Finally, the ToF-SIMS images support the hypothesis that the ethanol washes remove lipids from the tissue samples. This can be seen when Figure 54 and Figure 60 are compared or when Figure 43 and Figure 50 are compared. These images of the total ion count (TIC) show a drastic reduction in white matter intensity after staining has occurred. While lipids appear to have been removed, there does not appear to be any major structural damage to the integrity of the tissue when pre- and post-stained tissue images are compared.

7.4 Tissue Analysis Conclusions

The struggle to compare the results from the ToF-SIMS analysis and fluorescent imaging supports the purpose of this dissertation, as distension and struggle adjusting overlays would not occur if the amyloid plaques were able to be detected only using ToF-SIMS. The disparate pressure conditions used in each technique account for the challenge to overlay the two results: during ToF-SIMS, the tissue is under a high-pressure vacuum, but during fluorescent imaging it is under atmospheric pressure which can cause stretching and shrinking. Additionally, the fluorescent light of the microscope can become quite hot, further dehydrating and shrinking the tissue. Thus, as Brunelle states in his 2013 paper, the method of overlaying microscopy images and ToF-SIMS images is quite flawed.[104]

Another disadvantage when comparing fluorescent microscopic images with ToF-SIMS images is the issue of depth of view for each image. ToF-SIMS provides data only from the very top layer of the tissue, but microscopy provides a depth of view as thick as the sample. This is evident in Figure 63 where many splotches of fluorescent intensities can be seen on the left side of the image, but these do not appear in the ToF-SIMS analysis. It is likely that these aggregates are below the surface, in deeper parts of the 8 μm thick tissue section. Thus when microscopic images and ToF-SIMS images are compared, they do not produce identical results because microscopy images add an additional depth that is not present in ToF-SIMS images.

The case must then be made for comparing two ToF-SIMS images. In the protocol put forward in this dissertation, the tissue samples are imaged under high

vacuum, stained under atmospheric pressure with ethanol that washed away many of the lipids, and finally placed back into the high vacuum and imaged once more. The question becomes: Can the images prior to and after staining and washing be overlaid accurately? Figure 66 demonstrates that these two images are in fact quite aligned and could be easily overlaid. The same tile from each image was pulled out to demonstrate that, even though lipids have been washed away during the staining, the structure and form of the tissue remains very good. Thus the method laid out within this dissertation is a viable and not compromised by distension and variations in depth of view.

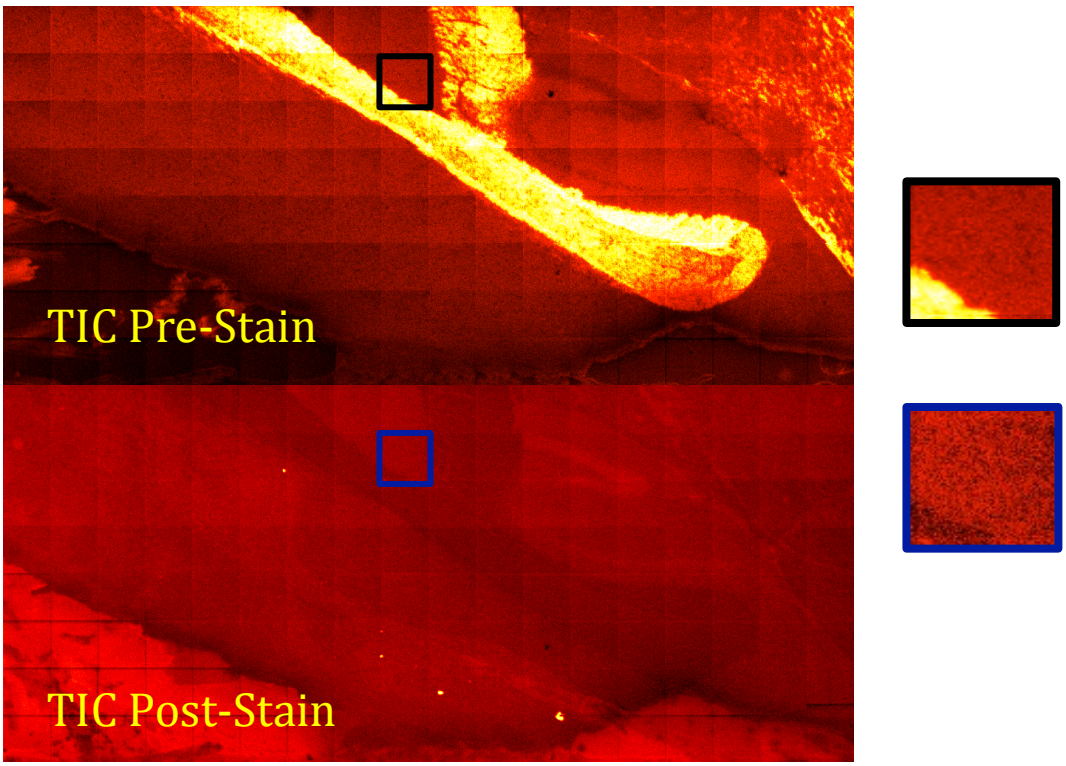

Figure 66: Comparison of pre- and post- stained images demonstrating the consistent alignment even after washings under atmospheric pressure. A tile from the same location was blown up on the right, demonstrating the structure and form of the tissue to be consistent.

After determining the location of the aggregates, the mass spectra from the pre- and post-stained tissues can be analysed to determine if there exist noticeable

differences between areas with and without plaques. Figure 67 compares the TIC mass spectra between a tile with an aggregate and a control tile, using the pre-stained sample. The spectra are aligned so that any ions present in one but not the other can be easily identified. Interestingly, these spectra appear to be mirror images of each other. This lack of difference could imply that the fragments of the amyloid-beta plaques are still too large for detection. Further, perhaps the local chemistry surrounding the plaques is not substantially different from the chemistry of the rest of the unaffected isocortex.

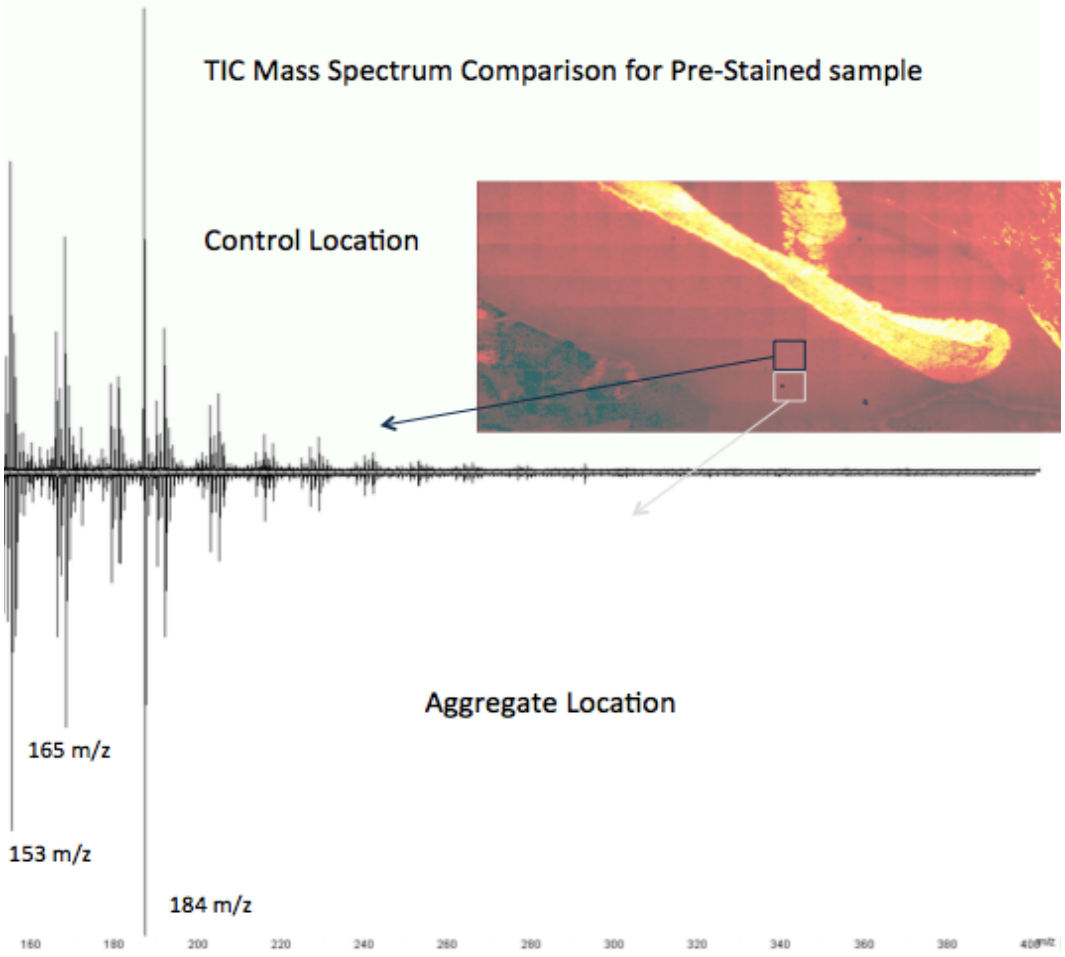

Figure 67: Comparison of pre-stained ToF-SIMS TIC Spectrum for aggregate and control tiles. Image on the top right is the TIC image of the pre-stained tissue. The location of the amyloid plaques is overlaid onto the image to illustrate that the aggregate tile does indeed have aggregates present.

The same comparison can be made for the post-stain sample (Figure 68). Once again, no new ions appear when the aggregate and control tiles are compared. However, as expected, there are larger peaks for 267 m/z and 283 m/z ions because these ions are found in much greater concentration in the aggregate tile since this is where the Thioflavin T bound to the amyloid aggregates.

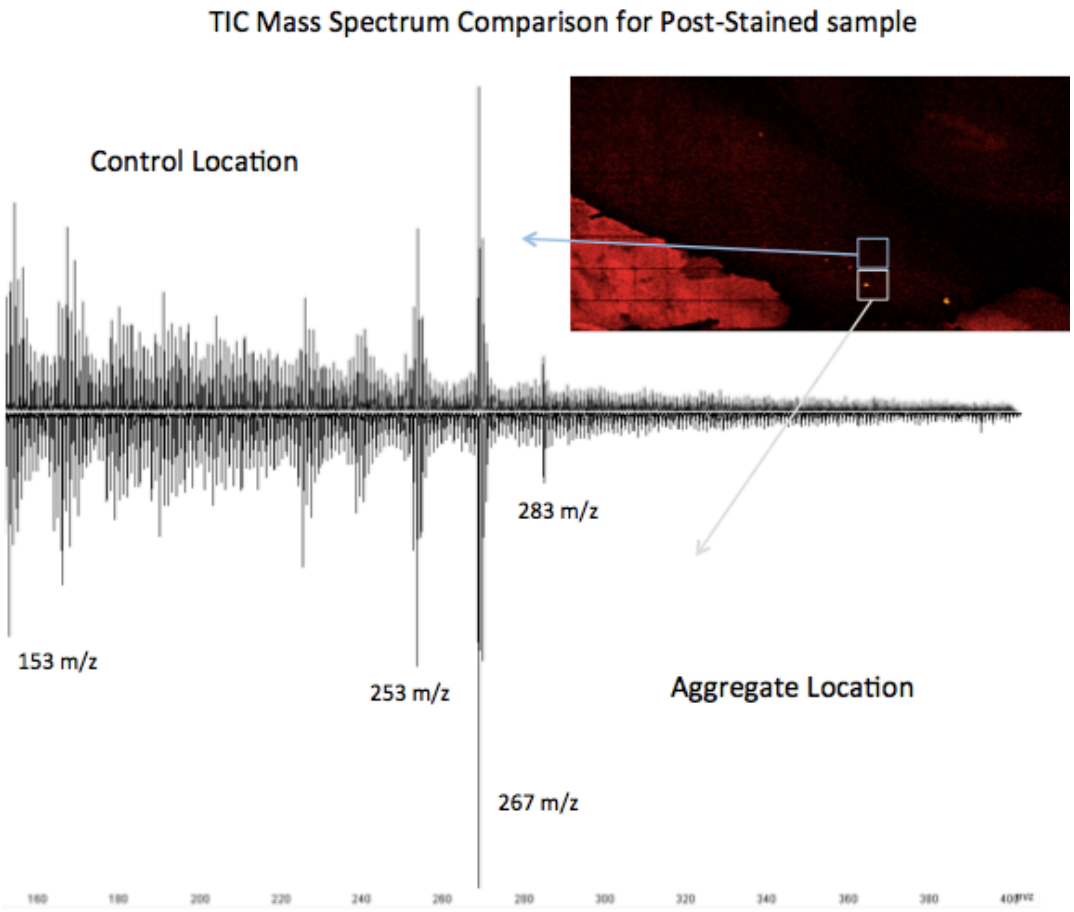

Figure 68: Comparison of post-stained ToF-SIMS TIC Spectrum for an aggregate tile and a control tile. Image on the top right is the TIC image of the post-stained tissue. While there are no new ions present, the aggregate tile has greater counts for 267 m/z and 283 m/z ions.

Another interesting finding when comparing the images and the spectra is the lack of cholesterol surrounding the aggregates (Figure 67 & Figure 69). The spectrum in Figure 67 shows no increased frequency in this region. When the images are compared side by side in Figure 69, no cholesterol deposits appear surrounding the plaques, despite the suggestions from the Johansson Group paper.[105]

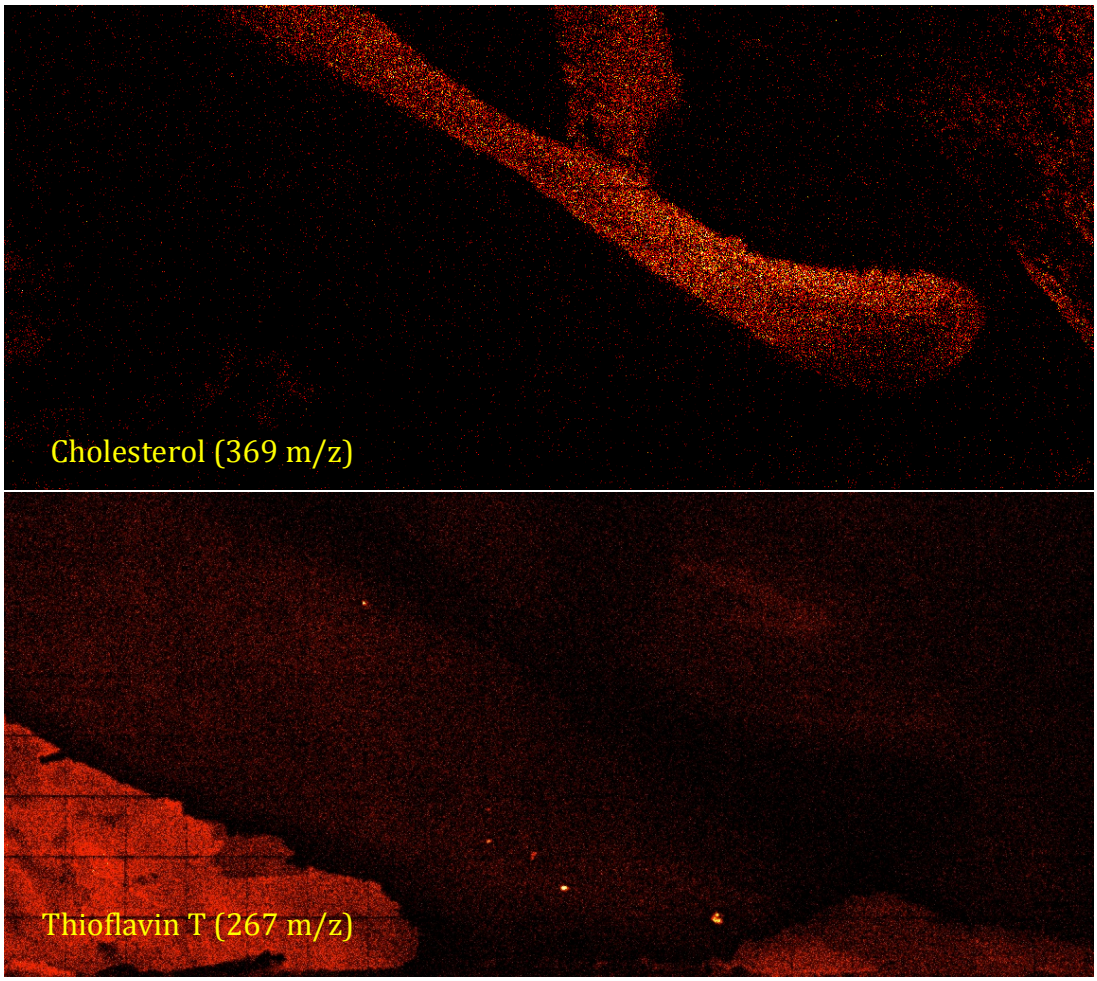

Figure 69: A pre-stained cholesterol image compared with a post-stained Thioflavin T image, illustrating that cholesterol deposits were not found around the plaques for 15 month old mice.

It could be that the high concentration of phosphonosphingolipids in this region of the isocortex (Figure 55 & Figure 56) suppresses the secondary ions produced by cholesterol. Yet if this is the case, then this same repression should have been seen in the paper by the Johansson Group since they also used ToF-SIMS to determine

the location of the cholesterol. Could it be that these cholesterol deposits are dependent on the age of the mice? The Johansson group used triple transgenic mice that were 18-24 months, while the triple transgenic mice used in these experiments were 15 months. Amyloid aggregates can be present in the human brain for 20 years prior to the symptoms of Alzheimer's disease. It is possible that the symptoms of the disease may occur only once these cholesterol deposits are present. This is of course wild speculation, but these are at least questions that future projects can investigate.

Another potential future project could look at the use of antibodies to identify particular proteins in tissue samples. If one could find a secondary antibody with a unique fragment, then one could identify any protein using this method. For such a project, the tissue would first be analysed, then a primary antibody would be used to bind to the protein of interest, followed by the addition of the unique secondary antibody to bind the primary antibody. The tissue would be analysed again and wherever the characteristic fragment for the secondary antibody is present, this would identify the location of the protein of interest. This would allow the detection of many different molecules and a unique stain would not have to be first identified.

This project presented a helpful protocol that hopefully will be used in this lab going forward. The ability to detect the amyloid-beta aggregates enables the study of metabolite and lipid co-localisations that might be present or absent in the diseased brain. This type of protocol could be used for many different proteins, amino acids, or even specific lipids, thus expanding the use of ToF-SIMS detection.

8. References

(1) Griffiths, J. A Brief History of Mass Spectrometry. *Anal. Chem.* **2008**, *80*, 5678–5683.

(2) Herzog, R. F. K.; Viehböck, F. P. Ion Source for Mass Spectrography. *Phys. Rev.* **1949**, *76*, 855–856.

(3) Liebl, H. Ion Microprobe Mass Analyzer. *Journal of Applied Physics* **1967**, *38*, 5277–5283.

(4) Vickerman, J. C. Prologue: TOF-SIMS – An Evolving Mass Spectrometry of Materials. In *TOF-SIMS: Materials Analysis by Mass Spectrometry*; 2nd Ed. Vickerman, J. C.; Briggs, D., Ed. SurfaceSpectra, Manchester and IM Publications: Chichester, 2013; pp 1-38.

(5) Benninghoven, A.; Loebach, E. Tandem Mass Spectrometer for Secondary Ion Studies. *Review of Scientific Instruments* **1971**, *42*, 49–52.

(6) Briggs, D.; Hearn, M. J. Sub-Micron Molecular Imaging. A Viability Study by Time-of-Flight SIMS. *Surf. Interface Anal.* **1988**, *13*, 181–185.

(7) Delcorte, A.; Garrison, B. J. Desorption of Large Organic Molecules Induced by keV Projectiles. *Nuclear Instruments and Methods in Physics Research Section B: Beam Interactions with Materials and Atoms* **2001**, *180*, 37–43.

(8) Davies, N.; Weibel, D. E.; Blenkinsopp, P.; Lockyer, N.; Hill, R.; Vickerman, J. C. Development and Experimental Application of a Gold Liquid Metal Ion Source. *Applied Surface Science* **2003**, *203–204*, 223–227.

(9) Wong, S. C. C.; Hill, R.; Blenkinsopp, P.; Lockyer, N. P.; Weibel, D. E.; Vickerman, J. C. Development of a C60+ Ion Gun for Static SIMS and Chemical Imaging. *Applied Surface Science* **2003**, *203–204*, 219–222.

(10) Yamada, I.; Matsuo, J.; Toyoda, N.; Kirkpatrick, A. Materials Processing by Gas Cluster Ion Beams. *Materials Science and Engineering: R: Reports* **2001**, *34*, 231–295.

(11) Rabbani, S.; Barber, A. M.; Fletcher, J. S.; Lockyer, N. P.; Vickerman, J. C. TOF-SIMS with Argon Gas Cluster Ion Beams: A Comparison with C60+. *Anal. Chem.* **2011**, *83*, 3793–3800.

(12) Sheraz née Rabbani, S.; Barber, A.; Fletcher, J. S.; Lockyer, N. P.; Vickerman, J. C. Enhancing Secondary Ion Yields in Time of Flight-Secondary Ion Mass Spectrometry Using Water Cluster Primary Beams. *Anal. Chem.* **2013**, *85*, 5654–5658.

(13) Fletcher, J. S.; Szakal, C. Cluster and Polyatomic Primary Ion Beam. In *TOF-SIMS: Materials Analysis by Mass Spectrometry*; 2nd Ed. Vickerman, J. C.; Briggs, D., Ed. SurfaceSpectra, Manchester and IM Publications: Chichester, 2013; pp 291-310.

(14) Fletcher, J. S.; Rabbani, S.; Henderson, A.; Blenkinsopp, P.; Thompson, S. P.; Lockyer, N. P.; Vickerman, J. C. A New Dynamic in Mass Spectral Imaging of Single Biological Cells. *Anal. Chem.* **2008**, *80*, 9058–9064.

(15) Fletcher, J. S.; Rabbani, S.; Henderson, A.; Lockyer, N. P.; Vickerman, J. C. Three-Dimensional Mass Spectral Imaging of HeLa-M Cells – Sample Preparation, Data Interpretation and Visualisation. *Rapid Commun. Mass Spectrom.* **2011**, *25*, 925–932.

(16) Rabbani, S.; Fletcher, J. S.; Lockyer, N. P.; Vickerman, J. C. Exploring Subcellular Imaging on the Buncher-ToF J105 3D Chemical Imager. *Surf. Interface Anal.* **2011**, *43*, 380–384.

(17) Piwowar, A.M.; Winograd, N. Application of SIMS to Study of Biological Systems. In *TOF-SIMS: Materials Analysis by Mass Spectrometry*; 2nd Ed. Vickerman, J. C.; Briggs, D., Ed. SurfaceSpectra, Manchester and IM Publications: Chichester, 2013; pp 553-582.

(18) Fletcher, J. S. Cellular Imaging with Secondary Ion Mass Spectrometry. *The Analyst* **2009**, *134*, 2204.

(19) Garrison, B. J.; Postawa, Z. Computational View of Surface Based Organic Mass Spectrometry. *Mass Spectrom. Rev.* **2008**, *27*, 289–315.

(20) Fletcher, J. S.; Lockyer, N. P.; Vickerman, J. C. C60, Buckminsterfullerene: Its Impact on Biological ToF-SIMS Analysis. *Surf. Interface Anal.* **2006**, *38*, 1393–1400.

(21) Hanrieder, J.; Malmberg, P.; Lindberg, O. R.; Fletcher, J. S.; Ewing, A. G. Time-of-Flight Secondary Ion Mass Spectrometry Based Molecular Histology of Human Spinal Cord Tissue and Motor Neurons. *Anal. Chem.* **2013**, *85*, 8741–8748.

(22) Frisz, J. F.; Choi, J. S.; Wilson, R. L.; Harley, B. A. C.; Kraft, M. L. Identifying Differentiation Stage of Individual Primary Hematopoietic Cells from Mouse Bone Marrow by Multivariate Analysis of TOF-Secondary Ion Mass Spectrometry Data. *Anal. Chem.* **2012**, *84*, 4307–4313.

(23) Jerigova, M.; Biro, C.; Kirchnerova, J.; Chorvatova, A.; Jr, D. C.; Lorenc, D.; Velic, D. Chemical Imaging of Cardiac Cell and Tissue by Using Secondary Ion Mass Spectrometry. *Mol Imaging Biol* **2011**, *13*, 1067–1076.

(24) Saito, K.; Watanabe, Y.; Shirakawa, M.; Matsushita, Y.; Imai, T.; Koike, T.; Sano, Y.; Funada, R.; Fukazawa, K.; Fukushima, K. Direct Mapping of Morphological Distribution of Syringyl and Guaiacyl Lignin in the Xylem of Maple by Time-of-Flight Secondary Ion Mass Spectrometry. *The Plant Journal* **2012**, *69*, 542–552.

(25) Cillero-Pastor, B.; Eijkel, G.; Kiss, A.; Blanco, F. J.; Heeren, R. M. A. Time-of-Flight Secondary Ion Mass Spectrometry-Based Molecular Distribution Distinguishing Healthy and Osteoarthritic Human Cartilage. *Anal. Chem.* **2012**, *84*, 8909–8916.

(26) Seyer, A.; Cantiello, M.; Bertrand-Michel, J.; Roques, V.; Nauze, M.; Bézirard, V.; Collet, X.; Touboul, D.; Brunelle, A.; Coméra, C. Lipidomic and Spatio-Temporal Imaging of Fat by Mass Spectrometry in Mice Duodenum during Lipid Digestion. *PLoS ONE* **2013**, *8*, e58224.

(27) Kotze, H. L.; Armitage, E. G.; Fletcher, J. S.; Henderson, A.; Williams, K. J.; Lockyer, N. P.; Vickerman, J. C. ToF-SIMS as a Tool for Metabolic Profiling

Small Biomolecules in Cancer Systems. *Surf. Interface Anal.* **2013**, *45*, 277–281.

(28) Passarelli, M. K.; Winograd, N. Lipid Imaging with Time-of-Flight Secondary Ion Mass Spectrometry (ToF-SIMS). *Biochim Biophys Acta* **2011**, *1811*, 976–990.

(29) Börner, K.; Nygren, H.; Hagenhoff, B.; Malmberg, P.; Tallarek, E.; Månsson, J.-E. Distribution of Cholesterol and Galactosylceramide in Rat Cerebellar White Matter. *Biochim. Biophys. Acta* **2006**, *1761*, 335–344.

(30) Sjövall, P.; Lausmaa, J.; Johansson, B. Mass Spectrometric Imaging of Lipids in Brain Tissue. *Anal. Chem.* **2004**, *76*, 4271–4278.

(31) Fletcher, J. S.; Lockyer, N. P.; Vickerman, J. C. Molecular SIMS Imaging; Spatial Resolution and Molecular Sensitivity: Have We Reached the End of the Road? Is There Light at the End of the Tunnel? *Surf. Interface Anal.* **2011**, *43*, 253–256.

(32) Kurczy, M. E.; Piehowski, P. D.; Van Bell, C. T.; Heien, M. L.; Winograd, N.; Ewing, A. G. Mass Spectrometry Imaging of Mating Tetrahymena Show That Changes in Cell Morphology Regulate Lipid Domain Formation. *Proc. Natl. Acad. Sci. U.S.A.* **2010**, *107*, 2751–2756.

(33) Yang, H.-J.; Ishizaki, I.; Sanada, N.; Zaima, N.; Sugiura, Y.; Yao, I.; Ikegami, K.; Setou, M. Detection of Characteristic Distributions of Phospholipid Head Groups and Fatty Acids on Neurite Surface by Time-of-Flight Secondary Ion Mass Spectrometry. *Med Mol Morphol* **2010**, *43*, 158–164.

(34) Brown, H.A. *Lipidomics and Bioactive Lipids: Mass Spectrometry Based Lipid Analysis: Mass Spectrometry Based Lipid Analysis*; Academic Press: Waltham, Massachusetts, 2007.

(35) Appelhans, A. D.; Dahl, D. A.; Delmore, J. E. Neutralization of Sample Charging in Secondary Ion Mass Spectrometry via a Pulsed Extraction Field. *Anal. Chem.* **1990**, *62*, 1679–1686.

(36) Aoyagi, S.; Fletcher, J. S.; (Rabbani), S. S.; Kawashima, T.; Razo, I. B.; Henderson, A.; Lockyer, N. P.; Vickerman, J. C. Peptide Structural Analysis

Using Continuous Ar Cluster and C60 Ion Beams. *Anal Bioanal Chem* **2013**, *405*, 6621–6628.

(37) Mahoney, C. M.; Fahey, A. J.; Belu, A. M. Three-Dimensional Compositional Analysis of Drug Eluting Stent Coatings Using Cluster Secondary Ion Mass Spectrometry. *Anal. Chem.* **2008**, *80*, 624–632.

(38) Goacher, R. E.; Jeremic, D.; Master, E. R. Expanding the Library of Secondary Ions That Distinguish Lignin and Polysaccharides in Time-of-Flight Secondary Ion Mass Spectrometry Analysis of Wood. *Anal. Chem.* **2011**, *83*, 804–812.

(39) Benninghoven, A. *Secondary Ion Mass Spectrometry: SIMS VI : Proceedings of the Sixth International Conference on Secondary Ion Mass Spectrometry (SIMS VI), Palais Des Congrès, Versailles, Paris, France, September 13-18th, 1987*; Wiley, 1988.

(40) Sichtermann, W.; Benninghoven, A. Secondary Ion Formation from Amino Acids by Proton and Cation Transfer. *International Journal of Mass Spectrometry and Ion Physics* **1981**, *40*, 177–184.

(41) Briggs, D.; Hearn, M. Interaction of Ion Beams with Polymers, with Particular Reference to SIMS. *Vacuum* **1986**, *36*, 1005–1010.

(42) Cheng, J.; Winograd, N. Depth Profiling of Peptide Films with TOF-SIMS and a C60 Probe. *Anal. Chem.* **2005**, *77*, 3651–3659.

(43) Jones, E. A.; Lockyer, N. P.; Vickerman, J. C. Mass Spectral Analysis and Imaging of Tissue by ToF-SIMS—The Role of Buckminsterfullerene, C60+, Primary Ions. *International Journal of Mass Spectrometry* **2007**, *260*, 146–157.

(44) Nygren, H.; Börner, K.; Malmberg, P.; Hagenhoff, B. Localization of Cholesterol in Rat Cerebellum with Imaging TOF-SIMS: Effect of Tissue Preparation. *Applied Surface Science* **2006**, *252*, 6975–6981.

(45) Fletcher, J. S.; Rabbani, S.; Barber, A. M.; Lockyer, N. P.; Vickerman, J. C. Comparison of C60 and GCIB Primary Ion Beams for the Analysis of Cancer Cells and Tumour Sections. *Surf. Interface Anal.* **2013**, *45*, 273–276.

(46) Amaya, K. R.; Monroe, E. B.; Sweedler, J. V.; Clayton, D. F. Lipid Imaging in the Zebra Finch Brain with Secondary Ion Mass Spectrometry. *International Journal of Mass Spectrometry* **2007**, *260*, 121–127.

(47) Chandra, S.; Barth, R. F.; Haider, S. A.; Yang, W.; Huo, T.; Shaikh, A. L.; Kabalka, G. W. Biodistribution and Subcellular Localization of an Unnatural Boron-Containing Amino Acid (Cis-ABCPC) by Imaging Secondary Ion Mass Spectrometry for Neutron Capture Therapy of Melanomas and Gliomas. *PLoS ONE* **2013**, *8*, e75377.

(48) Candy, J. M.; Oakley, A. E.; Mountfort, S. A.; Taylor, G. A.; Morris, C. M.; Bishop, H. E.; Edwardson, J. A. The Imaging and Quantification of Aluminium in the Human Brain Using Dynamic Secondary Ion Mass Spectrometry (SIMS). *Biology of the Cell* **1992**, *74*, 109–118.

(49) Lazar, A. N.; Bich, C.; Panchal, M.; Desbenoit, N.; Petit, V. W.; Touboul, D.; Dauphinot, L.; Marquer, C.; Laprévote, O.; Brunelle, A.; et al. Time-of-Flight Secondary Ion Mass Spectrometry (TOF-SIMS) Imaging Reveals Cholesterol Overload in the Cerebral Cortex of Alzheimer Disease Patients. *Acta Neuropathol* **2013**, *125*, 133–144.

(50) Matsuzaki, T.; Sasaki, K.; Hata, J.; Hirakawa, Y.; Fujimi, K.; Ninomiya, T.; Suzuki, S. O.; Kanba, S.; Kiyohara, Y.; Iwaki, T. Association of Alzheimer Disease Pathology with Abnormal Lipid Metabolism: The Hisayama Study. *Neurology September 13, 2011* **2011**, *77*, 1068–1075.

(51) Tofoleanu, F.; Buchete, N.-V. Molecular Interactions of Alzheimer's Aβ Protofilaments with Lipid Membranes. *Journal of Molecular Biology* **2012**, *421*, 572–586.

(52) Yu, X.; Zheng, J. Cholesterol Promotes the Interaction of Alzheimer B-Amyloid Monomer with Lipid Bilayer. *Journal of Molecular Biology* **2012**, *421*, 561–571.

(53) McKhann, G.; Drachman, D.; Folstein, M. Clinical Diagnosis of Alzheimer's Disease: Report of the NINCDS-ADRDA Work Group under the Auspices of

Department of Health and Human Services Task Force on Alzheimer's Disease. *Neurology* **1984**, *34*, 939–944.

(54) Hebert, L. E.; Weuve, J.; Scherr, P. A.; Evans, D. A. Alzheimer Disease in the United States (2010-2050) Estimated Using the 2010 Census. *Neurology* **2013**, *80*, 1778–1783.

(55) Dajani, S. Dementia 2013 infographic http://alzheimers.org.uk/infographic (accessed May 7, 2014).

(56) Alzheimer's Disease International. *World Alzheimer Report 2009*. http://www.alz.co.uk/research/files/WorldAlzheimerReport.pdf (accessed May 7, 2014).

(57) Alzheimer's Association. *Early Diagnosis: The Value of Knowing. http://www.alz.org/mnnd/documents/10signs_physicanfactsheet_final.pdf* (accessed May 7, 2014).

(58) Feldman, H. H.; Woodward, M. The Staging and Assessment of Moderate to Severe Alzheimer Disease. *Neurology* **2005**, *65*, S10–S17.

(59) Blennow, K.; de Leon, M. J.; Zetterberg, H. Alzheimer's Disease. *The Lancet* **2006**, *368*, 387–403.

(60) Sperling, R. A.; Aisen, P. S.; Beckett, L. A.; Bennett, D. A.; Craft, S.; Fagan, A. M.; Iwatsubo, T.; Jack Jr., C. R.; Kaye, J.; Montine, T. J.; et al. Toward Defining the Preclinical Stages of Alzheimer's Disease: Recommendations from the National Institute on Aging-Alzheimer's Association Workgroups on Diagnostic Guidelines for Alzheimer's Disease. *Alzheimer's & Dementia* **2011**, *7*, 280–292.

(61) Davies, L.; Wolska, B.; Hilbich, C.; Multhaup, G.; Martins, R.; Simms, G.; Beyreuther, K.; Masters, C. L. A4 Amyloid Protein Deposition and the Diagnosis of Alzheimer's Disease: Prevalence in Aged Brains Determined by Immunocytochemistry Compared with Conventional Neuropathologic Techniques. *Neurology* **1988**, *38*, 1688–1693.

(62) Braak, E.; Griffing, K.; Arai, K.; Bohl, J.; Bratzke, H.; Braak, H. Neuropathology of Alzheimer's Disease: What Is New since A. Alzheimer?

European Archives of Psychiatry and Clinical Neurosciences **1999**, *249*, S14–S22.

(63) Burns, A.; Iliffe, S. Alzheimer's Disease. *BMJ* **2009**, *338*, b158–b158.

(64) Iqbal, K.; Del C. Alonso, A.; Chen, S.; Chohan, M. O.; El-Akkad, E.; Gong, C.-X.; Khatoon, S.; Li, B.; Liu, F.; Rahman, A.; et al. Tau Pathology in Alzheimer Disease and Other Tauopathies. *Biochimica et Biophysica Acta - Molecular Basis of Disease* **2005**, *1739*, 198–210.

(65) Todd, S.; Barr, S.; Passmore, A. P. Cause of Death in Alzheimer's Disease: A Cohort Study. *QJM* **2013**, *106*, 747–753.

(66) Fox, N. C.; Schott, J. M. Imaging Cerebral Atrophy: Normal Ageing to Alzheimer's Disease. *The Lancet* **2004**, *363*, 392–394.

(67) Jost, B. C.; Grossberg, G. T. The Natural History of Alzheimer's Disease: A Brain Bank Study. *J Am Geriatr Soc* **1995**, *43*, 1248–1255.

(68) Robertson, P. Wellington Boone/Meredith Parker. *The 700 Club.* Sept 13, **2011**.

(69) Alzheimer, A. About a Peculiar Disease of the Cerebral Cortex. By Alois Alzheimer, 1907 (Translated by L. Jarvik and H. Greenson). *Alzheimer Dis Assoc Disord* **1987**, *1*, 3–8.

(70) Hardy, J.; Selkoe, D. J. The Amyloid Hypothesis of Alzheimer's Disease: Progress and Problems on the Road to Therapeutics. *Science* **2002**, *297*, 353–356.

(71) Masters, C. L.; Simms, G.; Weinman, N. A.; Multhaup, G.; McDonald, B. L.; Beyreuther, K. Amyloid Plaque Core Protein in Alzheimer Disease and Down Syndrome. *PNAS* **1985**, *82*, 4245–4249.

(72) Jarrett, J. T.; Berger, E. P.; Lansbury, P. T. The Carboxy Terminus of the .beta. Amyloid Protein Is Critical for the Seeding of Amyloid Formation: Implications for the Pathogenesis of Alzheimer's Disease. *Biochemistry* **1993**, *32*, 4693–4697.

(73) Priller, C.; Bauer, T.; Mitteregger, G.; Krebs, B.; Kretzschmar, H. A.; Herms, J. Synapse Formation and Function Is Modulated by the Amyloid Precursor Protein. *J. Neurosci.* **2006**, *26*, 7212–7221.

(74) Turner, P. R.; O'Connor, K.; Tate, W. P.; Abraham, W. C. Roles of Amyloid Precursor Protein and Its Fragments in Regulating Neural Activity, Plasticity and Memory. *Progress in Neurobiology* **2003**, *70*, 1–32.

(75) Kumar, S.; Rezaei-Ghaleh, N.; Terwel, D.; Thal, D. R.; Richard, M.; Hoch, M.; Donald, J. M. M.; Wüllner, U.; Glebov, K.; Heneka, M. T.; et al. Extracellular Phosphorylation of the Amyloid B-peptide Promotes Formation of Toxic Aggregates during the Pathogenesis of Alzheimer's Disease. *The EMBO Journal* **2011**, *30*, 2255–2265.

(76) Feki, A.; Teboul, O.; Dubois, A.; Bozon, B.; Faure, A.; Hantraye, P.; Dhenain, M.; Delatour, B.; Delzescaux, T. Fully Automated and Adaptive Detection of Amyloid Plaques in Stained Brain Sections of Alzheimer Transgenic Mice. *Med Image Comput Comput Assist Interv* **2007**, *10*, 960–968.

(77) Walsh, D. M.; Selkoe, D. J. Deciphering the Molecular Basis of Memory Failure in Alzheimer's Disease. *Neuron* **2004**, *44*, 181–193.

(78) Carson, J. A.; Turner, A. J. B-Amyloid Catabolism: Roles for Neprilysin (NEP) and Other Metallopeptidases? *Journal of Neurochemistry* **2002**, *81*, 1–8.

(79) Tanzi, R. E.; Moir, R. D.; Wagner, S. L. Clearance of Alzheimer's Aβ Peptide: The Many Roads to Perdition. *Neuron* **2004**, *43*, 605–608.

(80) Rovelet-Lecrux, A.; Hannequin, D.; Raux, G.; Meur, N. L.; Laquerrière, A.; Vital, A.; Dumanchin, C.; Feuillette, S.; Brice, A.; Vercelletto, M.; et al. APP Locus Duplication Causes Autosomal Dominant Early-Onset Alzheimer Disease with Cerebral Amyloid Angiopathy. *Nat Genet* **2006**, *38*, 24–26.

(81) Joachim, C. L.; Morris, J. H.; Selkoe, D. J. Clinically Diagnosed Alzheimer's Disease: Autopsy Results in 150 Cases. *Ann Neurol.* **1988**, *24*, 50–56.

(82) Wood, A. E.; Ellis, R. C. *Laboratory Histopathology : A Complete Reference*; Churchill Livingstone: Edinburgh, 1994.

(83) Maezawa, I.; Hong, H.-S.; Liu, R.; Wu, C.-Y.; Cheng, R. H.; Kung, M.-P.; Kung, H. F.; Lam, K. S.; Oddo, S.; LaFerla, F. M.; et al. Congo Red and

Thioflavin-T Analogs Detect Aβ Oligomers. *Journal of Neurochemistry* **2008**, *104*, 457–468.

(84) Qin, L.; Vastl, J.; Gao, J. Highly Sensitive Amyloid Detection Enabled by Thioflavin T Dimers. *Mol. BioSyst.* **2010**, *6*, 1791–1795.

(85) Wolfe, L. S.; Calabrese, M. F.; Nath, A.; Blaho, D. V.; Miranker, A. D.; Xiong, Y. Protein-Induced Photophysical Changes to the Amyloid Indicator Dye Thioflavin T. *Proc Natl Acad Sci U S A* **2010**, *107*, 16863–16868.

(86) Kuznetsova, I. M.; Sulatskaya, A. I.; Uversky, V. N.; Turoverov, K. K. Analyzing Thioflavin T Binding to Amyloid Fibrils by an Equilibrium Microdialysis-Based Technique. *PLoS ONE* **2012**, *7*, e30724.

(87) Hudson, S. A.; Ecroyd, H.; Kee, T. W.; Carver, J. A. The Thioflavin T Fluorescence Assay for Amyloid Fibril Detection Can Be Biased by the Presence of Exogenous Compounds. *FEBS J.* **2009**, *276*, 5960–5972.

(88) Rodríguez-Rodríguez, C.; Rimola, A.; Rodríguez-Santiago, L.; Ugliengo, P.; Álvarez-Larena, Á.; Gutiérrez-de-Terán, H.; Sodupe, M.; González-Duarte, P. Crystal Structure of Thioflavin-T and Its Binding to Amyloid Fibrils: Insights at the Molecular Level. *Chem. Commun.* **2010**, *46*, 1156–1158.

(89) Krebs, M. R. H.; Bromley, E. H. C.; Donald, A. M. The Binding of Thioflavin-T to Amyloid Fibrils: Localisation and Implications. *Journal of Structural Biology* **2005**, *149*, 30–37.

(90) Groenning, M. Binding Mode of Thioflavin T and Other Molecular Probes in the Context of Amyloid Fibrils--Current Status. *J Chem Biol* **2009**, *3*, 1–18.

(91) Ramakrishnan, M.; Kandimalla, K. K.; Wengenack, T. M.; Howell, K. G.; Poduslo, J. F. Surface Plasmon Resonance Binding Kinetics of Alzheimer's Disease Amyloid ? Peptide Capturing- and Plaque Binding- Monoclonal Antibodies. *Biochemistry* **2009**, *48*, 10405–10415.

(92) Shard, A. G.; Brewer, P. J.; Green, F. M.; Gilmore, I. S. Measurement of Sputtering Yields and Damage in C60 SIMS Depth Profiling of Model Organic Materials. *Surf. Interface Anal.* **2007**, *39*, 294–298.

(93) Shard, A. G.; Ray, S.; Seah, M. P.; Yang, L. VAMAS Interlaboratory Study on Organic Depth Profiling. *Surf. Interface Anal.* **2011**, *43*, 1240–1250.

(94) Shard, A. G.; Green, F. M.; Brewer, P. J.; Seah, M. P.; Gilmore, I. S. Quantitative Molecular Depth Profiling of Organic Delta-Layers by C60 Ion Sputtering and SIMS. *J Phys Chem B* **2008**, *112*, 2596–2605.

(95) Block, C.; Wynants, L.; Kelchtermans, M.; De Boer, R.; Compernolle, F. Identification of Polymer Additives by Liquid Chromatography–mass Spectrometry. *Polymer Degradation and Stability* **2006**, *91*, 3163–3173.

(96) ChemDoodle. ChemDoddle Web Components: 2D Sketcher. http://web.chemdoodle.com/demos/sketcher (accessed May 7, 2014).

(97) Zhou, A.; Carrell, R. W.; Murphy, M. P.; Wei, Z.; Yan, Y.; Stanley, P. L. D.; Stein, P. E.; Broughton Pipkin, F.; Read, R. J. A Redox Switch in Angiotensinogen Modulates Angiotensin Release. *Nature* **2010**, *468*, 108–111.

(98) Junqueira, L. C. U.; Carneiro, J. *Basic Histology: Text & Atlas*; McGraw-Hill, Medical Pub. Division: New York, 2005.

(99) Divry, P.; Bobon, J.; Collard, J.; Pinchard, A.; Nols, E. Study & clinical trial of R 1625 or haloperidol, a new neuroleptic & so-called neurodysleptic agent. *Acta Neurol Psychiatr Belg* **1959**, *59*, 337–366.

(100) Johansson, T.; Weidolf, L.; Popp, F.; Tacke, R.; Jurva, U. In Vitro Metabolism of Haloperidol and Sila-Haloperidol: New Metabolic Pathways Resulting from Carbon/Silicon Exchange. *Drug Metab Dispos* **2010**, *38*, 73–83.

(101) Giotto High Technology. Nanocalc: Optical characterization of thin films. http://www.ghtphotonics.com/wp/2012/10/17/nanocalc/ (accessed July 3, 2014).

(102) Microbe Hunter Microscopy Magazine. Phase Contrast vs. Bright Field Microscopy. http://www.microbehunter.com/phase-contrast-vs-bright-field-microscopy/ (accessed June 29, 2014).

(103) Seah, M. P. Universal Equation for Argon Gas Cluster Sputtering Yields. *J. Phys. Chem. C* **2013**, *117*, 12622–12632.

(104) Bich, C.; Vianello, S.; Guérineau, V.; Touboul, D.; De La Porte, S.; Brunelle, A. Compatibility between OF-SIMS Lipid Imaging and Histological Staining on a Rat Brain Section. *Surf. Interface Anal.* **2013**, *45*, 260–263.

(105) Solé-Domènech, S.; Sjövall, P.; Vukojević, V.; Fernando, R.; Codita, A.; Salve, S.; Bogdanović, N.; Mohammed, A. H.; Hammarström, P.; Nilsson, K. P. R.; et al. Localization of Cholesterol, Amyloid and Glia in Alzheimer's Disease Transgenic Mouse Brain Tissue Using Time-of-Flight Secondary Ion Mass Spectrometry (ToF-SIMS) and Immunofluorescence Imaging. *Acta Neuropathol* **2013**, *125*, 145–157.

(106) Alan Institute for Brain Science. Alan Brain Atlas - Mouse P59 Sagittal. http://mouse.brainmap.org/experiment/thumbnails/100042147?image_type=atlas (accessed July 23, 2014).

(107) Moser, M.B.; Moser, E. I. Functional Differentiation in the Hippocampus. *Hippocampus* **1998**, *8*, 608–619.

(108) Oddo, S.; Caccamo, A.; Shepherd, J. D.; Murphy, M. P.; Golde, T. E.; Kayed, R.; Metherate, R.; Mattson, M. P.; Akbari, Y.; LaFerla, F. M. Triple-Transgenic Model of Alzheimer's Disease with Plaques and Tangles: Intracellular Aβ and Synaptic Dysfunction. *Neuron* **2003**, *39*, 409–421.

(109) Mold, M.; Ouro-Gnao, L.; Wieckowski, B. M.; Exley, C. Copper Prevents Amyloid-β1-42 from Forming Amyloid Fibrils under near-Physiological Conditions in Vitro. *Sci. Rep.* **2013**, *3*.

(110) Billings, L. M.; Oddo, S.; Green, K. N.; McGaugh, J. L.; LaFerla, F. M. Intraneuronal Abeta Causes the Onset of Early Alzheimer's Disease-Related Cognitive Deficits in Transgenic Mice. *Neuron* **2005**, *45*, 675–688.

(111) Pradillo, J. M.; Denes, A.; Greenhalgh, A. D.; Boutin, H.; Drake, C.; McColl, B. W.; Barton, E.; Proctor, S. D.; Russell, J. C.; Rothwell, N. J.; et al. Delayed Administration of Interleukin-1 Receptor Antagonist Reduces Ischemic Brain Damage and Inflammation in Comorbid Rats. *J Cereb Blood Flow Metab* **2012**, *32*, 1810–1819.

(112) Westermark, G. T.; Johnson, K. H.; Westermark, P. Staining Methods for Identification of Amyloid in Tissue. In *Methods in Enzymology*; Ronald Wetzel, Ed.; Amyloid, Prions, and Other Protein Aggregates; Academic Press, 1999; Vol. Volume 309, pp. 3–25.

(113) Vassar, P. S.; Culling, C. F. Fluorescent Stains, with Special Reference to Amyloid and Connective Tissues. *Arch Pathol* **1959**, *68*, 487–498.

(114) Picken, M. M.; Herrera, G. A. Thioflavin T Stain: An Easier and More Sensitive Method for Amyloid Detection. In *Amyloid and Related Disorders*; FASN, M. M. P. M.; M.D, A. D.; M.D, G. A. H., Eds.; Current Clinical Pathology; Humana Press, 2012; pp. 187–189.

(115) Ly, P. T. T.; Cai, F.; Song, W. Detection of Neuritic Plaques in Alzheimer's Disease Mouse Model. *J Vis Exp* **2011**.

(116) Maezawa, I.; Hong, H.-S.; Liu, R.; Wu, C.-Y.; Cheng, R. H.; Kung, M.-P.; Kung, H. F.; Lam, K. S.; Oddo, S.; LaFerla, F. M.; et al. Congo Red and Thioflavin-T Analogs Detect Aβ Oligomers. *Journal of Neurochemistry* **2008**, *104*, 457–468.